Optimization of wind turbine rotors - using advanced aerodynamic and aeroelastic models and numerical optimization

Døssing, Mads

Publication date:
2011

Document Version
Publisher's PDF, also known as Version of record

Citation (APA):
Døssing, M. (2011). Optimization of wind turbine rotors - using advanced aerodynamic and aeroelastic models and numerical optimization. Roskilde: Risø National Laboratory for Sustainable Energy, Technical University of Denmark. (Risø-PhD; No. 69(EN)).

Optimization of wind turbine rotors - using advanced aerodynamic and aeroelastic models and numerical optimization

Risø-PhD-Report

Mads Døssing
Risø-PhD-69(EN)
May 2011

Risø DTU
National Laboratory for Sustainable Energy

Author: Mads Døssing
Title: Optimization of wind turbine rotors - using advanced aerodynamic and aeroelastic models and numerical optimization
Division: Wind energy division

Risø-PhD-69(EN)
ISBN 978-87-550-3861-5
May 2011

Pages: 181
Tables:
References:

Information Service Department
Risø National Laboratory for
Sustainable Energy
Technical University of Denmark
P.O.Box 49
DK-4000 Roskilde
Denmark
Telephone +45 46774005
bibl@risoe.dtu.dk
Fax +45 46774013
www.risoe.dtu.dk

Summary

During the last decades the annual energy produced by wind turbines has increased dramatically and wind turbines are now available in the 5 MW range. Turbines in this range are constantly being developed and it is also being investigated whether turbines as large as 10-20 MW are feasible. The design of very large machines introduces new problems in the practical design, and optimization tools are necessary. These must combine the dynamic effects of both aerodynamics and structure in an integrated optimization environment. This is referred to as aeroelastic optimization.

The Risø DTU optimization software HAWTOPT has been used in this project. The quasi-steady aerodynamic module have been improved with a corrected blade element momentum method. A structure module has also been developed which lays out the blade structural properties. This is done in a simplified way allowing fast conceptual design studies and with focus on the overall properties relevant for the aeroelastic properties. Aeroelastic simulations in the time domain were carried out using the aeroelastic code HAWC2. With these modules coupled to HAWTOPT, optimizations have been made. In parallel with the developments of the mentioned numerical modules, focus has been on analysis and a fundamental understanding of the key parameters in wind turbine design. This has resulted in insight and an effective design methodology is presented.

Using the optimization environment a 5 MW wind turbine rotor has been optimized for reduced fatigue loads due to flapwise bending moments. Among other things this has indicated that airfoils for wind turbine blades should have a high lift coefficient. The design methodology proved to be stable and a help in the otherwise challenging task of numerical aeroelastic optimization.

Resumé

I de sidste 10-20 år er der sket en dramatisk øgning i den årlige energimængde produceret af vindmøller, og disse er nu tilgængelige i 5 MW klassen. Møller i denne klasse bliver konstant udviklet, og det bliver ligeledes undersøgt om møller så store som 10-20 MW er realiserbare. Design af meget store maskiner introducerer nye praktiske problemer, og optimerings-værktøjer er nødvendige. Disse skal kombinere de dynamiske egenskaber af både aerodynamik og struktur i et integreret optimerings værktøj. Dette benævnes aeroelastisk optimering.

Risø DTU's optimerings program HAWTOPT er blevet benyttet i dette projekt. Det kvasi-statiske aerodynamik-modul er blevet forbedret med en forbedret blad element metode. Et struktur modul, der udlægger bladets strukturelle egenskaber, er også blevet udviklet. Dette gøres på en forenklet måde, der muliggør hurtige design studier på koncept basis, og med fokus på de overordnede egenskaber der er vigtige for de aeroelastiske egenskaber. Aeroelastiske simuleringer foretaget i tidsdomænet er udført ved brug af HAWC2. Med disse moduler koblet til HAWTOPT er der lavet optimeringer. Parallelt med udviklingen af de nævnte moduler er der også fokuseret på analytiske analyser og på en fundamental forståelse for nøgleparametrene i design af vindmøller. Dette har resulteret i indsigt, og en effektiv design metode bliver præsenteret.

Ved brug af optimerings-værktøjet er en 5 MW vindmølle vinge blevet optimeret med henblik på en reducering af udmattelses-lasterne fra de flapvise bøjnings momenter. Dette har blandt andet indikeret, at vingeprofiler til vindmøller skal have en høj lift koefficient. Design metoden var stabil og en stor hjælp i den udfordrende opgave, som numerisk aeroelastisk optimering er.

Preface

This Ph.D. thesis has been prepared at Risø DTU National Laboratory for Sustainable Energy, Wind Energy Department (VEA) Aeroelastic Design Group (AED) - Technical University of Denmark (DTU), during the period from 2008 to 2011 as a partial fulfillment of the requirements for acquiring the Ph.D. degree in engineering. The work has been supervised by Senior Scientist Christian Bak (Risø DTU) and co-supervised by Research Specialist Helge Aagaard Madsen (Risø DTU) and Senior Scientist Mac Gaunaa (Risø DTU).

The project was funded by VEA, Risø DTU, and partly funded by the projects:

- ”Development of Adaptive Trailing Edge Flap (ATEF) System for Wind Turbines” funded by the Advanced Technology Foundation.
- ”Light Rotor” funded by Energy Technological Development and Demonstration Program, EUDP2010 I.

I would like to thank Marianna for her loving support during the PhD study.

Papers included in the thesis

[D] Madsen HAa, Bak C, Døssing M, Mikkelsen R, Øye S. Validation and modification of the Blade Element Momentum theory based on comparisons with actuator disc simulations.
Wind Energy, 2010. Published

[E] Døssing M, Madsen HAa, Bak C. Aerodynamic optimization of wind turbine rotors using a BEM method with corrections for wake rotation and expansion.
Wind Energy, 2010. Submitted

[F] Døssing M, Bak C. A numerical and analytical investigation of blade fatigue loads on the NREL 5MW wind turbine.
Wind Energy, 2010. Submitted

Contents

CHAPTER 1

Introduction

1.1 Background

Wind turbines are constantly being developed and redesigned. Today the largest machines are in the 5 MW range and some manufacturers are currently designing for 6 MW. At e.g. Risø DTU, research is presently aimed at designing turbines as large as 10-20 MW. The increasing size of wind turbines and the increasing market volume set increasing requirements to optimization of the wind turbine components. Models have been developed to design rotors aerodynamically. These models have shown how efficient a turbine can be with respect to energy production and how large the associated loads are. This leads to a trade-off between structural requirements and aerodynamic efficiency, and therefore represents an optimization problem. The problem becomes more complex when the unsteady loads leading to fatigue damage are considered as well. A common way of designing rotors is to make an aerodynamic design and based on this make a structural layout. The process is iterative and needs to be carried out manually. However, there is a trend toward integrating the different disciplines and carrying out the rotor design as a multidisciplinary process.

There is a large amount of literature on wind turbine properties and engineering tools, but there are not many references which describes the integrated design process. Bak [1] describes the state of the art in aerodynamic tools as well as general issues in aerodynamic turbine design. This includes airfoil properties and their influence on turbine performance. Other books on wind turbines are Hansen MOL [2] and Burton et al. [3], which are general introductions to many issues in turbine design, including loads and structures. Other references, which have been used in the project, are presented below.

Fuglsang [4] describes general aerodynamic design guidelines and Johansen et al. [5] describes a turbine designed for optimum aerodynamic performance. Snel [6] reviews the wind turbine aerodynamics. Key parameters in rotor design are described by Bak [7]. In recent years there has been some interest in winglets on wind turbines. Døssing [8] describes a winglet design algorithm and another algorithm for performance prediction is described by Gaunaa et al. [9]. Gaunaa & Johansen [10] has made a detailed study of various generic winglet designs. Even though winglets are out of the scope of the present thesis, much information about turbine aerodynamics may be obtained by studying winglets.

An improved blade element momentum method ($\mathrm{BEM_{cor}}$) is described by Madsen HAa et al. [11]. This is the primary aerodynamic calculation model used in this work.

Aerodynamic profile design is described by Timmer & van Rooij [12] and Fuglsang & Bak [13]. These references includes descriptions of the airfoils used in this project.

Rotor design taking structure and aeroelasticity into account is described in a number of articles. Fuglsang [14] gives an introduction to important issues in blade design and Fuglsang & Madsen [15] describe a numerical optimization method for wind turbine rotors. Fuglsang & Thomsen [16] and Fuglsang et al. [17] describe site specific optimization of cost of energy (COE) based on cost functions. More recently, Jonkman et al. [18] has defined a fictitious 5MW offshore turbine. This includes data for the nacelle, tower and foundation, and the turbine is a useful reference case for turbine development.

In a PhD thesis Nygaard [19] describes a numerical method for turbine optimization. The work includes descriptions of general aspects in turbine optimization. The optimizations are focused on cost of energy and primarily takes the aerodynamics into account. Very simple structural models are used for determining structural properties, which are found by simple scaling of existing cross section data. Aeroelastic calculations are avoided by assuming that fatigue loads are correlated to steady state loads at rated wind speed. It has been shown that this assumption is not valid and we have developed new engineering models for prediction of fatigue loads which may be used for fast optimizations without using aeroelastic calculations (Appendix F). A PhD study by Merz [20] is about conceptual design of a Stall-Regulated Rotor for deep water offshore use. It will be published in the near future 2011.

An introduction to aeroelastic stability issues for wind turbines is given by Hansen MH [21][22][23]. The topic is also treated by Riziotis et al. [24]. Even though aeroelastic stability is an important issue in connection to rotor design, it has not been considered in this work apart from the response predicted by aeroelastic simulations in the time domain.

Atmospheric turbulence is important for the dynamic loading on wind turbines and Fransen [25] describes turbulence in wind turbine clusters. The spectrum observed in the moving reference of the blade is discussed by Kristensen & Fransen [26] and measurements are reported by Connel [27]. This special topic is important for the fatigue loads on the blades.

1.2 Introduction to the project

The continuous development of wind turbine optimization tools means that software packages expands significantly as more experience is gained. The optimizations are based on the blade optimization tool HAWTOPT [16], which is developed at Risø DTU, Denmark. The aerodynamic optimization variables include the chord, twist and thickness distributions, but HAWTOPT can handle a large number of constraints and variables. At the start of this PhD study it was decided that the aerodynamic module needed improvements in order to accurately calculate the quasi-steady aerodynamics and the annual energy production (AEP). A corrected blade element momentum method $\mathrm{BEM}_{\mathrm{cor}}$ [11] has been implemented. A structural module was also needed for evaluation of structural properties and a new module for blade structural layout was developed. Focus was on developing a model which can lay out the overall properties of the blade and provide key parameters for the aeroelastic properties but at the same time be as simple as possible, thereby keeping the number of design variables at a minimum. Finally, with the structural data available, aeroelastic simulations were made using HAWC2 in order to calculate fatigue loads. The structural and aerodynamic design is now integrated in HAWTOPT and can be used to optimize a conceptual aeroelastic design. Figure 1.1 shows a roadmap of the design process.

Most optimization algorithms works effectively if the number of design variables are low and the initial design is relatively close to the optimum. This will enhance the numerical stability and reduce computation time. It is very challenging when the design is far from optimum and constraints are possibly violated. In that case there is a risk that a local optimum is found instead of the

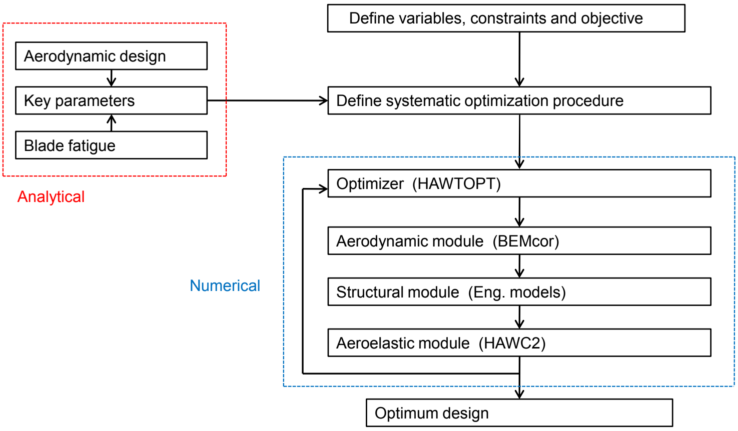

Figure 1.1: Project roadmap

global optimum or the algorithm may become unstable. This is especially likely to happen if many engineering models are used together, which is the case in wind turbine optimization. Based on practical issues, there are therefore many reasons for reducing the design problem as much as possible. Once a conceptual design has been found, it is possible to refine the optimization using more advanced models and more design variables. Thus, while it may be tempting to start with computational-heavy and accurate numerical models it is in practice a very difficult task and it will not provide any general understanding. Another reason for starting with simple models is that important parameters and their relative influence is clarified. This principle is applied throughout the presented work where it is the aim that the number of design variables should be as low as possible and engineering models should be as simple as possible.

Blades have been optimized for a 5 MW pitch regulated variable speed turbine (PRVS), which is a representative design for modern turbines. The optimization is focused on weight restrictions and fatigue loads due to bending of the blades caused by atmospheric shear, turbulence and gravity. Other objectives may be important but the fatigue loads are key parameters in the blade design process. The optimization tools may of course be used for optimization of other objectives. The primary constraint is the energy production because the yearly revenue is directly proportional to it.

Most published studies are focused on minimizing a cost function by taking individual component material and manufacturing costs into consideration as well as transportation etc. While this may be possible for a company it is not easily done in general in a scientific context because of lacking knowledge of the specific cost functions. More and more turbines are placed at sea and the blade production costs are now only a relatively small fraction of the total cost and more emphasis is on reliability. In this work focus in on the optimization of key parameters instead of cost. To ensure the design is economically feasible, various constraints are used. E.g. a minimum annual energy production.

The PhD project described in this thesis has focused on the development of tools for conceptual design of the rotor blades. The conceptual design represents a simplified initial layout of the blade, which is detailed enough to describe the overall aerodynamic and structural properties. Combining this yields the aeroelastic properties which are key parameters for fatigue loads and dynamic stability, and which must be considered in the initial design phase. Subsequently the blade aerodynamics and structure can be refined, without changing the aeroelastics significantly.

The blade design is made using engineering models coupled to optimization software. The engineering models describe the quasi-steady aerodynamics and the structural properties, and an aeroelastic simulation software is used to obtain time series of loads and energy production under unsteady conditions. Models for e.g. noise may also be used but focus is on the aforementioned. The final conceptual design is described by the aerodynamic shape and the structural layup of material inside the blade. This represents two vast engineering fields which in combination with heavy numerical optimization results in a complex problem.

The scope of this thesis is to present important results from the project. Numerical results have been combined with discussions of key parameters and thereby fairly general conclusions have been made. Focus is on the optimization methodology and results, but details are also included where appropriate. Aeroelastic optimization is complex, but hopefully reading this thesis will create an overview of the relations between many parameters in the rotor design process.

1.3 Design variables, constraints and objectives - model limitations

The design variables considered in this thesis are the spanwise distributions of chord, twist and thickness. These are numerically optimized and the process includes an automatic definition of the blade structural properties. Constraints are put on the annual energy production, blade mass and tip deflection relative to the blade shape at zero load. The objective is to minimize a selected load or combinations thereof. In this thesis flapwise fatigue loads have been minimized.

Some important limitations are listed below. Note that these may all be included in the optimization method presented.

- Edgewise fatigue loads are not minimized (however, the final design shows a reduction).
- The undeformed blade is assumed straight.
- Buckling is not considered.
- The design load cases does not include storm loads, e.g. DLC 6.4 .
- The design load cases does not include cases which are strongly controller dependent.
- The design load cases does not cover cases where stability is important.
- Load extrapolation of extreme loads is not done.

1.4 Outline of the thesis

The contents of the thesis is:

Chapter 2 is an introduction to important issues in the aerodynamic design of rotors.

Chapter 3 and 4 introduces the developed cross section and blade structural models for conceptual structural design.

Chapter 5 describes the wind turbine optimization methodology used in the project.

Chapter 6 discusses results of aeroelastic optimizations.

Chapter 7 contains conclusions from the project.

Appendix A is a summary of the basic aerodynamic rotor equations.

Appendix B describes analytical equations for aerodynamic rotor design.

Appendix C describes the fatigue analysis used for simplifying a complex dynamic load spectrum into an equivalent load.

Appendix D describes BEM_{cor}. Published in Wind Energy.

Appendix E describes numerical aerodynamic optimization using the corrected blade element momentum method ($\mathrm{BEM}_{\mathrm{cor}}$). Submitted for publication.

Appendix F describes analytical prediction of blade fatigue. Submitted for publication.

1.5 Contributions

An overview of the work carried out during the 3-year PhD study is given below. This includes topics which will not be described in detail in this thesis. Unless otherwise stated the author is Mads Døssing.

- A method for analysis of wind tunnel measurements using high frequency microphones distributed over the surface has been established. The analysis aims at determining the laminar to turbulent transition point. The method is described in technical reports [28] and [29](co-author) and was presented to the industry on the Aeroelastic Workshop, May 2008[1]. Results are given in the technical reports [30][31] and [32].

  Work has also been carried out in relation to the full scale DAN-Aero experiment where transition has been measured under unsteady inflow conditions.

- The corrected blade element momentum method $\mathrm{BEM}_{\mathrm{cor}}$ has been implemented in the optimization program HAWTOPT. A reviewed article on the method has been published in Wind Energy [11](Appendix D)(3rd author). A conference paper [33] was also published at the 2009 EWEC Conference in Marseilles and a poster presentation was given. A journal article on aerodynamic optimization has been submitted for publication in Wind Energy: Appendix E(1st author).

- Methods for analytical aerodynamic design has been studied and a model based on constant axial induction has been defined (Appendix B). This has clarifed key parameters in aerodynamic design.

- A structural model for cross section properties has been developed. This has been combined with a simple method for layout of the material in the blade in order to obtain structural data using as few parameters as possible. This is described in Chapters 3 and 4. The model is linked to HAWTOPT.

---

[1] Risø DTU EFP-Themeday

- Based on comprehensive studies of aeroelastic simulations an analytical model for the fatigue loads on blades due to shear, turbulence and gravity loads has been been derived. A conference paper [34] was published at the 6th PhD Seminar Wind Energy in Europe, Trondheim 2010. A journal article on the topic has been submitted for publication in Wind Energy: Appendix F(1st author).
- HAWOPT, including $\mathrm{BEM}_{\mathrm{cor}}$ and the developed blade structure module, has been linked to the aeroelastic calculation program HAWC2 and aeroelastic optimizations have been carried out. The results are described in this thesis.
- Collaboration with industrial partners has taken place in 2 projects where blades have been designed. The contents of these projects are confidential. The workload for the author was approximately 250 hours.
- Contributions have been made to a conference paper on winglets for wind turbines by Gaunaa et al. [9](3rd author).

CHAPTER 2

Aerodynamic design

The topic of this chapter is the quasi-steady aerodynamic design of the rotor at various wind speeds or tip speed ratios. This influences the annual energy production and the mean value of structural loads, and it is therefore a good starting point in the design process. A general introduction to rotor aerodynamics will be given and this highlights key parameters.

Both analytical and numerical results are discussed. The analytical design model is presented in detail in Appendix B and it describes the basic design variables. However, even though the analytical designs are good they do not represent the optimum, and for this the numerical models are necessary. Such numerical optimizations have been carried out and are described in Appendix E. In this chapter selected results have been included. The numerical aerodynamics were calculated using the corrected blade element momentum method ($\mathrm{BEM}_{\mathrm{cor}}$) which is described in Appendix D.

It will be explained later that the sensitivity to atmospheric turbulence can be calculated based on quasi-steady aerodynamic design parameters. However, full aeroelastic calculations will be necessary in order to include controller performance and possible stability problems and the discussion about fatigue therefore falls naturally into Chapters 5 and 6 and is omitted here.

Introductions to general wind turbine aerodynamics are found in Hansen MOL

[2] and Burton et al. [3].

2.1 2D airfoil aerodynamics

The airflow at a given radius on the blade is to a first approximation 2 dimensional. However, there are 3D effects due to spanwise flow and data must be corrected for this. Important 2D aerodynamic parameters are the lift and drag coefficients

$$C_l = \frac{l}{{}^1\!/_2 \rho v_{rel}^2 c} \tag{2.1}$$

$$C_d = \frac{d}{{}^1\!/_2 \rho v_{rel}^2 c} \tag{2.2}$$

where l is the lift, d is the drag, ρ is the density of air, c is the chord and v_{rel} is the relative inflow velocity.

The 2D flow depends on the Reynolds number Re, which typically is in the order of 1.0e6 to 1.0e7 for a 5 MW machine depending on rotational speed[1]. At startup the Reynolds number is small and it increases until the maximum rotational speed is obtained. Airfoil data representing a typical Reynolds number can be used but it is important to ensure that the data is not too sensitive to changes in Re. The airfoil data can be obtained using computational fluid dynamics (CFD) or by testing in a wind tunnel. XFoil [35] is a program which gives good results at modest inflow angles. The 3D correction procedure used in this work is described in [36]. Note that the blade element momentum method (BEM) is depending on reliable 2D aerodynamic data. The uncertainty on this topic is reduced by using profile series which are tested and validated.

Airfoil-data should be selected which are not sensitive to leading edge roughness. The sensitivity depends on the actual design but in general airfoils which have a thickness relative to chord greater than $t \approx 24\%$ are sensitive. Thus, from an aerodynamic viewpoint it is important that as much as possible of the blade is made using thin profiles, i.e. the relative thickness should be in the range $15\% < t < 24\%$.

It is important that the airfoil has little drag, because it decreases the turbine power. The optimum lift to drag ratio ${}^l\!/_d = {}^{C_l}\!/_{C_d}$ is usually limited to a small range of the angle of attack α, and the blade should therefore operate at that design point. For a given aerodynamic design, the value of C_l dictates c, since a

---

[1] Re is based on c

given lift must be obtained. The choice of C_l therefore affects many structural parameters such as stiffness and mass etc., which depend on c. These are important parameters influencing the aeroelastic properties and this yields a complex optimization problem. Experience shows that airfoils should have a high design lift coefficient because it reduces the dynamic loading due to turbulence and the results from Chapter 6 confirms this. The range from C_l to its maximum value $C_{l,max}$ should also be considered because it may affect stall induced vibrations and because there should be some safety in that the C_l value can be obtained in practice.

2.2 3D aerodynamic design

The 3D aerodynamics refers to the overall flow which is not limited to an area close to the blades. This flow is governed by the axial induction a which decelerates the flow of air past the rotor, but a number of other phenomena are also important. The 3D flow depends on the aerodynamic load distribution on the blades. Given an optimum load distribution it is possible to design a blade in many ways, and the result will depend strongly on the 2D airfoil data - this will be explained in detail below.

The aerodynamics can e.g. be calculated using the following methods: Navier-Stokes computational fluid dynamics (CFD), where the actuator line method and the actuator disc method (ACD) are special cases, potential flow methods and the blade element momentum method (BEM). At the Technical University of Denmark, a method is being developed where a CFD code is used in the viscous boundary layer and the surrounding flow is calculated using a potential flow method. The latter and CFD are the only methods which do not depend on 2D data, but unfortunately they are computational heavy.

In the present work, the corrected blade element momentum method $\mathrm{BEM}_{\mathrm{cor}}$ [11] was used for numerical calculations. This is a fast method and the accuracy is good because it includes the effects of wake expansion and pressure change caused by wake rotation. It is further important to note that very accurate 2D airfoil data is available today where CFD and high quality wind tunnels are available - however, it is still necessary to correct the data for 3D and roughness effects and this procedure requires considerable engineering skills.

Before making optimizations it is worth studying the theory behind the 3D aerodynamics because the problem can be reduced to depend on a few dimensionless key-parameters. Important dimensionless integral properties are the power, thrust and root flap moment coefficients

$$C_P = \frac{P}{1/2 \rho V_0^3 \pi R^2} \tag{2.3}$$

$$C_T = \frac{T}{1/2 \rho V_0^2 \pi R^2} \tag{2.4}$$

$$C_F = \frac{M_F N_B}{1/2 \rho V_0^2 \pi R^3} \tag{2.5}$$

where P is the power due to aerodynamics, T is the thrust force and M_F is the moment measured in the rotor center. V_0 is the wind speed, R is the rotor radius and N_B is the number of blades. P is acting on the shaft and the electrical power is diminished by the drive train losses. T generates an overturning moment on the tower and M_F is equal to the bending moment if the blade is clamped-free, which is usually the case. For fixed tip speed ratio λ, a blade with defined twist (β), tip pitch (θ_p) and chord distribution will experience flow similarity and constant values of C_P, C_T and C_F. λ is defined as

$$\lambda = \frac{\Omega R}{V_0} \tag{2.6}$$

where Ω is the rotational speed. It will be shown in Section 2.3 that the requirement for a fixed chord can be overcome by requiring a fixed design parameter instead, which gives some freedom in the value of c. The flow similarity is caused by similarity in the loads distributed along the blade. The dimensionless load distribution is given by the local thrust and torque coefficients: C_t and C_q ((A.14) and (A.15)). C_q can be found for a given C_t and the aerodynamics can therefore be reduced to depend on only C_t and λ.

2.3 Design equations

The important parameters can best be explained by studying the basic rotor theory. A comprehensive summary of important equations can be found in appendix A.

The lift and drag coefficients, which depend on the local angle of attack, are projected onto a direction normal and tangential to the rotor plane yielding the normal coefficient C_y and the tangential coefficient C_x (Equations (A.12) and (A.11)). The thrust coefficient is then defined as

$$C_t = \frac{v_{rel}^2 C_y c N_B}{V_0^2 2 \pi r} \tag{2.7}$$

where r is the radius. C_y is usually dominated by the lift forces and assuming zero drag the equation may be rewritten[2]

$$c^* C_l N_B = C_t 2\pi \frac{r^*}{{v^*_{rel}}^2 \cos\phi} \tag{2.8}$$

where ϕ is the inflow angle measured relative to the rotor plane. $v^*_{rel}=v_{rel}/V_0$ is the dimensionless relative velocity and $r^*=r/R$ the dimensionless radius. For fixed λ and C_t, both v^*_{rel} and ϕ are fixed as well and may be calculated as described in section A.5. For a given λ and distribution of C_t over the blade, the distribution of $c^* C_l N_B$ is a corresponding design parameter which will ensure a similar load distribution. It is noted that the design parameter will depend slightly on N_B because it affects the tip losses which changes v^*_{rel} and ϕ. However, this is limited to the tip region and the changes are small. Thus N_B is included in the design parameter to highlight that the 3D design is largely independent on the number of blades. In section 2.4 a detailed analytical example is given.

Besides from λ and the design parameter distribution, all other quasi-steady properties follows in dimensionless form. E.g. C_F, C_P and C_T.

Examples of optimum distributions of $c^* C_l N_B$ can be found in appendix F where the inflow angles are shown as well.

The actual blade shape is found by specifying C_l and N_B and calculating c^*. The blade twist β can be found from the inflow angle and the specified angle of attack using equation (A.4). c^* and β now defines the aerodynamic shape of the blade. The relative thickness t can be omitted in the aerodynamic analysis if C_l and l/d are defined, which may be useful for design purposes. t is mainly important for the structural properties and will first be included in Chapter 5.

The definition of the design parameter is inspired by the work of Burton et al. [3] which describes a blade geometry parameter similar to $c^* C_l N_B$.

2.4 Analytical design equations for uniform thrust

Equation (2.8) is local (i.e. distributed along the blade span). To obtain integral quantities such as C_P it is necessary to define λ and the distribution of e.g. C_t. An analytical study has been made on rotors with constant axial induction,

---

[2] note that the drag can not be neglected when calculating the power but here it is a good approximation

which is equivalent to prescribed load distribution. The details can be found in Appendix B and the results are discussed below.

The turbine is defined by specifying λ and C_{t2}, which is C_t corrected for tip losses

$$\lambda\,, \quad C_{t2,d} = \left({}^{C_t}\!/_F\right)_{design} \tag{2.9}$$

Where F is Prandtl's tip loss factor. The axial induction is related to $C_{t2,d}$ according to (A.40).

$$a = k_3 C_{t2,d}^3 + k_2 C_{t2,d}^2 + k_1 C_{t2,d} \tag{2.10}$$

This polynomial is used in HAWC2 [37] and represents the classic BEM results at low loadings and ACD results at high loading. In the following it must be remembered that $a{=}a(C_{t2,d})$, which is not explicitly written. Two dependent design coefficients are defined and they govern the influence of tip losses and wake rotation.

$$A_1 = \frac{1}{2} N_B \sqrt{1 + \frac{\lambda^2}{(1-a)^2}}\,, \quad A_2 = \frac{C_{t2,d}}{\lambda^2} \tag{2.11}$$

The influence of tip losses is described by integrals which have been calculated numerically for different values of A_1. By fitting a curve to the result a correction on total thrust due to tip losses is found ($A_1 > 5$)

$$C_{T,F} = -\frac{1.392}{1.2 + A_1} C_{t2,d} \tag{2.12}$$

A similar correction on the flap moment is ($A_1 > 5$)

$$C_{F,F} = -\frac{1.4}{2.3 + A_1} C_{t2,d} \tag{2.13}$$

By integrating as function of A_2, a correction for wake rotation losses on the power is found ($A_2 < 0.065$)

$$C_{P,a'} = \left(4.906 A_2^2 - 1.173 A_2 - 0.002362\right) C_{t2,d}(1-a) \tag{2.14}$$

The total thrust and root flap moment coefficient can now be found

$$C_T = C_{t2,d} + C_{T,F}\,, \quad C_F = {}^2\!/_3 C_{t2,d} + C_{F,F} \tag{2.15}$$

The influence of drag on the power is

$$C_{P,d} = -C_F \lambda \left({}^l\!/_d\right)^{-1} \tag{2.16}$$

where a uniform $^{l}/_{d}$ is assumed. The importance of $^{l}/_{d}$ is seen, and this should be as high as possible. $C_{P,d}$ is the only quantity which depends on drag, and this follows from the assumption that drag has no influence on C_t. The total aerodynamic power is

$$C_P = (1-a)C_T + C_{P,a'} + C_{P,d} \tag{2.17}$$

$(1-a)C_T$ is the major contribution to the shaft power and it represent the power exerted by the airflow onto the rotor thrust. It is diminished by $C_{P,a'}$ and $C_{p,d}$. The inviscous power coefficient $C_{P,l}$ is defined as

$$C_{P,l} = C_P - C_{P,d} \tag{2.18}$$

In general $C_{P,l}$ can be calculated using Equation (A.53).

The distributed flapwise moment due to aerodynamics is

$$C_f = C_{t2,d}\left(^{1}/_{3}{r^{*}}^{3} - r^{*} + ^{2}/_{3}\right) + C_{F,F} - r^{*}C_{T,F}\ , \quad r^{*} < \frac{r_F^{*}+1}{2} \tag{2.19}$$

where r_F^{*} is the radial position where tip losses becomes negligible (Eq. A.39). The flapwise bending moment is usually the dominating force on the blade and the layup of the main spars may be based on (2.19). In that case M_f should be calculated at rated wind speed where the aerodynamic forces are largest (for pitch regulated turbines). Note that the dimensionless bound circulation and other quantities also follows from the analysis. The tip loss factor is

$$F = \frac{2}{\pi}\arccos\left(e^{A_1(r^{*}-1)}\right) \tag{2.20}$$

Equations (2.9) to (2.20) are relatively simple considering the complexity of the problem and the important quantities can be plotted as function of λ and $C_{t2,d}$. Figure 2.1, 2.2 and 2.3 shows contour plots of C_P, C_T and C_F for $^{l}/_{d}$=100. The C_P contours depend strongly on $^{l}/_{d}$ and the value selected is representative for most practical designs. There is a clear peak in the predicted power around λ=8 and C_t/F=0.98. On the figure is also seen the working points for the NREL 5MW reference turbine [18]. Figure 2.4 shows the spanwise distribution of the design parameter at various working points. In general, the design parameter becomes larger at low λ and high loading (C_t/F) but by varying C_l it is also possible to obtain the exact same chord distribution independent of λ, as long as the C_l value can be obtained in practice. However, often C_l is determined based on the selected airfoil, structural requirements and aeroelastic properties.

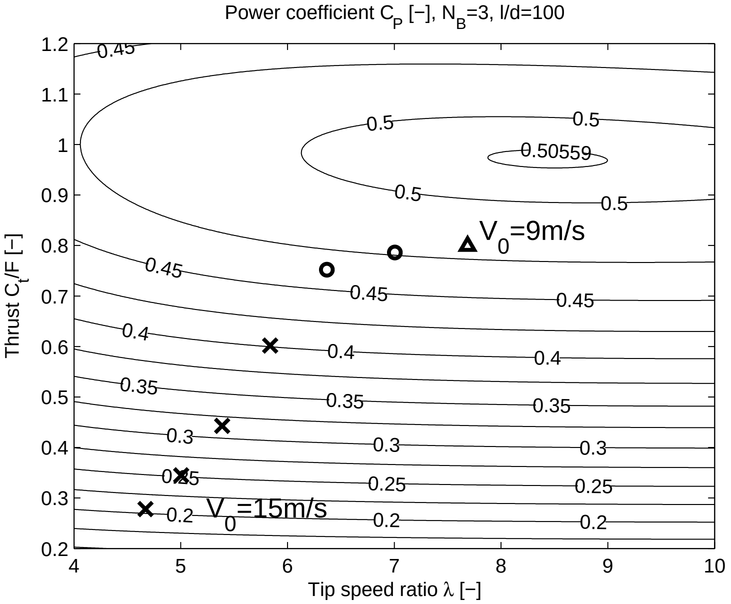

Figure 2.1: Contour plot of C_P versus local thrust coefficient and tip speed ratio. The symbols indicate values for NREL 5MW. The *triangle* represents the largest λ which is equivalent to wind speeds in the range $5 < V_0 < 9$ m/s where Ω is varied. The *circles* represent V_0=10 and 11 m/s where the max Ω is reached and λ therefore decreases and the turbine is less aerodynamically efficient (lower C_P). The *crosses* indicate wind speeds where the rated power is reached (11 m/s$< V_0$). The trust drops significantly because the blades are pitched toward lower angle of attack to reduce power. Note that this is an idealized representation of the working points for a PRVS turbine.

The C_F contours are aligned with the C_T contours but in more refined designs it is important to notice that reductions in bending moments may be obtained by optimization, which will decrease the loading near the tip. Figure 2.5 shows distributed variables for NREL 5MW in its original layout at λ=7. The design parameter is compared to the analytical found using the analytical model and the same λ. C_t/F is selected in order to obtain the same C_P as NREL 5MW. The largest difference is found near the root and tip. Note that on NREL 5MW C_t/F is increasing toward the tip, which is often seen in practice. An improvement to the analytical design model would therefore be to use a distribution model for C_t/F which decreases near the root and increases near the tip.

There are no corrections for wake expansion and the effects of wake pressure

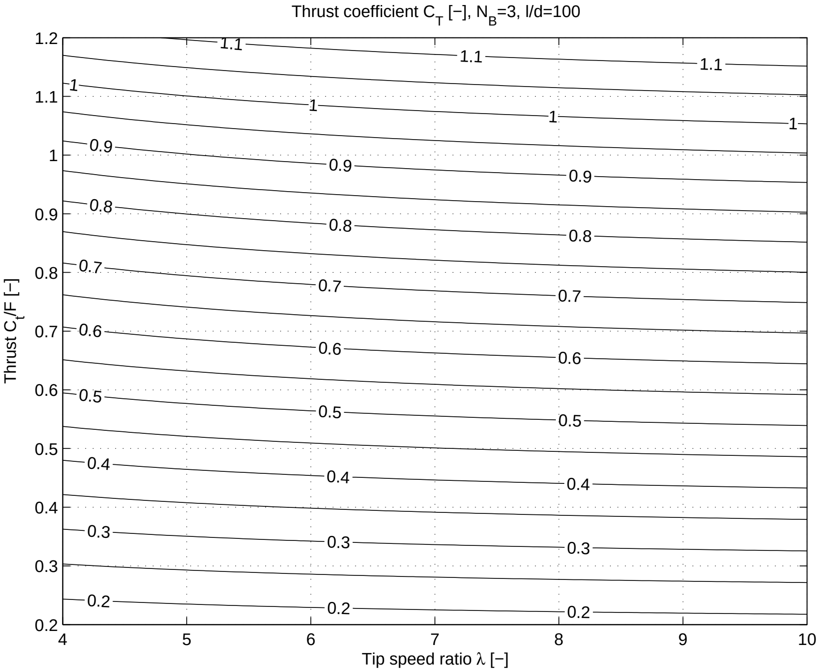

Figure 2.2: Contour plot of C_T versus local thrust coeffient and tip speed ratio.

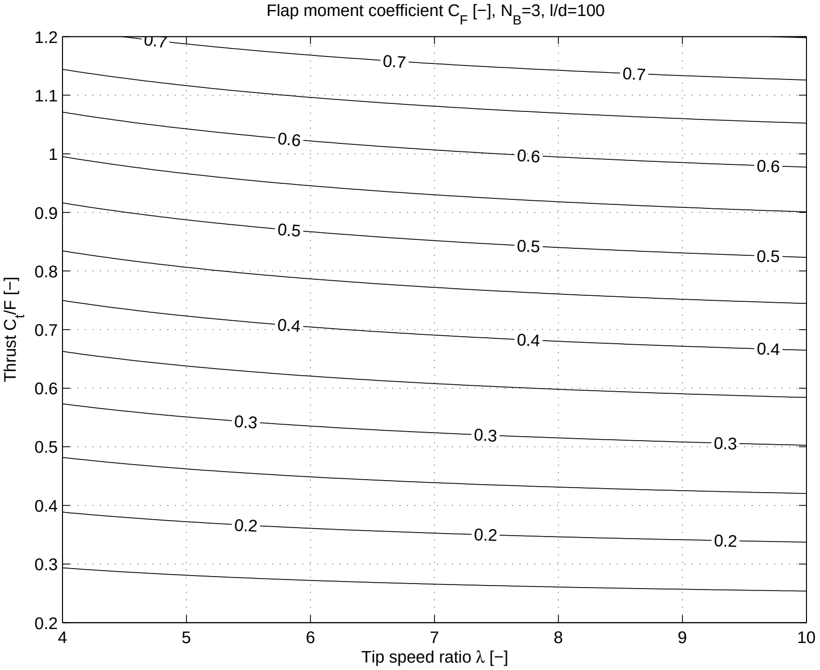

Figure 2.3: Contour plot of C_F versus local thrust coeffient and tip speed ratio.

due to rotation, but these effects may be neglected when studying first order effects. The effects are included in $\mathrm{BEM}_{\mathrm{cor}}$, which will be used in subsequent numerical calculations and optimizations.

2.5 Single and multi point optimization

The design parameter is defined in a working point represented by λ. A final design can only be made by considering the whole range of operating conditions but the single point design will still be a good first approximation. Typically a λ value is selected which corresponds to wind speeds below rated power because there is no need for power optimization above rated wind speed. For PRVS turbines, AEP is only slightly affected by the turbine being designed in a single point, but it is noted that this depend on many factors and the designer must consider this in the design process. If the turbine operates at wind speeds where the design λ can not be achieved due to restrictions in rotational speed, the turbine will pitch toward higher angles of attack in order to maintain a high

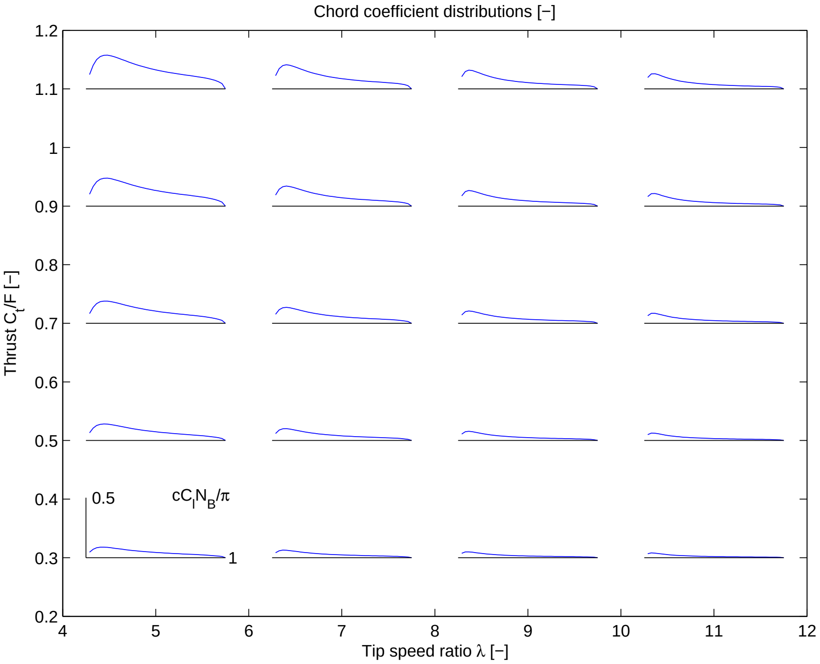

Figure 2.4: Overview of the aerodynamic design parameter versus local thrust coeffient and tip speed ratio.

loading despite Ω being below design value. If $C_{l,max}$ is reached there will be a drop in power in addition to the drop in power caused by the increase in drag as the airfoil gets closer to stall. This must be considered if the design point is well below rated wind speed and λ is large - in that case there should be sufficient lift reserve between C_l and $C_{l,max}$. In Chapter 6 a design point at rated power is used (i.e. low λ) which gives good initial results. Thus, PRVS turbines may be optimized in a single point, but a multi point optimization is still necessary for the evaluation of fatigue loads and for final optimization of AEP.

2.6 Numerical aerodynamic optimization

In the following a summary of the work done on aerodynamic optimization of wind turbine rotors is given. It is described in details in Appendix E.

The blade element momentum method with corrections for wake rotation and

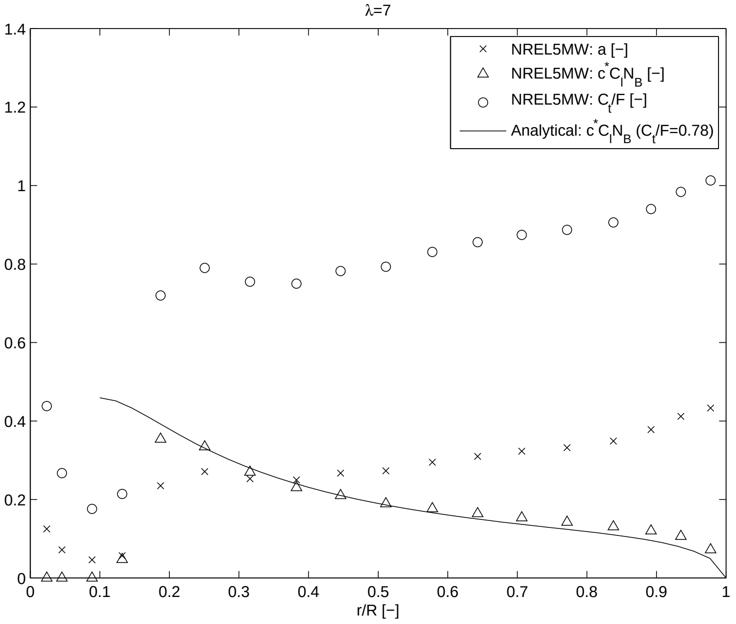

Figure 2.5: Design variables for the NREL 5MW turbine at λ=7.

expansion (BEM$_{\text{cor}}$) was used. The wake rotation refers to the positive effects of the suction created behind the turbine in the root region. The wake expansion has a negative effect near the tip. Both effects are not included in the traditional BEM method. BEM$_{\text{cor}}$ is described in detail in [11].

A plot of the dimensionless axial velocity in the rotor plane $v_a^*{=}v_a/V_0$ is useful for validation of BEM$_{\text{cor}}$, because the corrections are included in order to calculate it more accurately. Figure 2.6(a) shows the difference in v_a^* obtained using BEM and BEM$_{\text{cor}}$ for a redesign of the NREL 5MW rotor where the rotor is designed for maximum power at λ=8, using Risø B1-15 airfoils with design C_l=1.4 and l/d=110 on the entire rotor (Ref. [38]). Δv_W and p_w refers to details in the model. The results are compared to an ACD calculation and a good agreement is observed between BEM$_{\text{cor}}$ and ACD - ACD being the most accurate of the methods. The BEM method shows some differences in the root and tip region. The impact of these differences depends on the actual blade design and its load distribution, leading to differences in C_P, C_T and C_F. Table 2.1 compares results for the NREL 5MW turbine [18] at wind speeds of 5 and 11 m/s. BEM$_{\text{cor}}$ predicts a 0.5% lower value of C_P, compared to BEM.

A series of aerodynamic optimizations have been carried out. The objective was

	C_P	C_T	C_F
V_0=5 m/s, λ=8.0			
BEM$_{\text{cor}}$	0.4937	0.8637	0.5884
BEM	0.4961	0.8697	0.5964
V_0=11 m/s, λ=6.4			
BEM$_{\text{cor}}$	0.4593	0.7186	0.4811
BEM	0.4617	0.7183	0.4831

Table 2.1: Comparison of different aerodynamic models used to calculate properties for the NREL 5MW turbine [18].

either maximum power, or minimum thrust at reduced power. The latter is in order to reduce the loads which increase dramatically when the optimum power is sought. The optimization variable is the distribution of axial induction, which is equivalent to the load distribution. Note that results have been found using both BEM and BEM$_{\text{cor}}$ in order to highlight differences in the design optima.

Figure 2.6(b) shows the optimum values of C_P plotted against λ. The results are given with and without tip losses and drag, and the importance of these effects can be seen. The most realistic case is with tip losses and drag included, and there is very little difference in the results for $6< \lambda <8$, which is often the range for operation below rated power.

Figure 2.7 shows the optimized design parameter and inflow angle distributions at two operation points: λ=5 and λ=7. It is noted that there is only a minor difference between BEM and BEM$_{\text{cor}}$. The distributions of the design parameter are almost equal. The major difference is in the inflow angle, and the blade twist should therefore be different.

Optimizations at λ=6 and 8 at reduced power, shows that there may be important differences in C_P, C_T and C_F when comparing BEM and BEM$_{\text{cor}}$. This is discussed in detail in Appendix E. Note that BEM$_{\text{cor}}$ shows a possible reduction in the flapwise bending moment at λ=6, which is a typical value at rated power where the largest quasi steady loads are found, i.e. the design loads.

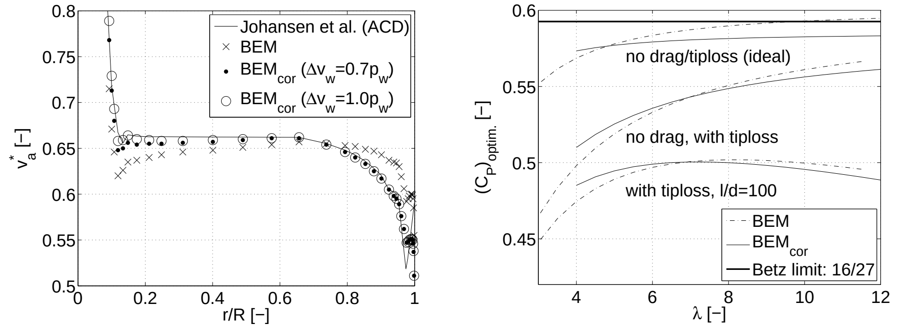

(a) The axial wind speed in the rotor plane calculated with different aerodynamic models.

(b) Optimum aerodynamic efficiency versus tip speed ratio, calculated with different aerodynamic models.

Figure 2.6: Comparisons of aerodynamic models.

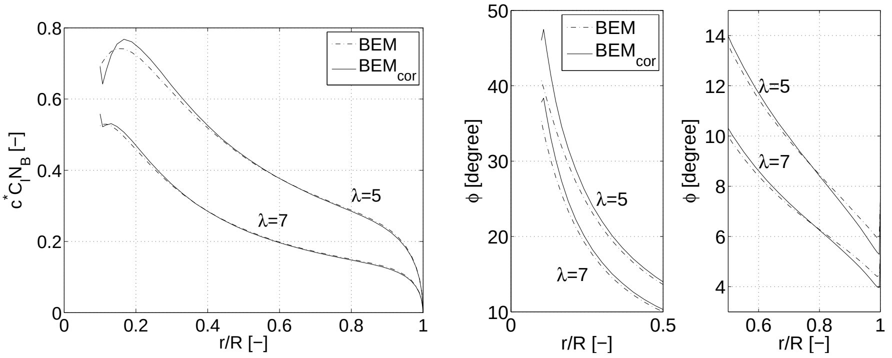

(a) Design parameter

(b) Inflow angle

Figure 2.7: Distributions of design parameter and inflow angle for optimum C_P designs ($^l/_d$=100).

2.7 Conclusions

All quasi-steady key parameters in the 3D aerodynamic design are dimensionless and follows from λ and the distribution of C_t. This includes the distributions of inflow angle ϕ and the design parameter $c^* C_l N_B$ and moment coefficient C_f as well as the integral power, thrust and moment coefficients (C_P, C_T and C_F). These quantities have been described analytically in the case of a defined constant value of C_{t2}, which is equivalent to a constant axial induction. Examples of the design parameter optimized using BEM and BEM_{cor} have been given.

Given the 3D aerodynamic design the actual distribution of c^* follows from the distribution of C_l which is a key 2D parameter. The value of c^* influences the blade structural parameters such as stiffness, mass and eigenfrequencies, and is also important for the fatigue sensitivity to unsteady inflow.

The 2D drag has very little influence on the 3D aerodynamics and therefore it has no direct influence on the blade design. Instead, the drag generates a moment which reduces the turbine power. In practice, the choice of C_l will depend on the drag characteristics (i.e. a high $^l/_d$ is preferable) but this may be overcome by using profiles with good performance at the desired C_l values.

BEM_{cor} has been validated and gives results which are close to those of an actuator disc. For a specific turbine, the difference in predicted C_P was 0.5%. It has also been shown that there are fundamental differences in the optima for BEM_{cor} compared to BEM. E.g. a turbine with the same power may be designed for a lower flapwise bending moment using BEM_{cor}. The difference in the blade aerodynamic shape is mainly on the twist.

CHAPTER 3

Structural model for the blade sections

This chapter deals with the structural properties of a blade cross section. A relatively simple model is used which is sufficient to provide the most important data which is used as input to the blade layout model presented in Chapter 4. The method is based on dimensionless coefficients from which scaling to the actual chord and shell thickness can be made.

In the following it is shown how structural parameters can be obtained, which are assumed to be sufficient to make trustworthy aeroelastic calculations and stability analysis. Because the scope of this work is not in the structural details it is possible to reduce the number of inputs, which will simplify aeroelastic optimizations. The important structural data which should be modeled includes the bending stiffness EI, the torsional stiffness GJ, the section mass m and various centers. The method predicts the center of gravity (CG) and the elastic center (EA[1]). The shear and aerodynamic centers (SC and AC) are not described and are defined. From 2D analysis for thin airfoils it is known that AC is in $^1/_4c$ and this will be assumed to be true in general. SC is assumed constant. Flutter stability depends mainly on EA, CG and AC but other instability issues and the general aeroelasticity is more complicated. The geometrical shape of the blade (sweep, prebend etc.) and the distribution of properties are also important, but this is treated in later chapters.

---

[1] EA should not be confused with the spanwise stiffness EA

The method is based on integrals which in general can be calculated numerically for an arbitrary cross-section. A model where the cross section is represented by straight line polygons is also described. This has the advantage that an analytical solution is available. However in the following chapters data obtained numerically for realistic shaped airfoils is used. Methods based on Taylor expansions are also given as well as a study of simple scaling of reference data.

A general introduction to the wind turbine cross section properties is found in M.O.L. Hansen [2]. This has been combined with the methods for structural idealization described in Megson [39], Chapter 9.

The important material parameters are the spanwise elastic modulus E_{11}, the in-plane shear modulus G_{12} of the outer shells and the density ρ. Subscript 1 refers to the spanwise direction which is orthogonal to the cross section. In the following the notation is simplified to E and G.

3.1 Coordinates and section layout

The calculations are based on thin walled sections (shells) which are divided into sectors denoted α, β, γ and δ. α, β and γ sectors follow the airfoil surface. The δ sectors represent the shear webs. Shear deformations are not considered and in the following the δ sectors are included primarily to take their mass into account.

The structural sections are defined symmetrically around EA. In that way EA will not move if more material is added in a sector. The α sector is the main carrying spar and the γ-sector represents the leading and trailing edges. The β sector is connecting the two and δ represents the shear webs. They are defined by $x_1 \dots x_5$ which gives the positions along the chord line relative to the leading edge.

The following analysis is simplified by using a coordinate system with origo in the elastic axis (EA) (see Figure 3.1). The position can be determined using (3.6) and the coordinate system subsequently moved. Figure 3.2 shows an example of a structural layout before translating the coordinates so they will have origo in EA.

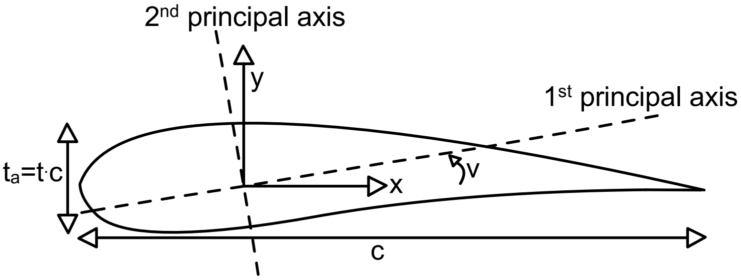

Figure 3.1: The coordinate system and principal axes. The coordinate system should have origo in EA.

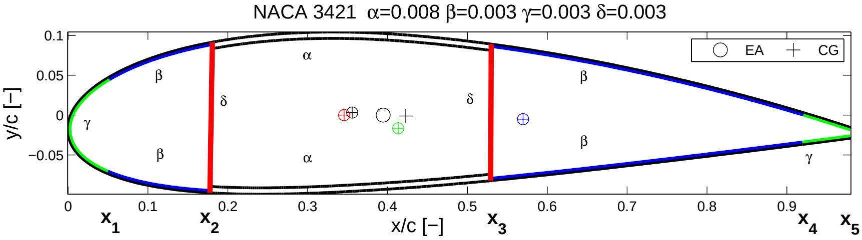

Figure 3.2: Example of geometrical layout. Note that in the following the origo should be in EA.

3.2 Structural integrals

The important structural quantities are described by the integrals in Table 3.1. The torsional stiffness requires special considerations and is included later.

Section area (closed section)	$A_0 = \int_S \operatorname{sgn}(y) y \, dx$
Section mass	$m = \int_A \rho \, dA$
Longitudinal stiffness	$EA = \int_A E \, dA$
Moment of stiffness about the x axis	$ES_x = \int_A Ey \, dA$
Moment of stiffness about the y axis	$ES_y = \int_A Ex \, dA$
Moment of mass about the x axis	$\rho S_x = \int_A \rho y \, dA$
Moment of mass about the y axis	$\rho S_y = \int_A \rho x \, dA$
Moment of stiffness inertia about the x axis	$EI_x = \int_A Ey^2 \, dA$
Moment of stiffness inertia about the y axis	$EI_y = \int_A Ex^2 \, dA$
Moment of centrifugal stiffness	$ED_{xy} = \int_A Exy \, dA$

Table 3.1: Definitions of cross section integrals. Note that A_0 should be integrated over the surface contour lines described by $y(x)$ in order to obtain the enclosed area. sgn denotes the sign of y. A refers to areas where material is present. E is the elastic modulus and ρ the mass density.

Assuming thin shells with thickness h and uniform properties across them it is possible to switch to line integrals along the shell lines described by $\mathbf{r} = \{x, y(x)\}$. Using the chordwise coordinate x as parameter, the area segment is

$$dA = h \, ds \,, \quad ds = \left\| \frac{d\mathbf{r}}{dx} \right\| dx = \sqrt{1 + \left(\frac{dy(x)}{dx} \right)^2} \, dx \tag{3.1}$$

Where ds is the curve length. Note that airfoil surfaces are usually described by x and $y(x)$ so the integrations are now single integrals over x. x is not a possible parameter if sections are aligned with the y-axis which is the case for the shear webs. In that case y must be used as integration variable and $ds = dy$. The section shell thickness's are defined as

$$h_\alpha = \alpha c \,, \quad h_\beta = \beta c \,, \quad h_\gamma = \gamma c \,, \quad h_\delta = \delta c \tag{3.2}$$

The section mass integral can now be written as

$$m = \int_A \rho h \, ds = \alpha c \rho_\alpha \int_\alpha ds + \beta c \rho_\beta \int_\beta ds + \gamma c \rho_\gamma \int_\gamma ds + \delta c \rho_\delta \int_\delta ds \tag{3.3}$$

The geometrical quantities are made dimensionless by dividing with the chord

$$x^* = \frac{x}{c} \,, \quad y^* = \frac{y}{c} \quad \Rightarrow \quad ds^* = \frac{ds}{c} \tag{3.4}$$

This results in the following expression where the integral may be evaluated numerically

$$m = c \sum_i h_i \rho_i \int_i ds^* = c^2 \sum_i \alpha_i \rho_i \int_i ds^* \tag{3.5}$$

Index i refers to the different sectors and α_i is the given sectors thickness parameter (α, β, γ, δ). The integral is a dimensionless geometrical quantity which depends on the structural shape and the layout of the sectors. Note that the integration over the α sector includes two integrals - one on the pressure side and one on the suction side. In the same way the integrations over the other sectors are divided into sub-integrals each having a monotonically increasing integration variable. Repeating the procedure for all structural integrals yields the dimensionless coefficients in Table 3.2.

$C_{A_0} = \int_i \operatorname{sgn}(y^*) y^* \, dx^*$

$C_{A_i} = \int_i ds^*$

$C_{S_{x\,i}} = \int_i y^* \, ds^*$

$C_{S_{y\,i}} = \int_i x^* \, ds^*$

$C_{I_{x\,i}} = \int_i {y^*}^2 \, ds^*$

$C_{I_{y\,i}} = \int_i {x^*}^2 \, ds^*$

$C_{D_{xy\,i}} = \int_i x^* y^* \, ds^*$

Table 3.2: Dimensionless geometrical quantities. These should be calculated using a coordinate system with origo in EA in order for scaling to be correct.

The structural properties can now be expressed as listed in Table 3.3.

Section area (closed section)	$A_0 = c^2 C_{A_0}$
Section mass	$m = c^2 \sum_i \alpha_i \rho_i C_{A_i}$
Longitudinal stiffness	$EA = c^2 \sum_i \alpha_i E_i C_{A_i}$
Moment of stiffness about the x axis	$ES_x = c^3 \sum_i \alpha_i E_i C_{S_{x\,i}}$
Moment of stiffness about the y axis	$ES_y = c^3 \sum_i \alpha_i E_i C_{S_{y\,i}}$
Moment of mass about the x axis	$\rho S_x = c^3 \sum_i \alpha_i \rho_i C_{S_{x\,i}}$
Moment of mass about the y axis	$\rho S_y = c^3 \sum_i \alpha_i \rho_i C_{S_{y\,i}}$
Moment of stiffness inertia about the x axis	$EI_x = c^4 \sum_i \alpha_i E_i C_{I_{x\,i}}$
Moment of stiffness inertia about the y axis	$EI_y = c^4 \sum_i \alpha_i E_i C_{I_{y\,i}}$
Moment of centrifugal stiffness	$ED_{xy} = c^4 \sum_i \alpha_i E_i C_{D_{xy\,i}}$

Table 3.3: Cross section properties based on dimensionless coefficients.

The coefficients have been calculated numerically based on the geometry of the

NACA 34xx airfoil series using defined values of $x_1 \ldots x_5$. The resulting set of coefficients depends on thickness and are given in Section 3.8. An example of analytical expressions for the coefficients is given in Section 3.6.

The center of gravity and the center of mass are found as (note that x_{EA}=0 if the coefficients are correctly calibrated)

$$x_{EA} = \frac{ES_y}{EA} \quad y_{EA} = \frac{ES_x}{EA} \tag{3.6}$$

$$x_{CG} = \frac{\rho S_y}{m} \quad y_{CG} = \frac{\rho S_x}{m} \tag{3.7}$$

3.3 Principal axes

The 1st principal axis is rotated by the angle ν

$$\nu = \frac{1}{2}\tan^{-1}\left(\frac{2ED_{xy}}{EI_y - EI_x}\right) \tag{3.8}$$

The 2nd principal axis is perpendicular to the 1st. The bending stiffness's about the principal axes are

$$EI_{x'} = EI_x - ED_{xy}\tan\nu \tag{3.9}$$

$$EI_{y'} = EI_y + ED_{xy}\tan\nu \tag{3.10}$$

3.4 Torsional stiffness

Assuming St. Venant torsion for a single closed cell, i.e. the profile surface shell is assumed to carry all shear forces due to torsion.

$$GJ = \frac{4A_0^2}{\oint \frac{1}{h(s)G(s)}\,ds} \tag{3.11}$$

Rewriting using the α, β, γ definitions

$$1/GJ = \frac{\oint \frac{1}{h(s)G(s)}\,ds}{4A_0^2} \tag{3.12}$$

$$1/GJ = \frac{\frac{1}{\alpha G_\alpha}C_{A_\alpha} + \frac{1}{\beta G_\beta}C_{A_\beta} + \frac{1}{\gamma G_\gamma}C_{A_\gamma}}{4C_{A_0}^2 c^4} \tag{3.13}$$

If the section can not be approximated by a single cell, the method of successive approximations can be used (see [39]), however, the method is iterative and cannot be linearized easily.

3.5 Material parameters

The structural model requires that the user specifies E_{11}, G_{12} and ρ for each sector on the blade. In most cases the material will be a fiber laminate and the values must represent the overall engineering values. This gives considerable flexibility for the user when selecting E_{11} and G_{12}, which depends on the layup. The use of fiber laminates also allows twist-bending coupling, but this is not included in the model. In the laminates, a symmetric fibre layup must therefore be used because it has zero twist-bending coupling.

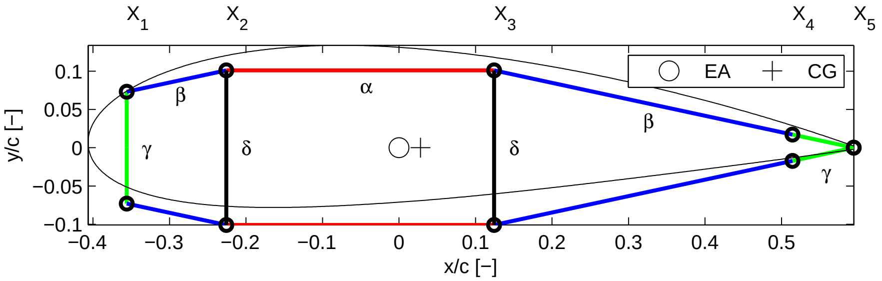

Figure 3.3: Layout of polygon model (t=21%). EA and CG are for the polygon model.

3.6 Polygon model

The geometrical coefficients in Table 3.2 can be determined analytically using the expressions in Table 3.4. The layout corresponds to a polygon model with straight line segments as seen in Figure 3.3. The slope a is defined to make the profile taper off to zero at the trailing edge. Note that the principal axes by definition are aligned with the x and y axes. Note that $x_1 \dots x_5$ now are defined relative to EA, the position of which must be assumed. However, it is relatively safe to assume EA=0.4 relative to the leading edge. t is the relative profile thickness.

a	$-\frac{t}{2(x_5-x_3)}$
b	$\sqrt{1+a^2}$
$C_{A_{0\alpha}}$	$(x_3-x_2)t$
$C_{A_{0\beta}}$	$(x_2-x_1+x_4-x_3)bt$
	$+(3x_1^2+x_4^2+3x_2^2-6x_2x_1+x_3^2-2x_3x_4)ab$
$C_{A_{0\gamma}}$	$(x_5-x_4)bt+(x_5^2-x_4^2-2x_3x_5+2x_3x_4)ab$
$C_{A_{0\delta}}$	0
C_{A_α}	$2(x_3-x_2)$
C_{A_β}	$2(x_2-x_1+x_4-x_3)b$
C_{A_γ}	$t+2(x_5-x_4)b+2(x_2-x_1)a$
C_{A_δ}	$2t$
$C_{I_{x\alpha}}$	${}^1\!/_2(x_3-x_2)t^2$
$C_{I_{x\beta}}$	${}^1\!/_2(x_2-x_1+x_4-x_3)bt^2+(3(x_2-x_1)^2+(x_4-x_3)^2)abt$
	$+({}^{14}\!/_3(x_2-x_1)^3+{}^2\!/_3(x_4-x_3)^3)a^2b$
$C_{I_{x\gamma}}$	$(2b((a(x_5-x_4)+{}^1\!/_2t+a(x_4-x_3))^3-({}^1\!/_2t+a(x_4-x_3))^3))/(3a)$

	$+{}^{2}/_{3}({}^{1}/_{2}t + a(x_2 - x_1))^3$
$C_{I_{x\delta}}$	${}^{1}/_{6}t^3$
$C_{I_{y_\alpha}}$	${}^{2}/_{3}(x_3^3 - x_2^3)$
$C_{I_{y_\beta}}$	${}^{2}/_{3}(x_2^3 - x_1^3 + x_4^3 - x_3^3)b$
$C_{I_{y_\gamma}}$	$x_1^2 t + {}^{2}/_{3}(x_5^3 - x_4^3)b + (2x_2x_1^2 - 2x_1^3)a$
$C_{I_{y_\delta}}$	$(x_2^2 + x_3^2)t$
$C_{S_{y_\alpha}}$	$x_3^2 - x_2^2$
$C_{S_{y_\beta}}$	$(x_2^2 - x_1^2 + x_4^2 - x_3^2)b$
$C_{S_{y_\gamma}}$	$x_1 t + (x_5^2 - x_4^2)b + (2x_1x_2 - 2x_1^2)a$
$C_{S_{y_\delta}}$	$(x_2 + x_3)t$
$C_{D_{xy_\alpha}}$	0
$C_{D_{xy_\beta}}$	0
$C_{D_{xy_\gamma}}$	0
$C_{D_{xy_\delta}}$	0

Table 3.4: The structural coefficients for the polygon model.

3.7 Example: NACA 3421

To validate the model the 5MW NREL reference turbine at r=37.7 m (t=21%) has been used as a test case. The structural layout has been modelled using 3 methods:

1. Numerical integration of coefficients based on the geometry of a NACA 3421 profile.
2. The polygon model for calculation of coefficients.
3. PreComp and the geometry of a NACA 3421 profile. PreComp [40] is a numerical tool for determining cross section properties.

The NREL 5MW turbine uses TU Delft profiles but here the NACA 3421 profile is used because its shape is representative for many airfoils. Results are found in Table 3.5. All 3 models yields results which are close to the target values of the reference turbine. The input parameters have been varied based on assumptions for the structural layout and material parameters until the values for m, EA, EI_x, EI_y and GJ showed good agreement. The model is then considered to be calibrated. Note that the simplified semi-analytical models yield good results but that the polygon model requires some tuning of G.

The value of EA reported in the NREL5MW documentation [18] appears to be very high and a lower value have been assumed instead which appears to be more realistic. EA influences the local spanwise strains and stresses, but besides from that it has very little influence, and the uncertainty has been accepted.

Figure 3.4 shows the properties when the thickness of the α-sector is scaled by f_α. PreComp is considered to be most accurate and the other methods yield good results when compared.

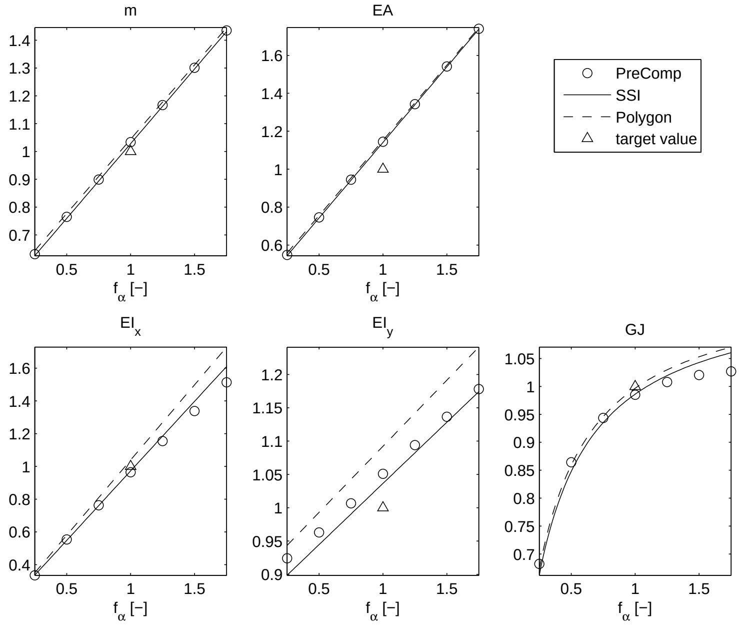

Figure 3.4: A comparison of the results when scaling α with the factor f_α

3.8 Structural coefficients for the NREL 5MW turbine

The process described in Section 3.7 has been repeated for different airfoil thickness, resulting in the following set of coefficients:

Designation	NACA3417	NACA3421	NACA3425	NACA3430	NACA3435	NACA3440	Cylinder
t [%]	1.7000e+001	2.1000e+001	2.5000e+001	3.0000e+001	3.5000e+001	4.0000e+001	1.0000e+002
C_A0_alfa	5.5124e-002	6.7844e-002	8.0862e-002	9.7696e-002	1.1500e-001	1.3046e-001	3.4045e-001
C_A0_beta	5.2422e-002	6.4705e-002	7.7813e-002	9.3985e-002	1.1004e-001	1.2404e-001	3.8565e-001
C_A0_gamm	5.7512e-003	6.5273e-003	7.4610e-003	8.9122e-003	1.0264e-002	1.1569e-002	5.9285e-002
C_A0_delt	0	0	0	0	0	0	0
C_A_alfa	7.0329e-001	7.0364e-001	7.0063e-001	7.0102e-001	7.0421e-001	7.0781e-001	7.1001e-001
C_A_beta	1.0540e+000	1.0641e+000	1.0746e+000	1.0865e+000	1.1017e+000	1.1146e+000	1.2839e+000
C_A_gamm	2.7261e-001	2.8745e-001	3.4040e-001	3.4033e-001	3.6946e-001	3.9734e-001	1.1523e+000
C_A_delt	2.9242e-001	3.6059e-001	4.3210e-001	5.2196e-001	6.1290e-001	6.9282e-001	1.8753e+000
C_Ix_alfa	4.3614e-003	6.6011e-003	9.4330e-003	1.3798e-002	1.9102e-002	2.4551e-002	1.7023e-001
C_Ix_beta	3.0281e-003	4.6085e-003	6.6647e-003	9.8241e-003	1.3651e-002	1.7629e-002	1.9283e-001
C_Ix_gamm	2.4869e-004	3.4820e-004	4.9023e-004	7.3366e-004	1.0586e-003	1.4318e-003	2.9643e-002
C_Ix_delt	5.2832e-004	9.8754e-004	1.6972e-003	2.9877e-003	4.8340e-003	6.9774e-003	1.3739e-001
C_Iy_alfa	8.9966e-003	8.2903e-003	7.9196e-003	8.0577e-003	8.1784e-003	7.6762e-003	7.2741e-003
C_Iy_beta	1.1361e-001	1.1910e-001	1.2191e-001	1.2210e-001	1.2419e-001	1.3109e-001	1.2815e-001
C_Iy_gamm	5.8725e-002	6.1096e-002	6.9610e-002	6.9790e-002	7.4295e-002	7.8053e-002	2.5844e-001
C_Iy_delt	1.0081e-002	1.1897e-002	1.3895e-002	1.7027e-002	1.9959e-002	2.1976e-002	5.6643e-002
C_Dxy_alfa	8.3234e-005	1.0531e-004	1.2147e-004	1.7312e-004	1.6142e-004	2.0193e-004	5.3480e-004
C_Dxy_beta	-8.4465e-004	-1.0674e-003	-1.0595e-003	-1.1011e-003	-1.1660e-003	-1.1758e-003	6.0500e-004
C_Dxy_gamm	-3.4157e-004	-4.1661e-004	-3.1042e-004	-6.2714e-004	-7.6367e-004	-1.1894e-003	9.3861e-005
C_Dxy_delt	1.5784e-004	2.0172e-004	2.1477e-004	2.4017e-004	2.3416e-004	2.4411e-004	-1.7795e-004
C_Sx_alfa	2.6807e-003	2.2678e-003	2.1356e-003	2.0437e-003	2.2753e-003	1.1591e-003	-2.7710e-007
C_Sx_beta	-4.2287e-003	-5.3971e-003	-4.1186e-003	-3.5485e-003	-3.4051e-003	-3.3476e-003	-2.1460e-006
C_Sx_gamm	-4.6190e-003	-4.7668e-003	-5.0928e-003	-4.4463e-003	-4.1570e-003	-3.4124e-003	1.1952e-006
C_Sx_delt	2.4179e-004	1.3353e-005	2.5686e-004	3.4264e-004	4.9414e-004	1.6570e-004	-7.3188e-007
C_Sy_alfa	-3.5268e-002	-2.7316e-002	-2.3568e-002	-2.5581e-002	-2.6219e-002	-1.6491e-002	4.1162e-004
C_Sy_beta	1.7383e-001	1.8641e-001	1.9254e-001	1.9045e-001	1.9236e-001	2.0717e-001	1.7915e-003
C_Sy_gamm	8.7910e-003	5.4370e-003	-9.6036e-003	-7.5650e-003	-1.7439e-002	-2.0861e-002	-1.1645e-003
C_Sy_delt	-1.7427e-002	-1.7604e-002	-1.8307e-002	-2.3885e-002	-2.8138e-002	-2.3075e-002	1.0872e-003
x1/c	5.0000e-002	5.0000e-002	5.0000e-002	5.0000e-002	5.0000e-002	5.0000e-002	8.0000e-002
x2/c	1.8000e-001	1.8000e-001	1.8000e-001	1.8000e-001	1.8000e-001	1.8000e-001	3.2500e-001
x3/c	5.3000e-001	5.3000e-001	5.3000e-001	5.3000e-001	5.3000e-001	5.3000e-001	6.7500e-001
x4/c	9.2000e-001	9.2000e-001	9.2000e-001	9.2000e-001	9.2000e-001	9.2000e-001	9.2000e-001
x5/c	9.8000e-001	9.8000e-001	9.8000e-001	9.8000e-001	9.8000e-001	9.8000e-001	1.0000e+000
alfa_0	6.0000e-003	8.0000e-003	8.0000e-003	7.2000e-003	6.0000e-003	1.0500e-002	6.0000e-003
beta_0	3.0000e-003	3.0000e-003	3.0000e-003	3.0000e-003	3.0000e-003	3.0000e-003	7.0000e-003
gamm_0	3.0000e-003	3.0000e-003	3.0000e-003	3.0000e-003	3.0000e-003	3.0000e-003	8.0000e-003
delt_0	3.0000e-003	3.0000e-003	3.0000e-003	3.0000e-003	3.0000e-003	3.0000e-003	0
x_EA	4.0584e-001	3.9450e-001	3.8856e-001	3.9146e-001	3.9160e-001	3.7848e-001	4.9942e-001
y_EA	2.3190e-002	2.4263e-002	2.4129e-002	2.4536e-002	2.5040e-002	2.5736e-002	3.9028e-007
x_CG	4.3713e-001	4.2276e-001	4.1595e-001	4.1834e-001	4.1861e-001	4.0102e-001	4.9967e-001
y_CG	2.2118e-002	2.3120e-002	2.3251e-002	2.3779e-002	2.4320e-002	2.5194e-002	7.3218e-008

Note that the values of $x_1 \ldots x_5$ were varied until good agreement with the reference data for e.g. EI_x was obtained. This also included tuning of E, G, ρ and α_i.

		NREL 5MW t=0.21	PreComp	Numerical	Polygon
x_1	-		0.05	0.05	0.05
x_2	-		0.18	0.18	0.18
x_3	-		0.53	0.53	0.53
x_4	-		0.92	0.92	0.92
α	-		0.008	0.008	0.008
β	-		0.003	0.003	0.003
γ	-		0.003	0.003	0.003
δ	-		0.003	0.003	0.003
ρ_α	$\mathrm{kg/m^3}$		1800.0	1800.0	1800.0
ρ_β	$\mathrm{kg/m^3}$		1800.0	1800.0	1800.0
ρ_γ	$\mathrm{kg/m^3}$		1800.0	1800.0	1800.0
ρ_δ	$\mathrm{kg/m^3}$		1800.0	1800.0	1800.0
E_α	Pa		37.0e9	37.0e9	37.0e9
E_β	Pa		15.0e9	15.0e9	15.0e9
E_γ	Pa		30.0e9	30.0e9	30.0e9
E_δ	Pa		15.0e9	15.0e9	15.0e9
G_α	Pa		2.3e9	2.3e9	2.5e9
G_β	Pa		2.3e9	2.3e9	2.5e9
G_γ	Pa		2.3e9	2.3e9	2.5e9
G_δ	Pa		2.3e9	-	-
x_{SC}	-		0.397	-	-
x_{EA}	-		0.400	0.395	0.406
x_{CG}	-		0.427	0.423	0.433
m	kg/m	220.6	228.0	227.1	230.3
EA	N	3.06e9	3.502e9	3.496e9	3.52e9
EI_x	$\mathrm{Nm^2}$	3.15e8	3.037e8	3.073e8	3.273e8
EI_y	$\mathrm{Nm^2}$	1.83e9	1.923e9	1.902e9	1.999e9
GJ	$\mathrm{Nm^2}$	4.59e7	4.521e7	4.540e7	4.575e7
ν	deg.		-0.438	-0.224	0
$EI_{x'}$	$\mathrm{Nm^2}$		-	3.073e8	-
$EI_{y'}$	$\mathrm{Nm^2}$		-	1.902e9	-

Table 3.5: Comparison of model input data and results when modeling the properties of the 5MW NREL reference turbine at r=37.7 m (t=21%). The upper part of the table is input data and lower the output of the models.

3.9 Matrix representation

Often $\nu \approx 0$ and it is not necessary to use the principal axes. In that case the following linear representation can be used to obtain the properties in the coordinate axes.

$$\underbrace{\begin{bmatrix} m \\ EA \\ EI_x \\ EI_y \end{bmatrix}}_{\mathbf{y}} = \underbrace{\begin{bmatrix} c^2 & 0 & 0 & 0 \\ 0 & c^2 & 0 & 0 \\ 0 & 0 & c^4 & 0 \\ 0 & 0 & 0 & c^4 \end{bmatrix}}_{\mathbf{C}} \underbrace{\begin{bmatrix} \rho_\alpha C_{A_\alpha} & \rho_\beta C_{A_\beta} & \rho_\gamma C_{A_\gamma} & \rho_\delta C_{A_\delta} \\ E_\alpha C_{A_\alpha} & E_\beta C_{A_\beta} & E_\gamma C_{A_\gamma} & E_\delta C_{A_\delta} \\ E_\alpha C_{I_{x\alpha}} & E_\beta C_{I_{x\beta}} & E_\gamma C_{I_{x\gamma}} & E_\delta C_{I_{x\delta}} \\ E_\alpha C_{I_{y\alpha}} & E_\beta C_{I_{y\beta}} & E_\gamma C_{I_{y\gamma}} & E_\delta C_{I_{y\delta}} \end{bmatrix}}_{\mathbf{A}} \underbrace{\begin{bmatrix} \alpha \\ \beta \\ \gamma \\ \delta \end{bmatrix}}_{\mathbf{x}} \tag{3.14}$$

The matrix formulation can be extended to include the torsional stiffness:

$$\begin{bmatrix} \mathbf{y} \\ 1/GJ \end{bmatrix} = \begin{bmatrix} \mathbf{C} & \mathbf{0} \\ \mathbf{0} & c^{-4} \end{bmatrix} \begin{bmatrix} \mathbf{A} & \mathbf{0} & \mathbf{0} & \mathbf{0} \\ \mathbf{0} & \frac{C_{A_\alpha}}{G_\alpha 4C^2_{A_0}} & \frac{C_{A_\beta}}{G_\beta 4C^2_{A_0}} & \frac{C_{A_\gamma}}{G_\gamma 4C^2_{A_0}} \end{bmatrix} \underbrace{\begin{bmatrix} \mathbf{x} \\ 1/\alpha \\ 1/\beta \\ 1/\gamma \end{bmatrix}}_{\mathbf{x}_2} \tag{3.15}$$

Note that the coefficients in $\mathbf{x}_2$ are not independent. In terms of the absolute shell thicknesses the result is

$$\mathbf{y} = \underbrace{\begin{bmatrix} c & 0 & 0 & 0 \\ 0 & c & 0 & 0 \\ 0 & 0 & c^3 & 0 \\ 0 & 0 & 0 & c^3 \end{bmatrix}}_{\mathbf{D}} \mathbf{A} \underbrace{\begin{bmatrix} h_\alpha \\ h_\beta \\ h_\gamma \\ h_\delta \end{bmatrix}}_{\mathbf{h}} \tag{3.16}$$

Likewise, GJ will also scale with c^3 for fixed shell thickness (for the assumed single-cell torsion).

3.10 Alternative formulations

Some alternative simplified structural formulations which may be usefull, but not used in this project, is described below. They are based on taylor expansions and there are therefore no requirements on the cross section layout. h is rewritten

$$h = h_r + \Delta h \tag{3.17}$$

where h_r is a reference value for an existing blade and Δh is an absolute change. The equations can now be rewritten as

$$\mathbf{y} = \mathbf{D}\mathbf{y}_0 + \mathbf{D}\mathbf{A}\underbrace{\begin{bmatrix} \Delta h_\alpha \\ \Delta h_\beta \\ \Delta h_\gamma \\ \Delta h_\delta \end{bmatrix}}_{\mathbf{z}}, \quad \mathbf{y_0} = \mathbf{D}_r^{-1}\mathbf{y}_r \tag{3.18}$$

where $\mathbf{y}_0$ includes the reference values corresponding to unit chord and Δ denotes an absolute change of material thickness. This form has the advantage that the reference values are included directly in $\mathbf{y_r}$ and the layout will therefore be close to the reference values.

Linear Taylor expansion

Equation (3.18) is equivalent to a first order Taylor expansion around $\mathbf{y}_0$ in which $\mathbf{DA}$ contains the Taylor coefficients. The Taylor coefficients are the partial derivatives and these may be calculated using finite differences, which can be determined using e.g. FEM models. For instance, consider the section mass which, for an arbitrary chord c_r, can be approximated as

$$m = m_r + \left.\frac{\partial m}{\partial h_\alpha}\right|_{h_{\alpha_r}} \Delta h_\alpha + \left.\frac{\partial m}{\partial h_\beta}\right|_{h_{\beta_r}} \Delta h_\beta + \left.\frac{\partial m}{\partial h_\gamma}\right|_{h_{\gamma_r}} \Delta h_\gamma + \left.\frac{\partial m}{\partial h_\delta}\right|_{h_{\delta_r}} \Delta h_\delta \tag{3.19}$$

This is equivalent to the form

$$\mathbf{y} = \mathbf{y}_r + \mathbf{A}_r\mathbf{z} \tag{3.20}$$

where $\mathbf{A}_r$ is defined as

$$\mathbf{A}_r = \begin{bmatrix} \left.\frac{\partial m}{\partial h_\alpha}\right|_{h_{\alpha_r}} & \left.\frac{\partial m}{\partial h_\beta}\right|_{h_{\beta_r}} & \left.\frac{\partial m}{\partial h_\gamma}\right|_{h_{\gamma_r}} & \left.\frac{\partial m}{\partial h_\delta}\right|_{h_{\delta_r}} \\ \left.\frac{\partial EA}{\partial h_\alpha}\right|_{h_{\alpha_r}} & \left.\frac{\partial EA}{\partial h_\beta}\right|_{h_{\beta_r}} & \left.\frac{\partial EA}{\partial h_\gamma}\right|_{h_{\gamma_r}} & \left.\frac{\partial EA}{\partial h_\delta}\right|_{h_{\delta_r}} \\ \left.\frac{\partial EI_x}{\partial h_\alpha}\right|_{h_{\alpha_r}} & \left.\frac{\partial EI_x}{\partial h_\beta}\right|_{h_{\beta_r}} & \left.\frac{\partial EI_x}{\partial h_\gamma}\right|_{h_{\gamma_r}} & \left.\frac{\partial EI_x}{\partial h_\delta}\right|_{h_{\delta_r}} \\ \left.\frac{\partial EI_y}{\partial h_\alpha}\right|_{h_{\alpha_r}} & \left.\frac{\partial EI_y}{\partial h_\beta}\right|_{h_{\beta_r}} & \left.\frac{\partial EI_y}{\partial h_\gamma}\right|_{h_{\gamma_r}} & \left.\frac{\partial EI_y}{\partial h_\delta}\right|_{h_{\delta_r}} \end{bmatrix} \tag{3.21}$$

However, (3.20) is for a fixed chord $c{=}c_r$ and it is necessary to scale to other chords. Comparing Equation (3.20) and (3.16) yields

$$\mathbf{y_0} = \mathbf{A}\mathbf{h} = \mathbf{D}_r^{-1}\left(\mathbf{y_r} + \mathbf{A}_r\mathbf{z}\right) \tag{3.22}$$

In short

$$\mathbf{y} = \mathbf{DD}_r^{-1} \left(\mathbf{y}_r + \mathbf{A}_r \mathbf{z} \right) \tag{3.23}$$

The advantage of this formulation is that $\mathbf{A}_r$ can be determined using FEM for an arbitrary internal layout (i.e. different numbers of spars, varying geometry etc.). It is also valid for thick shells as long as the thickness is not varied too much. $\mathbf{y}$ will take values around the linearization point, i.e. the blade reference values which may be an advantage.

Note that $\mathbf{DD}_r^{-1}$ represents a scaling around the reference chord, e.g. c/c_r. This means that the formulation is not necessarily based on a unit chord, which could introduce large errors when scaled up to the actual chord. This is especially important for the torsion stiffness properties because it is not known how it scales in the general case and one have to rely on the chord scaling laws for the linearized model.

Higher order Taylor expansion

The torsion can be described using higher order Taylor expansions. This is also useful if the wall thickness's changes significantly. In the following assume that only the main spar thickness will be changed. A Taylor expansion of GJ is

$$GJ = GJ_r + \left. \frac{dGJ}{dh_\alpha} \right|_{h_{\alpha_0}} \Delta h_\alpha + \frac{1}{2} \left. \frac{d^2 GJ}{dh_\alpha^2} \right|_{h_{\alpha_0}} \Delta h_\alpha^2 + \dots \tag{3.24}$$

It is assumed that the torsion stiffness follows the same scaling law as found for the single cell torsion.

$$\begin{bmatrix} m \\ EA \\ EI_x \\ EI_y \\ GJ \end{bmatrix} = \mathbf{DD}_r^{-1} \left(\begin{bmatrix} \frac{\partial m}{\partial h_\alpha} & \frac{1}{2}\frac{\partial^2 m}{\partial h_\alpha^2} & \cdots \\ \frac{\partial EA}{\partial h_\alpha} & \frac{1}{2}\frac{\partial^2 EA}{\partial h_\alpha^2} & \cdots \\ \frac{\partial EI_x}{\partial h_\alpha} & \frac{1}{2}\frac{\partial^2 EI_x}{\partial h_\alpha^2} & \cdots \\ \frac{\partial EI_y}{\partial h_\alpha} & \frac{1}{2}\frac{\partial^2 EI_y}{\partial h_\alpha^2} & \cdots \\ \frac{\partial GJ}{\partial h_\alpha} & \frac{1}{2}\frac{\partial^2 GJ}{\partial h_\alpha^2} & \cdots \end{bmatrix} \begin{bmatrix} \Delta h_\alpha \\ \Delta h_\alpha^2 \\ \vdots \end{bmatrix} + \mathbf{y}_r \right) \tag{3.25}$$

This is on the same form as Equation (3.23). The partial derivatives can be calculated using finite differences based on FEM calculations with small perturbations on h_α.

3.11 Scaling laws

The cross section properties for a given profile of thickness t is described in the previous sections. Some useful approximate expressions for simple scaling is defined in the following. These are useful for understanding how the basic properties varies, and some simple conclusions are made.

Scaling with thickness, changing shell thickness

Consider airfoils where the y coordinate can be scaled from a reference airfoil of thickness t_{ref} to an airfoil of thickness t (e. g. Naca four digit airfoils without camber)

$$y = y_{ref}(x)\frac{t}{t_{ref}} \tag{3.26}$$

Calculating the area result in

$$A = \int 1\,dy\,dx = \frac{t}{t_{ref}}\int_A 1\,dy_{ref}\,dx = \frac{t}{t_{ref}}A_{ref} \tag{3.27}$$

Note that constant chord is assumed. The material absolute thickness measured in the y-direction becomes (notice that this is a poor measure of the actual thickness near the leading and trailing edge)

$$h_y = f\frac{t}{t_{ref}}h_{y,ref} \tag{3.28}$$

Where $f = h/h_{ref}$ is a factor which is introduced in order to scale all material thickness's (h_α, h_β, h_γ, h_δ). In the same way the following scaling rules can be made

$$m = f\frac{t}{t_{ref}}m_{ref} \tag{3.29}$$

$$EI_x = f\left(\frac{t}{t_{ref}}\right)^3 EI_{x,ref} \tag{3.30}$$

$$EI_y = f\frac{t}{t_{ref}}EI_{y,ref} \tag{3.31}$$

This scaling is exact but it is restricted by the entire structure being deformed in the y-direction.

Approximate scaling laws

Scaling using constant absolute shell thickness

Note that on horizontal planes such as the main carrying spar h_y is very close to the actual material thickness h. The absolute thickness there can be kept unchanged by setting $f{=}t_{ref}/t$ resulting in

$$EI_x = \left(\frac{t}{t_{ref}}\right)^2 EI_{x,ref} \quad \text{Constant abs. shell thickness} \tag{3.32}$$

This is only possible because EI_x depends mainly on the main carrying spar and whether or not the thickness of the other sectors change is not important. However it will be important for the mass and in the following it is assumed that all sectors have unchanged absolute thickness. The circumference of the NACA 34xx series is approximately

$$l = ((\pi - 2)t^{1.8} + 2)c \tag{3.33}$$

Assuming that the mass is proportional to the surface size, it follows that it scales with thickness as

$$m = \frac{(\pi - 2)t^{1.8} + 2}{(\pi - 2)t_{ref}^{1.8} + 2} m_{ref} \quad \text{Constant abs. shell thickness} \tag{3.34}$$

The stiffness to mass ratio for scaling then becomes

$$\frac{EI_x}{m} = \frac{EI_{x,ref}}{m_{ref}} \frac{t^2}{t_{ref}^2} \frac{(\pi - 2)t_{ref}^{1.8} + 2}{(\pi - 2)t^{1.8} + 2} \approx \frac{EI_{x,ref}}{m_{ref}} \frac{t^2}{t_{ref}^2} \quad \text{Constant abs. shell thickness} \tag{3.35}$$

Scaling to different shell thickness and chord

From the linear structural model it follows that

$$EI_x = \frac{h}{h_{ref}} \left(\frac{c}{c_{ref}}\right)^3 \left(\frac{t}{t_{ref}}\right)^2 EI_{x,ref} \tag{3.36}$$

Note that EI_x does not scale with c^4 because the absolute thickness's are constant and does not scale linearly. It is also noted that all sectors are scaled, which may not be what is wanted. If h/h_{ref} refers to a change in the main carrying spar only, then the expression still holds because of the small influence from the other sectors. The mass relation becomes

$$m = \frac{h}{h_{ref}} \frac{c}{c_{ref}} \frac{(\pi - 2)t^{1.8} + 2}{(\pi - 2)t_{ref}^{1.8} + 2} m_{ref} \approx \frac{h}{h_{ref}} \frac{c}{c_{ref}} m_{ref} \tag{3.37}$$

Note that this is a bad approximation if only the thickness of the main carrying spar is changed. In the example seen in Figure 3.4 it is noted that for a relative change in the main carrying spar thickness of $^{h}/_{h_{ref}}$=1.5 the corresponding scaling of mass is only 1.3. This scaling law can be expressed as

$$m = \left({}^{3}/_{5} \frac{h_\alpha}{h_{\alpha,ref}} + {}^{2}/_{5} \right) \frac{c}{c_{ref}} \frac{(\pi - 2)t^{1.8} + 2}{(\pi - 2)t_{ref}^{1.8} + 2} m_{ref} \approx \left({}^{3}/_{5} \frac{h_\alpha}{h_{\alpha,ref}} + {}^{2}/_{5} \right) \frac{c}{c_{ref}} m_{ref} \tag{3.38}$$

But it will depend on the specific structural layup. The stiffness to mass ratio is

$$\frac{EI_x}{m} \approx \frac{EI_{x,ref}}{m_{ref}} \left(\frac{t}{t_{ref}} \right)^2 \left(\frac{c}{c_{ref}} \right)^2 \tag{3.39}$$

Or using (3.38)

$$\frac{EI_x}{m} \approx \left({}^{3}/_{5} + {}^{2}/_{5} \frac{h_{\alpha,ref}}{h_\alpha} \right)^{-1} \left(\frac{t}{t_{ref}} \right)^2 \left(\frac{c}{c_{ref}} \right)^2 \frac{EI_{x,ref}}{m_{ref}} \tag{3.40}$$

It is seen that there is only a small dependency on the spar thickness whereas the chord and thickness is very important. It is also seen that if the absolute thickness (t_a=tc) is kept constant, the ratio will not change. The ratio $^{EI}/_{m}$ is important for the eigenfrequencies which will increase with it. Thus, for fixed wall thickness the flapwise eigenfrequencies increases with c and t.

The scaling rule for the edgewise stiffness is

$$EI_y = \frac{h}{h_{ref}} \left(\frac{c}{c_{ref}} \right)^2 EI_{y,ref} \tag{3.41}$$

And the stiffness to mass ratio

$$\frac{EI_y}{m} \approx \frac{EI_{y,ref}}{m_{ref}} \frac{c}{c_{ref}} \tag{3.42}$$

From this it is seen that increasing the chord will also increase the edgewise eigenfrequencies.

Example: Redefine profile thickness

Solving for t in (3.36) yields

$$EI_x = \frac{h}{h_{ref}} \left(\frac{c}{c_{ref}}\right)^3 \left(\frac{t}{t_{ref}}\right)^2 EI_{x,ref} \tag{3.43}$$

$$t = t_{ref} \sqrt{\frac{EI_x}{EI_{x,ref}} \left(\frac{h}{h_{ref}}\right)^{-1} \left(\frac{c}{c_{ref}}\right)^{-3}} \tag{3.44}$$

Maintaining the bending stiffness and decreasing the main spar thickness to e.g. h/h_{ref}=0.66 for constant stiffness and chord yields t=1.23t_{ref}. I.e. a thicker profile is required. The new mass is approximately m=0.8m_{ref} (using (3.38)) Note that if the chord is increased by 10% the result is t=1.07t_{ref}. The stiffness to mass ratio is then increased by 15% which will tend to increase the eigenfrequencies.

3.12 Conclusions

A method has been developed allowing for easy calculation of the cross section structural properties which are relevant for the aeroelastic properties of the blade. This model is based on dimensionless coefficients and have been implemented in a HAWTOPT module.

The model is based on the geometry of a NACA 34xx profile, but it has also been shown that good results can be obtained using a simple polygon model.

The accuracy of the method is acceptable for conceptual design and it has been shown that it is possible to tune the model in order to represent a reference turbine. The tuning involves the selection of material and geometric properties, including the shell thickness. It is subsequently easy to vary parameters such as the chord and the shell thickness of the main carrying spar. The material parameters can also be varied.

Some alternative formulations based on Taylor expansions are also suggested. These models are not used but may be useful in future work.

Some simple scaling laws have been described, which can be used to obtain quantitative results. This provides guidelines for the designer, and approximate calculations of the effects of changing profile thickness, chord and shell thickness, can be made. E.g. increasing the chord or absolute thickness will increase the stiffness to mass ratio, which will increase the blade eigenfrequencies.

CHAPTER 4

Structural model for the blade

The blade is subjected to spanwise, bending, shear and torsional loads. In this chapter it is described how the thickness of the main load carrying spar can be distributed in order to produce a design which is resistant to the worst case quasi steady loads.

The spanwise, shear and torsional loads will be considered to be less important and only bending will be considered in the initial design. The blades will be approximated as slender cantilever beams under relatively small deformations and the simple Bernoulli-Euler beam theory is then sufficient. An aeroelastic code for advanced calculations of e.g. deflections is later used for validation of the design.

Given known structural properties in a section, the next step is to determine the material layout along the blade span. This must be done in order to fulfill a number of criteria such as:

1. Constraint on max tip deflection
2. Constraint on local stress and/or strain
3. It must be a practical solution from a manufacturing point of view
4. Good aeroelastic properties. I.e. a stable design with low fatigue damage.

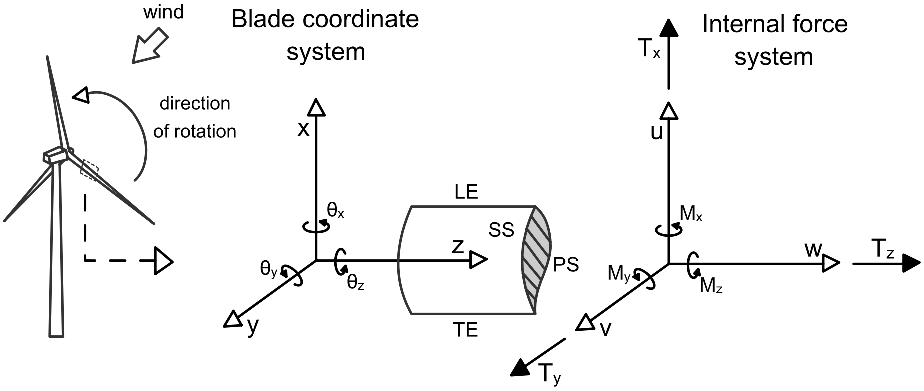

Figure 4.1: Blade coordinate system and sign conventions. LE: Leading edge. TE: Trailing edge. SS: Suction side. PS: Pressure side. u and v measures the edgewise and flapwise deflections.

Item 1 and 2 are directly included in the design process. Item 3 is indirectly included by the user specifying material data and constraints on material thickness. Item 4 is validated in the optimization process.

The layout is made in a simplified manner which takes into account the most important steady state forces and using a Bernoulli-Euler beam model to relate moments and structural properties to a defined deflection shape. This is a simplified model which is selected for a number of reasons: 1) The goal is to make a conceptual structural layout which requires simplicity so that various constraints are easily implemented. 2) Aeroelastic codes predict the full load spectrum and can be used for validation. HAWC2 has been used in this work.

As a first approximation, a layout which ensures a constraint on the tip deflection is used. To take the occurrence of gusts etc. into account, a conservative value should be used (e.g. v^*_{tip}=v_{tip}/R=0.05 – 0.07). To enforce this is in practice, a flapwise deflection shape is specified, and the material is laid out in order to obtain the equivalent curvatures along the span. The specific shape is important for the blade weight and represents an optimization problem. However, if a simple shape is used this can be overcome with a simple parameter-variation (line search). This will be explained in detail in later sections. The edgewise deflection is relaxed, i.e. there is no constraints, which is usually not a problem with turbines in the 5MW range. Further constraints can be put on the shell thickness, which should be within specified limits.

All quantities are defined according to the general rules for a cartesian coordinate system. This makes it easy to transform between coordinate systems. The definitions used is seen in Figure 4.1. Small deformations are assumed so that the z-coordinate can be used as curve-coordinate along the blade. Blade twisting is neglected.

4.1 Definitions

The blade deflections are denoted u, v and w. The curvatures are defined as

$$\kappa_x = \frac{d^2v}{dz^2} \tag{4.1}$$

$$\kappa_y = \frac{d^2u}{dz^2} \tag{4.2}$$

The approximation of angular deformations are

$$\theta_x = -\frac{dv}{dz}\,, \quad \theta_y = \frac{du}{dz} \tag{4.3}$$

$$\frac{d\theta_x}{dz} = -\kappa_x\,, \quad \frac{d\theta_y}{dz} = \kappa_y \tag{4.4}$$

The Bernoulli-Euler relations for simple beam theory then becomes

$$-\kappa_x = \frac{M_x}{EI_x} = \frac{d\theta_x}{dz} \tag{4.5}$$

$$\kappa_y = \frac{M_y}{EI_y} = \frac{d\theta_y}{dz} \tag{4.6}$$

Note that quantities should be defined in the principal coordinate system which is defined relative to the blade chord line which is rotated relative to the blade coordinate system by the twist and tip pitch.

4.2 Flapwise design deflection shape

The design deflection in the y-direction is defined as a third order polynomial.

$$v = az^3 + bz^2 \tag{4.7}$$

$$\frac{d^2v}{dz^2} = 6az + 2b = \kappa_x \tag{4.8}$$

The first and second order derivatives are approximated as the angle and the curvature according to the assumptions in the Bernoulli-Euler beam theory.

The negative values follow from the definition of the right hand rule about the x-axis. It is assumed that the blade follows this shape all the way to the rotor center, even though an actual blade starts a small radial distance away. This polynomial fulfills the clamped boundary conditions that v=0 and θ_x=0 at z=0.

The boundary conditions on the tip deflection and slope are defined using dimensionless numbers

$$\chi = v^*|_{z^*=1}\ , \quad \psi = \left.\frac{dv^*}{dz^*}\right|_{z^*=1}\ , \quad z^* = \frac{z}{R}\,, \quad v^* = \frac{v}{R} \tag{4.9}$$

where χ is the dimensionless tip deflection and ψ is the tip slope (which by definition is dimensionless). This yields a and b

$$a = \frac{\psi - 2\chi}{R^2}\,, \quad b = \frac{3\chi - \psi}{R} \tag{4.10}$$

Normally a positive curvature is wanted along the span and it can be shown that this can be enforced by setting

$$\psi = f\,3\chi\,, \quad f \in [1/2\ 1] \tag{4.11}$$

For a given value of χ, ψ can be selected in order to minimize the blade mass. A typical value is ψ=0.1785 for χ=0.07. The deflection shape can be optimized by using more degrees of freedom but good results have been obtained using the defined polynomial. In practice it is usually found that f has a relatively small influence on the blade mass. Instead it affects the blade eigenfrequencies because the stiffness and mass distribution is shifted. It is also often found that f should be relatively close to 1.0 . This has the unfortunate effect that the curvature near the blade root is almost zero and the required section mass is very large. f=0.95 is a good value which can be used as a first approximation. The design deflection shape for different values of f is seen in Figure 4.2.

4.3 Design loads

The design loads can be calculated in a simple way because the blade is a cantilever beam (clamped-free). The section loads then only depends on the load distribution at larger radii. The bending moment is found by integrating the vector cross moments due to forces at larger radii. This is then a general vector representation of the bending moment and it can easily be transformed to the principal axes using a rotation matrix. Note that this requires the sign of the bending moment to be defined in the general way (see Figure 4.1).

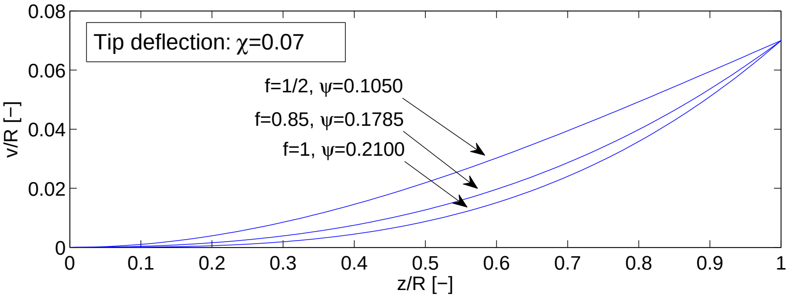

Figure 4.2: Defined design deflection shape for fixed tip deflection and various tip slopes.

External forces

θ is the azimuth angle defined as zero when the blade is pointing directly upwards. The external forces are described as:

Aerodynamic (assumed known):

$$\mathbf{p}_a(z) = \begin{bmatrix} p_{a,x}(z) \\ p_{a,y}(z) \\ p_{a,z}(z) \end{bmatrix} \tag{4.12}$$

Gravity:

$$\mathbf{p}_g(z) = \begin{bmatrix} \sin(\theta) \\ 0 \\ -\cos(\theta) \end{bmatrix} m(z)g \tag{4.13}$$

Centrifugal:

$$\mathbf{p}_c(z) = \begin{bmatrix} 0 \\ 0 \\ 1 \end{bmatrix} m(z)\Omega^2 z \tag{4.14}$$

Total

$$\mathbf{p}(z) = \mathbf{p}_a(z) + \mathbf{p}_g(z) + \mathbf{p}_c(z) \tag{4.15}$$

Note that the aerodynamic loads are the projections of l and d onto the respective directions.

Internal forces

Internal forces at z are described as follows with the tip assumed to be load free.

$$\mathbf{T}(z) = \int_z^R \mathbf{p}(z')\,dz' \tag{4.16}$$

Internal bending moments

With the vector pointing from point at z to point at z'

$$\mathbf{r}(z,z') = \begin{bmatrix} u(z') - u(z) \\ v(z') - v(z) \\ z' - z \end{bmatrix} \tag{4.17}$$

the bending moment at z due to distributed loads at z' is:

$$\mathbf{M}(z) = \int_z^R \mathbf{r}(z,z') \times \mathbf{p}(z')\,dz' \tag{4.18}$$

This integration is performed numerically using the loads defined above, but often the bending moments due to aerodynamics are known from the aerodynamic analysis.

$$\mathbf{M}_a(z) = \begin{bmatrix} -M_f(z) \\ M_e(z) \\ 0 \end{bmatrix} \tag{4.19}$$

The aerodynamic loads should be the largest expected and for PRVS-turbines the quasi-steady loads at rated wind speed can be used even though the forces will be larger under a gust. For stall regulated turbines the largest forces may be found at higher wind speeds. The bending moment due to gravitational loads $\mathbf{M}_g$ and the bending moment due to centrifugal loads $\mathbf{M}_c$, depends on the blade mass and are determined through an iterative process where the mass is updated. The gravitational loads are determined for θ=90^o, which is the blade position where the gravity is in-phase with the aerodynamic loads causing the maximum edgewise bending moment. The total design bending moment is then found as:

$$\mathbf{M}(z) = \begin{bmatrix} M_x(z) \\ M_y(z) \\ M_z(z) \end{bmatrix} = \mathbf{M}_a(z) + \mathbf{M}_g(z) + \mathbf{M}_c(z) \tag{4.20}$$

Note that M_x and M_y are the flapwise and edgewise bending moments. In the aeroelastic optimizations the fatigue loads due to variations in M_x will be minimized.

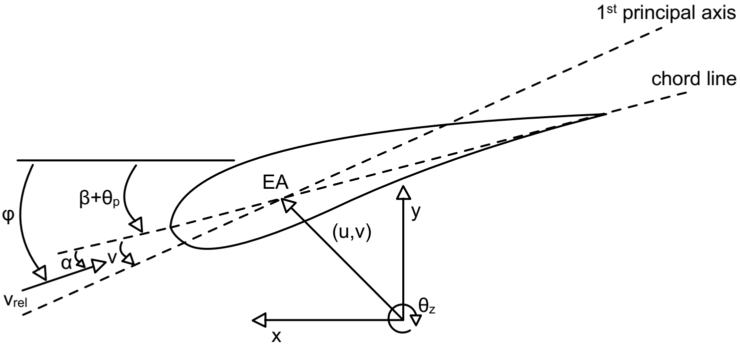

Figure 4.3: Definitions of angles.

4.4 Design measures in principal axes

The design variables are transformed to the principal coordinate system. The rotation angle from blade coordinate system to the principal axis system, is seen in Figure 4.3)

$$\theta_z = -(\beta + \theta_p + \nu) \tag{4.21}$$

Note that the traditional sign of angles is opposite to the general right-hand-rule definition. A coordinate change matrix about the z-axis is defined as:

$$\mathbf{R}_{\theta_z} = \begin{bmatrix} \cos\theta_z & \sin\theta_z \\ -\sin\theta_z & \cos\theta_z \end{bmatrix} \tag{4.22}$$

The design curvatures can then be found in the principal-axis-coordinate system

$$\begin{bmatrix} \frac{d\theta_{x'}}{dz} \\ \frac{d\theta_{y'}}{dz} \end{bmatrix} = \mathbf{R}_{\theta_z} \begin{bmatrix} \frac{d\theta_x}{dz} \\ \frac{d\theta_y}{dz} \end{bmatrix} \tag{4.23}$$

and likewise for the moments

$$\begin{bmatrix} M_{x'} \\ M_{y'} \end{bmatrix} = \mathbf{R}_{\theta_z} \begin{bmatrix} M_x \\ M_y \end{bmatrix} \tag{4.24}$$

The required bending stiffness is then determined using the Bernoulli-Euler assumption

$$EI_{x'} = {}^{M_{x'}}\!/_{\frac{d\theta_{x'}}{dz}} \tag{4.25}$$

$$EI_{y'} = {}^{M_{y'}}\!/_{\frac{d\theta_{y'}}{dz}} \tag{4.26}$$

The material is now laid out in order to obtain this, which also results in other structural properties of the sections, e.g. mass and principal angle. The value of $d\theta_y/dz$ has not been defined because the edgewise deflection shape is relaxed. Instead, its value from the previous iteration should be used in (4.23).

It is often found that ν is small and in that case it is not important for the analysis. However the transformations are still important because the twist and pitch angles can be large.

4.5 Layout of main spar

The shell thickness β, γ and δ are user specified. EI'_x is known from (4.25), and can be transformed back to EI_x using (3.9). Solving for α then yields:

$$EI_{x'} = EI_x - ED_{xy} \tan\nu \tag{4.27}$$

$$\alpha = \frac{EI_x/c^4 - \beta E_\beta C_{I_{x\beta}} - \gamma E_\gamma C_{I_{x\gamma}} - \delta E_\delta C_{I_{x\delta}}}{E_\alpha C_{I_{x\alpha}}} \tag{4.28}$$

An iterative process is now necessary in order to update loads depending on mass and deflections etc.

4.6 Deflection shape

The actual deflection shape may deviate from the design shape because constraints on the material layout means that the actual bending stiffness's are different from (4.25) and (4.26). To calculate the actual deflection the curvatures in the principal system is determined

$$\frac{d\theta_{x'}}{dz} = \frac{M_{x'}}{EI_{x'}} \tag{4.29}$$

$$\frac{d\theta_{y'}}{dz} = \frac{M_{y'}}{EI_{y'}} \tag{4.30}$$

These are then transformed back to the profile coordinate system

$$\begin{bmatrix} \frac{d\theta_x}{dz} \\ \frac{d\theta_y}{dz} \end{bmatrix} = \mathbf{R}_{\theta_z}^{-1} \begin{bmatrix} \frac{d\theta_{x'}}{dz} \\ \frac{d\theta_{y'}}{dz} \end{bmatrix} \tag{4.31}$$

The deflections can now be found by integration of (4.1) and (4.2). Note that this is based on moments which are not updated, and iterations are needed.

	x [-]	y [-]	
$(x_1,\, y_1)$	x_{EA}	0	Leading Edge
$(x_2,\, y_2)$	$(x_{EA} - c)$	0	Trailing Edge
$(x_3,\, y_3)$	$(x_{EA} - x_2)$	$-{}^{tc}/_{2}$	Main laminate, pressure side. Nearest L.E.
$(x_4,\, y_4)$	$(x_{EA} - x_3)$	$-{}^{tc}/_{2}$	Main laminate, pressure side. Nearest T.E.
$(x_5,\, y_5)$	$(x_{EA} - x_2)$	${}^{tc}/_{2}$	Main laminate, suction side. Nearest L.E.
$(x_6,\, y_6)$	$(x_{EA} - x_3)$	${}^{tc}/_{2}$	Main laminate, suction side. Nearest T.E.

Table 4.1: Table of coordinates in a chord aligned system for evaluation of spanwise shear, ϵ_z

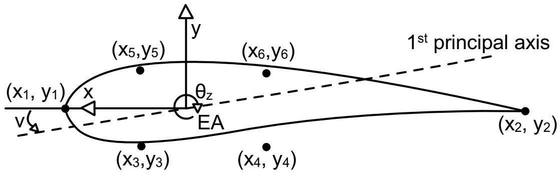

Figure 4.4: Sketch of the defined strain evaluation points.

4.7 Strains

Given an iterated solution, the axial strain in a given point in the principal coordinate system $(x',\, y')$, is given by

$$\epsilon_z = \frac{T_z}{EA} + \frac{M_{x'}}{EI_{x'}} y' - \frac{M_{y'}}{EI_{y'}} x' \tag{4.32}$$

Instead of evaluating in all points over the surface a limited number of evaluation points have been selected. These are defined based on a simplified, assumed profile shape and defined in a coordinate system with origo in EA and with x-axis aligned with the chord and positive direction from trailing to leading edge (see Figure 4.4):

The principal coordinate system is rotated by -ν relative to the chord. Therefore, a coordinate shift matrix is used to project the coordinates. This matrix is defined equivalently to (4.22). E.g.:

$$\begin{bmatrix} x' \\ y' \end{bmatrix} = \mathbf{R}_{-\nu} \begin{bmatrix} x \\ y \end{bmatrix} \tag{4.33}$$

Note that it is also possible to calculate the strains using the curvatures in the chord coordinate system. In that case it is not necessary to rotate the evaluation points but it is instead important to use the correct curvatures (see 4.6).

4.8 Conclusion

In this chapter a method for material layout in the main load carrying spar has been described. The aim is to constrain the extreme quasi steady tip deflection, which is a key constraint in blade design. The method is based on a defined deflection shape and the simplified cross section model presented in Chapter 3. It has been implemented in a HAWTOPT sub module.

Chapter 5

Setup for aeroelastic blade optimization

In this chapter a generalized approach to the turbine optimization is described. The numerical optimizations carried out are very heavy, and for this reason the process has been divided into steps which progressively goes toward more advanced calculations as the design approaches optimum.

The optimizations are based on a reference turbine with defined properties for the blades, tower, nacelle and drive train. The reference turbine used is of the PRVS type and only the blade is optimized. The numerical tools are general but the design approach described in the following is tailored toward PRVS turbines where the single point optimization is useful.

5.1 Outline of optimization process

The optimization is aimed at minimizing an objective value, which in this work is the equivalent fatigue load due to variations in the flapwise bending moment $R_{eq}(M_x)$.

Figure 5.1 shows a flowchart of the optimization process which is divided into the steps described below.

1 Determine key parameters. At the design point this includes the blade mass M, C_P, the inviscous power coefficient $C_{P,l}$, v_{tip}, C_T and fatigue parameters ($R_{eq}(M_x)$). The design point is rated wind speed, which in our case is V_0=11 m/s, λ=6.4. AEP is determined using the whole range of wind speeds between cut-in and cut-out wind speed. $C_{P,l}$ can be calculated using Equation (A.53).

2 Initial single point optimization using constraint on $C_{P,l}$. This is an initial optimization in order to determine design C_l. It is possible to neglect drag because it mainly affects the power. I.e. if the turbine operates away from the design angle of attack where the lift to drag ratio is high, the overall 3D aerodynamics is not changed and the drag primarily generates a negative torque around the rotor shaft. The design will be optimized for a different lift coefficient which is optimum for the structural and aeroelastic properties. The drag may simply be defined to be zero in the aerodynamic data for the airfoils, but it is easier to monitor $C_{P,l}$.

3 Select a new set of airfoils which has good drag characteristics in the relevant range of C_l.

4 Single point optimization using airfoils with good performance at design C_l. C_P is constrained to reference value.

5 Power curve optimization for final design. AEP is constrained to reference value. It is expected that the single point optimizations yields a blade which can generate an AEP within a few percent of the reference turbine. However, because AEP is extremely important, a fine tuning of the design is carried out.

6 Validation of design based on full set of IEC loadcases. In case there is a problem with stability, fatigue issues, extreme loads etc. the objective must be changed to take this into account and the procedure is repeated from 1.

All point optimizations were initialized by minimizing the turbulence sensitivity c_1 (Section 5.4) in the blade root. The design was then further improved by evaluating $R_{eq}(M_x)$ using 100 second aeroelastic calculations based on design load case (DLC) 1 in Table 5.2. The optimization procedure takes advantage of some general conclusions from Chapter 2. I.e. that the overall 3D aerodynamics can be determined independent of drag and that it is possible to change c if cC_l is kept constant.

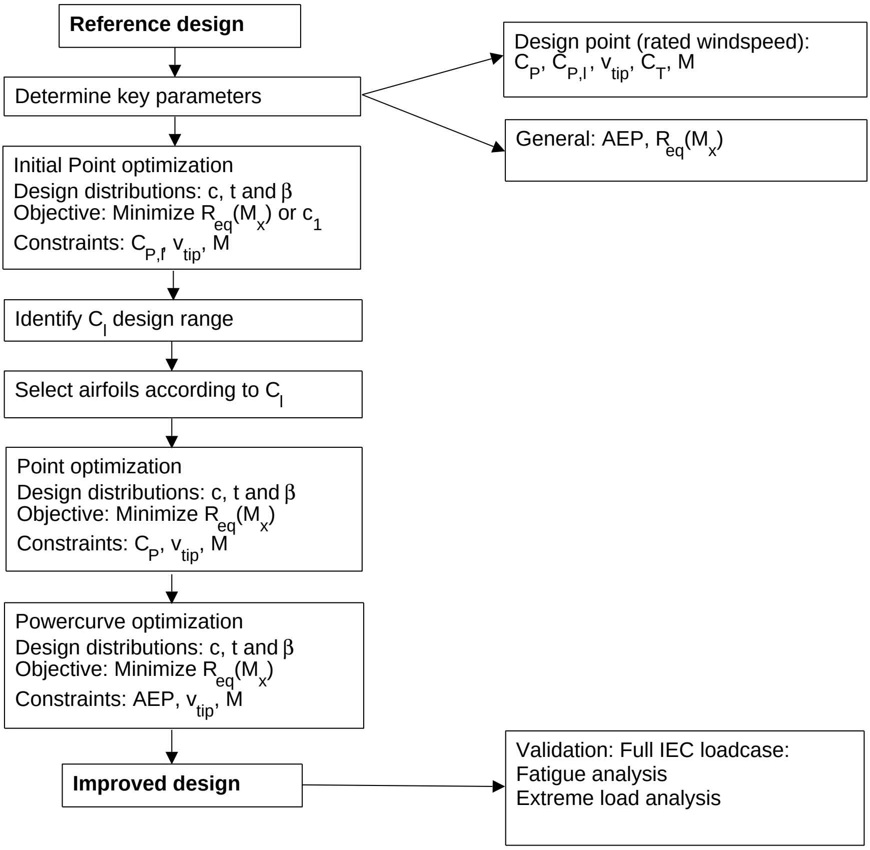

Figure 5.1: Flowchart for the optimization process

The single point optimizations are carried out at rated wind speed (11 m/s). The quasi steady loads are largest at that wind speed, and this is therefore also the design wind speed for the structural layout. Note that this is the case for pitch regulated variable speed turbines, but it may not necessarily be so for stall regulated turbines. Considering only one wind speed enhances numerical stability and speed. Selecting the rated wind speed corresponds to a relatively low λ and thrust coefficient, and is different from the usual approach, where turbines are designed for high aerodynamic efficiency at high λ, which corresponds to low wind speeds. However, designing at rated wind speed makes it possible to optimize for low bending moments under the conditions which dictates the quasi-steady structural requirements.

The optimization software HAWTOPT was used for optimization. The design variables are the distributions of chord, twist and relative thickness. These distributions are defined using 8-point Bezier-curves in order to obtain smooth curves. Twist and thickness distributions are relatively simple curves which can be defined using fewer Bezier-points leading to a reduction in simulation time. The optimization algorithm is the Sequential Linear Programming method [41]. This is less stable than the Method of Feasible Directions [41] but requires only 1/3 of the optimization-iterations and is therefore considerably faster.

Figure 5.2 shows a flowchart for the optimization tool, which consists of an optimizer coupled to various modules. $\mathrm{BEM_{cor}}$ is used for quasi-steady aerodynamic calculations. The structural model is defined in Chapter 4 and yields M and the input for aeroelastic simulations. These are carried out using HAWC2 and result in equivalent fatigue loads R_{eq}. The setup for the aeroelastic calculations will be discussed in Section 5.2. c_1 is a fatigue sensitivity parameter which is defined in Section 5.4.

5.2 Aeroelastic simulations (HAWC2)

The aeroelastic code HAWC2 [37] is used for calculations in the time domain. It uses a multi body formulation based on Timoschenko beam elements to represent all structural members of the turbine. The aerodynamics are calculated using an unsteady BEM method with dynamic wake and stall effects included, and turbulence is described using the Mann turbulence model. All features will not be mentioned here but it is noted that HAWC2 is a state-of-the-art tool.

Aeroelastic calculations are not trivial. A well defined model is required and in order for the aeroelastic response to be correct, it is among other things necessary that the turbine eigenfrequencies are correct. The HAWC2 model has

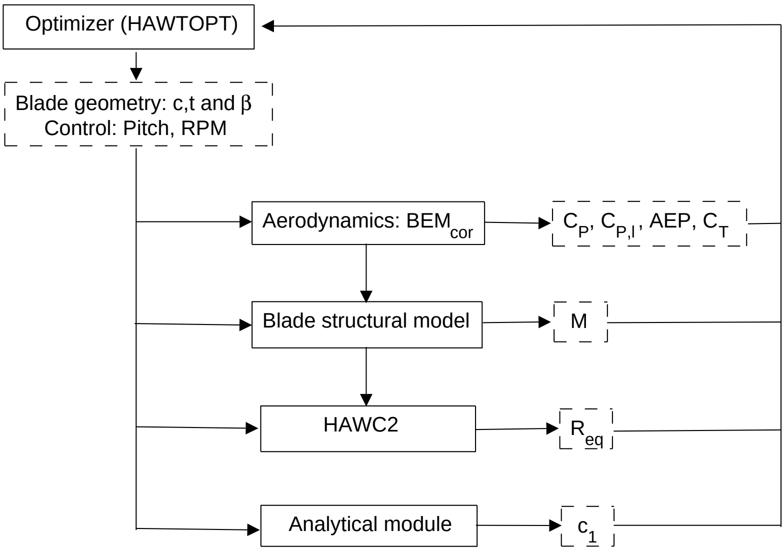

Figure 5.2: Flowchart for the optimization software based on HAWTOPT

been calibrated and validated according to this. The model include all structural members (tower, drive train, blades etc.) but only the blade properties are changed during the optimization. The simplified blade layout method described in earlier chapters yields realistic blade eigenfrequencies and it is therefore believed that realistic aeroelastic simulations can be made.

The blade geometry is defined by putting the $1/2$-chord point on the pitch axis. This increased the numerical stability but unfortunately the obtained designs are restricted to this layout. If e.g. a different sweep was used the fatigue loads could have been decreased due to passive load reduction. The simplified structural model do not yield the shear center and aerodynamic center (SC and AC) and it is assumed that these are in SC=$0.4c$ and AC=$0.25c$. The shear factors are defined to be k_x=0.52 and k_y=0.52 (Ref. [37]).

The control algorithm which was found to give good results for the reference turbine was also used in all optimizations. The control will not be described here but it is noted that the tip speed was limited to 70 m/s. In general, the control will influence the loading and therefore it can be optimized, but this is out of the scope of this work. Instead focus is on load cases where the control is less important.

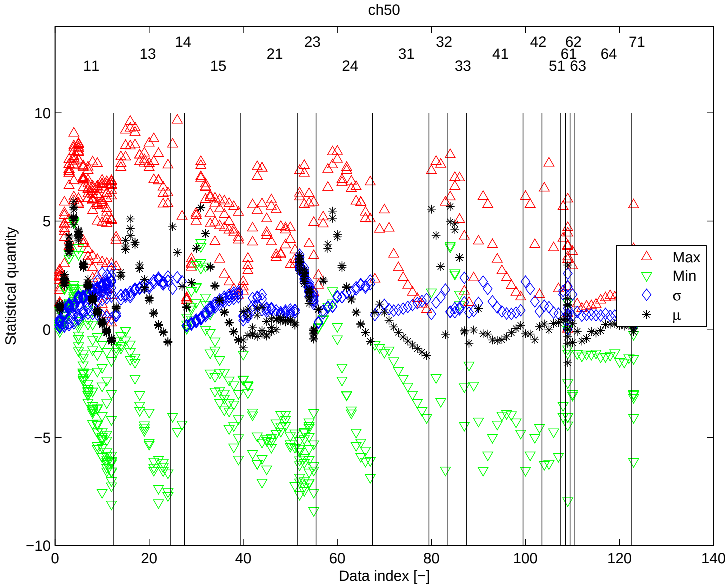

Figure 5.3: Statistical properties of the tip deflection [m] (positive downwind), for the NREL5MW turbine. The numbers refer to IEC loadcases. E.g. 11 is DLC 1.1 .

5.2.1 Reduced set of design load cases

Depending on the optimization objective it is useful to select a limited number of design load cases (DLC's). These must be selected in order to represent the operating conditions under which the objective is important.

A full loadcase calculation according to the IEC standard 61400-1 [42] has been carried out. Figure 5.3, 5.4 and 5.5 shows resulting statistical properties of the tip deflection, root flapwise bending moment and root edgewise bending moment. The numbers in the figures refers to DLC's in the standard. E.g. 13 is DLC 1.3 . Figure 5.6 shows the mean wind speeds. Based on the results a set of reduced DLC's have been selected as listed in Table 5.2. They are selected in order to include cases where tip-deflections and bending moments are largest, and cases with a large generation of fatigue damage. DLC 1.2 represents normal operation using the normal turbulence model (NTM). DLC 1.3 uses the extreme turbulence model (ETM). DLC 2.3 simulates an extreme operating gust (EOG) and is included to monitor the extreme tip deflections and loads. DLC 6.1 is a 50 year extreme wind model (EWM) with a parked turbine. DLC 6.1 depends strongly on control issues such as pitch settings, which can be defined arbitrarily

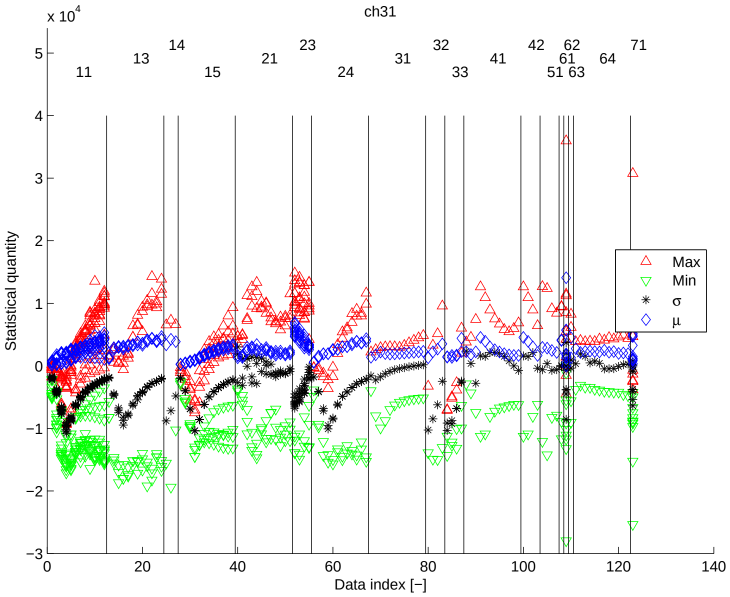

Figure 5.4: Statistical properties of the flapwise root bending moment [kNm] (positive for upwind bending), for the NREL5MW turbine. The numbers refer to IEC loadcases.

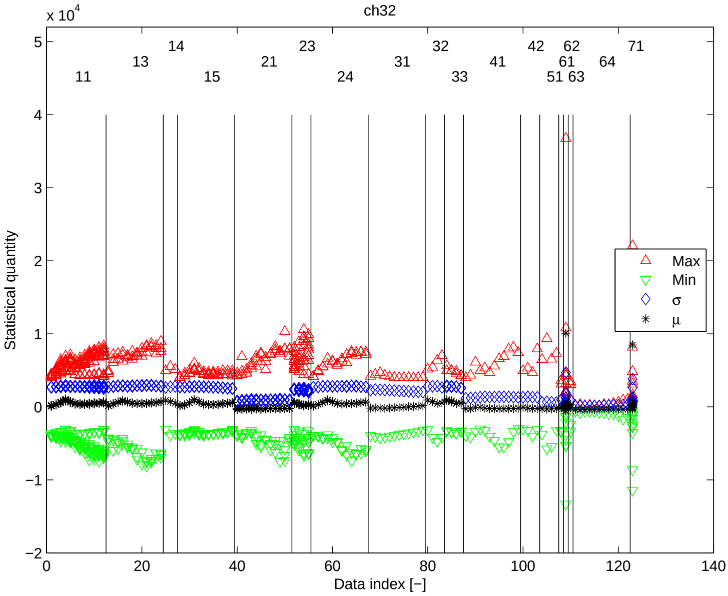

Figure 5.5: Statistical properties of the edgewise root bending moment [kNm] (positive for bending in the edgewise direction), for the NREL5MW turbine. The numbers refer to IEC loadcases.

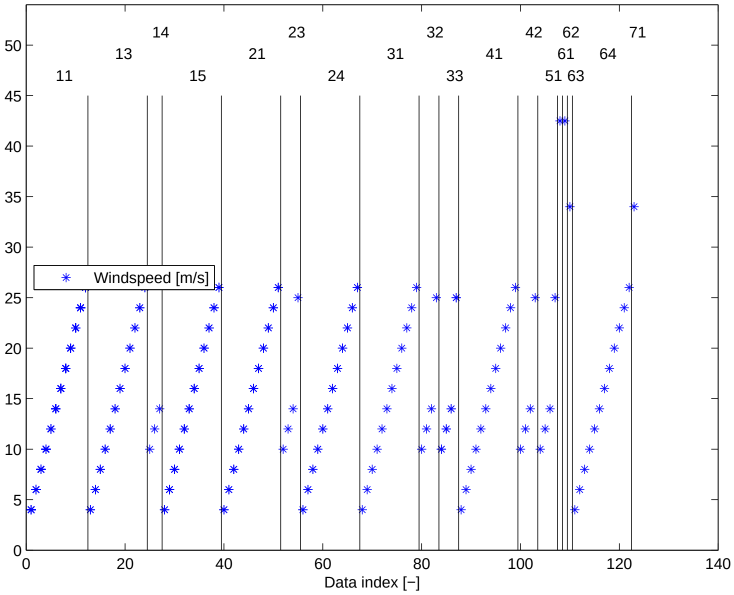

Figure 5.6: Average wind speeds in IEC design loadcases. The numbers refer to IEC loadcases.

in standstill. Therefore DLC 6.1 is actually less useful for conceptual design and can be omitted. Other DLC's involving normal shut down and emergency shut down have also been neglected as these are depending on the controller. It is relatively safe to assume that any possible problems due to the controller can be solved after the conceptual design process. At 11 m/s there is some fluctuations in e.g. power and therefore this wind speed has been avoided. Instead 10 m/s is used, which is just below rated power and max thrust. It is also close to the annual mean wind speed. The DLC's at 20 m/s are included in order to cover the more extreme turbulence at high wind speeds. The design point in the single point optimizations is rated wind speed and this should not be confused with wind speeds included in the reduced DLC's. They are selected in order to provide a clear picture of the fatigue sensitivity and should ideally include all wind speeds.

The DLC's are for wind turbine class IEC II B corresponding to medium reference windspeed and medium turbulence characteristics:

$$\text{Class IEC II B:} \quad V_{ref} = 42.5\,\text{m/s} \quad I_{ref} = 0.14$$

An atmospheric shear exponent of α=0.2 is used. The Weibull wind speed distribution is defined using a roughness length of z_0=0.01 m, parameters A=9.59 m/s,

V_0 [m/s]	f_W [-]	V_0 [m/s]	f_W [-]	V_0 [m/s]	f_W [-]
5.0	0.0827	12.0	0.0545	19.0	0.0082
6.0	0.0880	13.0	0.0450	20.0	0.0056
7.0	0.0892	14.0	0.0362	21.0	0.0038
8.0	0.0866	15.0	0.0283	22.0	0.0025
9.0	0.0810	16.0	0.0216	23.0	0.0016
10.0	0.0733	17.0	0.0160	24.0	0.0010
11.0	0.0642	18.0	0.0116	25.0	0.0006

Table 5.1: Discrete Weibull distribution of wind speeds. f_W is the discrete probability that the wind speed is V_0. The total probability that $5< V_0 <25=0.80$.

k=2.0 and hub height h_A=90 m. This corresponds to an average wind speed at hub height of 8.5 m/s. The cumulative probability function is

$$p_W(V_0) = 1 - \exp^{-(V_0/A)^k} \tag{5.1}$$

The discrete probabilities of the distribution are given in Table 5.1 and the values of f_j are defined so the sum at a given wind speed corresponds to the discrete probability. f_j describes the weighting of fatigue damage - an explanation is given in Section 5.3. For DLC 1.2 It is assumed that the turbine operates with yaw error 50% of the time. Note that the resulting weighted equivalent fatigue load corresponds to operation in windspeeds of 10 and 20 m/s, thus it only represents the fatigue damage generated in a fraction of the operating time. Even though the full operating range is not considered, the equivalent load will be a good representation of the overall fatigue sensitivity. An exact measure of the fatigue is found by including all windspeeds and the sum of f_j would be 1 corresponding to the full operation range of windspeeds.

5.3 Fatigue loads

The aeroelastic response of a given DLC results in a spectrum of load variations which is found using rainflow counting. This can be simplified to a single equivalent load $R_{eq,j}$ which generates the same fatigue damage per unit time as the spectrum if the load varies at the frequency f_{eq} (f_{eq}=1.0 is used throughout). The equivalent loads of multiple DLC's can be combined to an equivalent load R_{eq} by specifying the weight of the DLC as the fraction of lifetime the DLC represents. This is done using the factor f_j. R_{eq} can be related linearly to the equivalent stress S_{eq} which is measured in the actual material which absorbs the load variations. S_{eq} will in general depend on cross section properties.

Index	DLC	V_0	θ_{yaw}	TI	model	analysis	f_j
1,2	1.2	10	0	0.1834	NTM	F	0.01833
3,4	1.2	10	-10	0.1834	NTM	F	0.00916
5,6	1.2	10	10	0.1834	NTM	F	0.00916
7,8	1.2	20	0	0.1442	NTM	F	0.0014
9,10	1.2	20	-10	0.1442	NTM	F	0.0007
11,12	1.2	20	10	0.1442	NTM	F	0.0007
13,14,15	1.3	10	0	0.2946	ETM	U	0
16,17,18	1.3	20	0	0.1838	ETM	U	0
19	2.3	10	0	0.0	EOG	U	0
20	2.3	25	0	0.0	EOG	U	0
21	6.1	42.5	-8	0.0	EWM	U	0
22	6.1	42.5	8	0.0	EWM	U	0

Table 5.2: Reduced set of loadcases. U) Ultimate. F) Fatigue. Effective simulation time is 600 s unless otherwise stated - this is preceded by a 50 s run-in.

Further details are given in Appendix C and a short introduction is given in Appendix F.

5.4 Simplified design measure for flapwise fatigue - forced vibrations due to turbulence

A thorough description of fatigue issues for wind turbines can be found in [25]. The theory describes the fatigue on a turbine operating in the atmospheric boundary layer but does not present any indications about how it can effectively be reduced in the design process. An analytical study aimed at obtaining this knowledge have been made and results are presented in Appendix F. It is a description of the key parameters for the generation of fatigue damage due to variations in the flapwise bending moment. The analysis relates variations in inflow due to turbulence and shear to variations in bending moments and the equivalent fatigue load is derived. An important conclusion is that the equivalent fatigue load for the variations in flapwise bending moment can be approximated as:

$$R_{eq}^{m}(M_x) = \frac{1}{f_{eq}} 3.0\Omega(1-a)\left(\sigma_1 V_0 \Omega\, {}^1\!/\!_2\rho \int_r^R (r'-r) r' C_l' c\, dr'\right)^m \int_0^{8.0} \exp(-x) x^m\, dx \tag{5.2}$$

where C_l' is the slope of the dynamic lift curve and m is the Wöhler curve exponent (glass-fibre $m \approx 10$, steel $m=3$). The last integral represents the spectrum of the wind fluctuations. It is an advantage to design without taking the atmospheric properties into account. This yields

$$R_{eq} \propto (1-a)^{1/m}\Omega^{1+1/m} \int_r^R (r'-r)r'C_l'c\,dr' \tag{5.3}$$

Thus, for optimization it is only necessary to calculate relative changes from the reference design. Note that a will not change much if the turbine is designed for the same power. For simplicity it is also assumed that the dynamic lift slope is independent of design changes, and the exponent of the rotational speed is replaced with 1. This will introduce a small error but capture the basic trend. These changes result in:

$$R_{eq} \propto c_1 = \Omega \int_r^R (r'-r)r'c\,dr' \tag{5.4}$$

It is seen that the rotational speed and the distribution of the chord is important for R_{eq}. The stress is related to the load through Equation (C.8):

$$S_{eq} \propto \frac{y_{max}E_{y_{max}}}{EI_x}\Omega \int_r^R (r'-r)r'c\,dr' \tag{5.5}$$

The stress in the main spar is considered which is assumed to be in the distance y_{max}=$t_a/2$ from the neutral axis. The elastic modulus is E_α. This results in (omitting the factor 1/2):

$$S_{eq} \propto c_2 = \frac{t_a E_\alpha}{EI_x}\Omega \int_r^R (r'-r)r'c\,dr' \tag{5.6}$$

Note that EI_x is largely dictated by the constraint on maximum tip deflection and is therefore in practice constant. So the fatigue loads can be reduced by reducing the thickness and the elastic modulus. Unfortunately, doing so means that more material must be used, thereby increasing the weight.

The c_1 and c_2 coefficients can now be used to approximate the relative fatigue sensitivity of different blades.

The dynamic lift curve slope was omitted in the definition of c_1 and c_2, but it is very important because it affects the change in aerodynamic forces for a given change in angle of attack. However, c_1 and c_2 are relative measures of the sensitivity and reducing them will in general reduce fatigue damage.

5.5 Parameter study - changing design lift coefficient

Before starting the fully numerical optimization a small parameter study using HAWC2 was carried out. This highlights important properties and verify that the reduced DLC's have been selected properly. It will also validate the use of Equation (5.4).

The chord is changed manually. The HAWC2-control will then automatically change pitch and C_l in order to keep $c^* C_l N_B$ constant and thereby maintaining the same power output. The new chord and lift coefficient then becomes

$$c_{new} = c f_c \tag{5.7}$$

$$C_{l,new} = C_l / f_c \tag{5.8}$$

The quasi-steady aerodynamic loads at design conditions are not changed, but they may change at off-design conditions which will influence AEP. The fatigue loads are expected to change significantly. The changed chord will influence the structural properties of the blade and to avoid major changes in the flapwise bending stiffness and blade mass, the relative thickness is changed in order to maintain the absolute thickness

$$t_{new} = t / f_c \tag{5.9}$$

The pitch angle will change with C_l and the lift to drag ratio will also change, possibly leading to higher drag. The range $C_{l,max}$-C_l also changes and this may affect the stall characteristics and the power.

Figure 5.7 shows the equivalent loads for the flapwise root bending moment for the reduced DLC's. Figure 5.8 shows the equivalent loads for the edgewise root bending moment. Figure 5.9 shows the maximum tip deflections.

The results confirms that the equivalent load scales linearly with the chord as predicted by equation 5.2 which is shown as the solid line in Figure 5.7. This is true even at 20 m/s where a large part of the blade is in stall, but the dynamic lift slope is almost the same making scaling possible. Note that a reduction in equivalent load to 90% leads to a fatigue damage of $(0.9)^m$. For m=10 the damage is reduced to 35%. The AEP is lower for the reduced chord and this is associated with the loss in efficiency above design tip speed ratio and increased drag. The drag may be reduced significantly by tailoring the airfoils to the specific design requirements (i.e. minimizing drag at the design lift coefficient). The increase in relative thickness also increases drag because the best lift to drag ratio is found for thin profiles. The thicker blade will also be more sensitive to

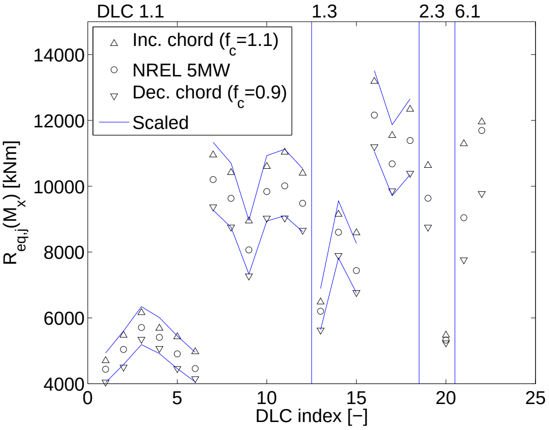

Figure 5.7: Equivalent root flapwise moment for reduced DLC's (m=10).

	M [kg]	AEP [GWh]	f_1 [Hz]	f_2 [Hz]	f_3 [Hz]
Increased chord (f_c=1.1)	16900	19.72	0.647	1.10	1.91
NREL 5MW	15100	19.51	0.665	1.05	1.94
Decreased chord (f_c=0.9)	13340	19.23	0.683	0.98	1.99

Table 5.3: Key results from parameter study

leading edge roughness and may have worse dynamic stall characteristics. Table 5.3 summarizes key results in the parameter study.

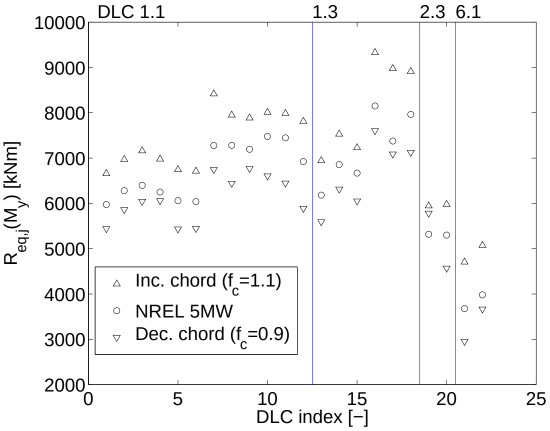

Figure 5.8: Equivalent root edgewise moment for reduced DLC's (m=10).

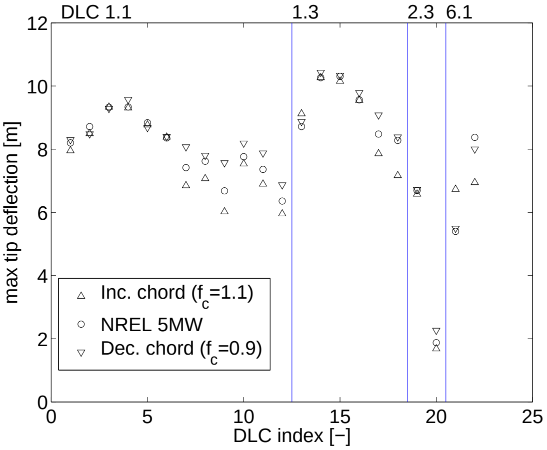

Figure 5.9: Max tip deflection for reduced DLC's.

5.6 Conclusions

A design methodology has been suggested, which is aimed at making a stable and effective optimization process for PRVS turbines. It is based on knowledge about the key parameters for aerodynamics and structures, which have been discussed in previous chapters. Among other things, the design lift coefficient is important and is determined using single point optimization.

Based on a full IEC set of loadcases a reduced set of design load cases (DLC's) have been defined which can be used for quick evaluation of the design objective. The DLC's have been defined in order to include operating conditions which are important for the dynamic flapwise loads.

The fatigue analysis of several timeseries have been introduced. The analysis describes the equivalent fatigue load, which will be used to combine the results of several aeroelastic calculations into a single measure.

Sensitivity parameters c_1 and c_2 for the flapwise fatigue loads have been defined. They depend on chord distribution and rotational speed, and can be used for fast initial optimizations without aeroelastic simulations. A parameter study has verified that fatigue loads scales proportional to the sensitivity parameters, as predicted by the theory.

Chapter 6

Results

This chapter contains the results of an optimization. It follows the steps described in Section 5.1 but the results of the tuning of the structural model have also been included. The objective is to design for low fatigue loads due to variations in the flapwise bending moment M_x, i.e. $R_{eq}(M_x)$ is reduced. The results are compared and discussed in the end of the chapter.

In the following, *NREL 5MW* refers to the reference turbine.
NREL 5MW (H) refers to the reference turbine with the structural data defined using our model for the blade - the aerodynamic shape is exactly the same. *HAWTOPT* refers to calculations or optimizations from HAWTOPT, which in all cases uses our structural model.

6.1 Reference turbine, NREL 5MW

The 3 bladed NREL 5MW [18] fictitious turbine was used as reference case. Some key parameters are listed in Table 6.1. M is the total mass of a single blade.

AEP			21.3425 GWh
M			16880 kg
C_P	11 m/s	λ=6.37	0.459
$C_{P,l}$	11 m/s	λ=6.37	0.492
C_T	11 m/s	λ=6.37	0.719
v^*_{tip}	11 m/s	λ=6.37	0.095 (6.0 m)

Table 6.1: Key parameters for NREL 5MW

	α	β	γ	δ
ρ [kg/m^3]	1900.0	1900.0	1900.0	1900.0
E_{11} [Pa]	37.0e9	15.0e9	30.0e9	15.0e9
G_{12} [Pa]	2.3e9	2.3e9	2.3e9	0.0
β,γ,δ		0.003	0.003	0.003

Table 6.2: Input to the structural model.

6.2 Reference turbine - structural model

The optimizations have been carried out using the structural model defined earlier. The properties of the reference blade are deliberately reproduced as a part of the tuning of structural parameters. Figure 6.1 (a,b,c,d) shows the distribution of mass and stiffness. The results deviatev substantially on the innermost part where a steel flange etc. is mounted. The mass difference is approximately 500 kg (per blade) and therefore a constant value of 1500 kg is added to the nacelle mass. The first 3 blade-eigenfrequencies are reported in Table 6.3 and the differences are within 1%. Thus, the structural model yields results which are close to the reference values and it is concluded that realistic eigenfrequencies are obtained and that the simplifying assumptions in the structural model are valid. Figure 6.1 (e,f) shows the relative and absolute shell thicknesses.

The quantities in Table 6.2 was used in the structural model. The α-value, which is the shell thickness of the main spar normalized with the chord, was restricted to the range: [0.003, 0.010]. The absolute thickness of the main spar was limited to h_α=0.03 m. These parameters have been selected in order to represent the materials and shell thicknesses used in the reference turbine.

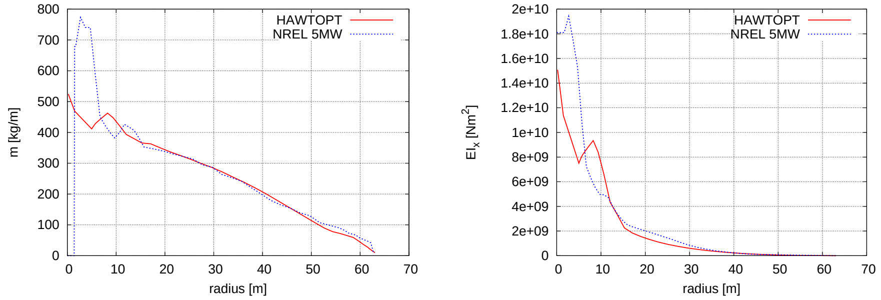

(a) Mass (b) Flapwise stiffness

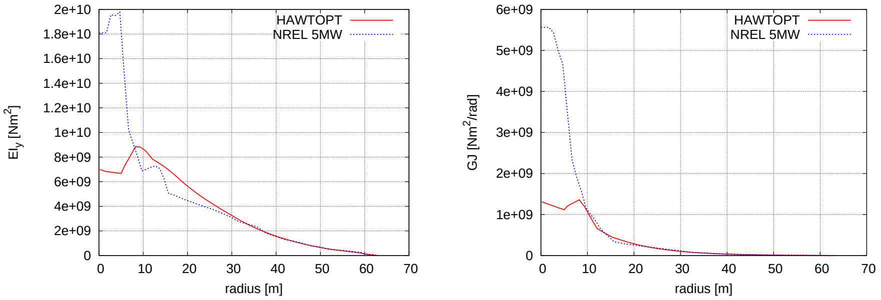

(c) Edgewise stiffness (d) Torsion stiffness

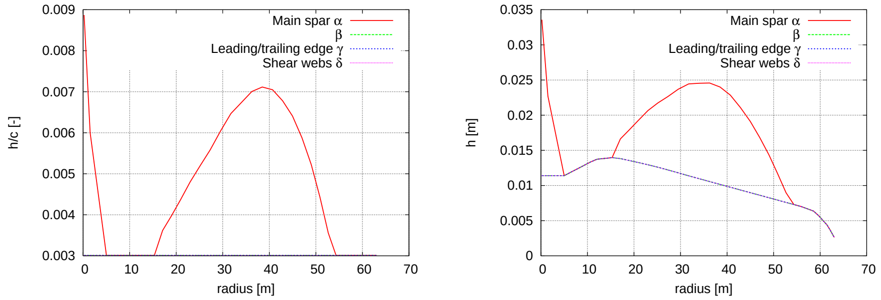

(e) Relative shell thickness. $\beta=\gamma=\delta=0.003$. (f) Absolute shell thickness

Figure 6.1: Plots of parameters for the reference turbine. The structural data is obtained using our structural model, which has been tuned to reproduce the reference values.

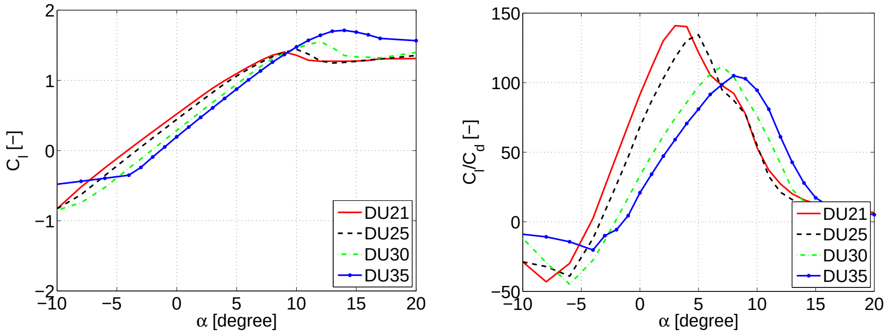

(a) Lift data (b) Lift to drag ratio

Figure 6.2: Original profile data for the NREL 5MW turbine (TU Delft, DUxx profiles).

6.3 Initial point optimization

This section describes the results of a point optimization at 11 m/s. The objective is the equivalent fatigue load of the flapwise bending moment $R_{eq,1(100s)}(M_x)$ evaluated using 100 second simulations of DLC 1 in Table 5.2. The optimization is constrained by the inviscous power coefficient $C_{P,l}$ which makes the optimization independent of the drag properties of the airfoils. Figure 6.2 shows the 2D aerodynamic data used.

Figure 6.3 shows distributions of key parameters from the optimized design. The stiffness and mass distributions are largely unchanged. The major difference in the design is the decrease in chord, and the main spar thickness is increased in order to account for the decrease in absolute structural thickness. The relative thickness has a minimum around r=48 and increases near the tip. The absolute thickness follows a smooth curve and the blade is in general thinner than the reference. The lift coefficient at rated power is around $C_l \approx$1.4 on most of the blade. This is close to max lift, indicating that high lift airfoils should be used. The $^l/_d$ ratio is around 75 and this reduces the total power considerably. The inviscous power is the same as for the reference turbine, and therefore a new set of 2D airfoil data should be used which performs well at high C_l values. This is described in the next section.

Figure 6.4 shows the equivalent fatigue loads corresponding to Table 5.2. These are in general reduced indicating that the optimization based on a single 100 second load case has yielded a general reduction.

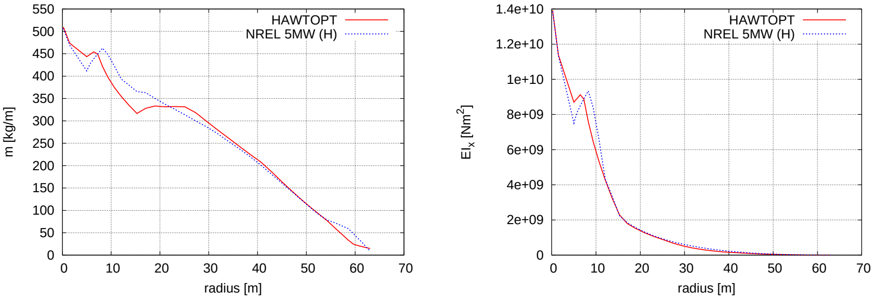

(a) Mass (b) Flapwise stiffness

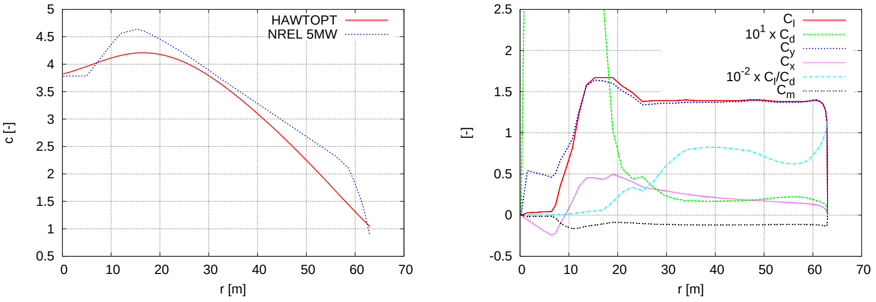

(c) Chord (d) Aerodynamic coefficients

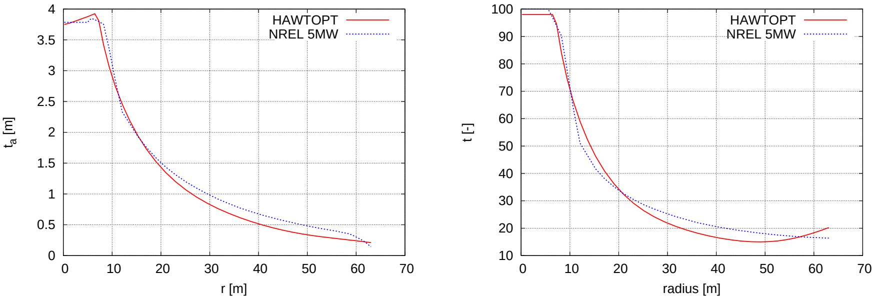

(e) Absolute thickness (f) Relative thickness

Figure 6.3: Results of the initial point optimization using DUxx profiles are compared to reference values.

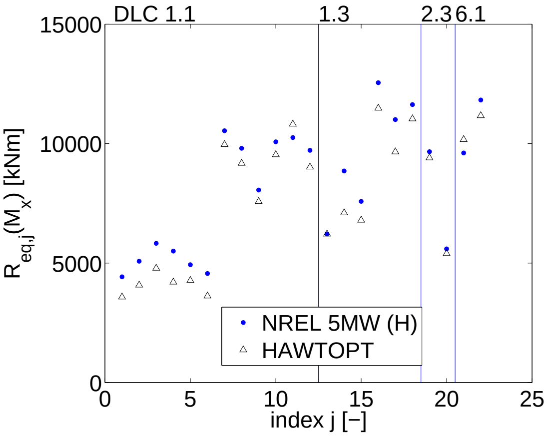

Figure 6.4: Equivalent fatigue loads for flapwise bending moment for the reduced DLC's calculated for the point optimized design based on DU-xx profiles.

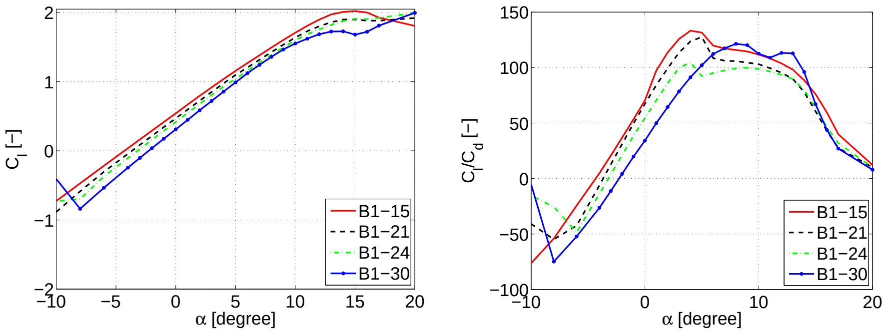

(a) Lift data (b) Lift to drag ratio

Figure 6.5: Profile data for the selected high lift airfoils (Risø B1-xx profiles).

6.4 Point optimization using high-lift airfoils

In section 6.3 it is found that high lift airfoils should be used on this design and the Risø B1-xx airfoil family have been selected. The lift and drag characteristics are seen in Figure 6.5. These profiles have a number of advantages. 1) They are designed to be roughness insensitive. 2) They have high $^{l}/_{d}$ at the high C_l values which was not the case for the DUxx profiles. 3) The max-lift is high and it is possible to design very slender blades with low fatigue sensitivity and possibly take advantage of high stiffness materials (E.g. carbon fibres).

The point optimization is continued, but now the total C_P is used as the constraint on power. It was also found necessary to limit the relative thickness to t=21% on the outer part of the blade. Figure 6.6 shows distributed properties for the new design. The result is a very slender blade which is designed around a high $C_l \approx 1.7$. There is an error in the drag data which is negative and therefore not realistic around r=19 m. It is believed that this is due to errors in the 3D corrections, but that it will only have a minor influence on the overall results.

Figure 6.7 shows the equivalent fatigue loads for the reduced DLC's. There is a clear reduction at all DLC's.

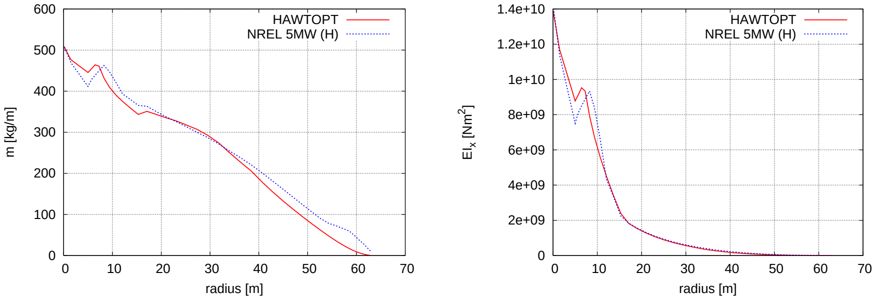

(a) Mass (b) Flapwise stiffness

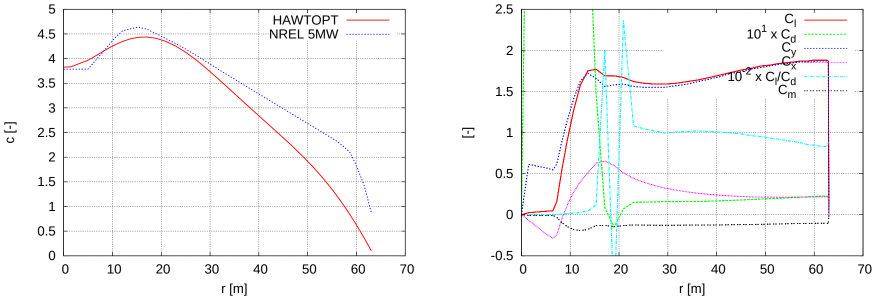

(c) Chord (d) Aerodynamic coefficients. There is an error in the drag data at r=19 m

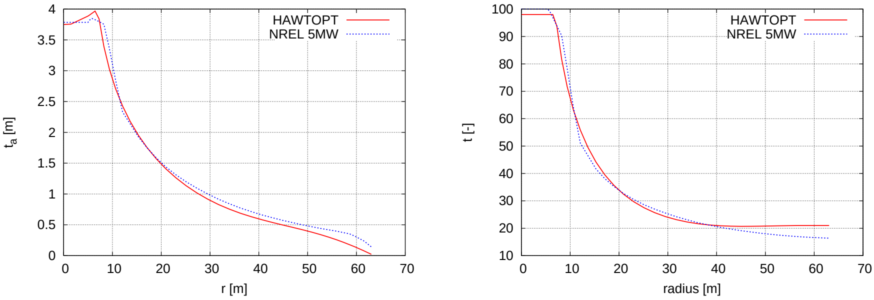

(e) Absolute thickness (f) Relative thickness

Figure 6.6: Plots of parameters for the NREL 5MW reference layout and the initial optimization values using B1-xx high lift profiles.

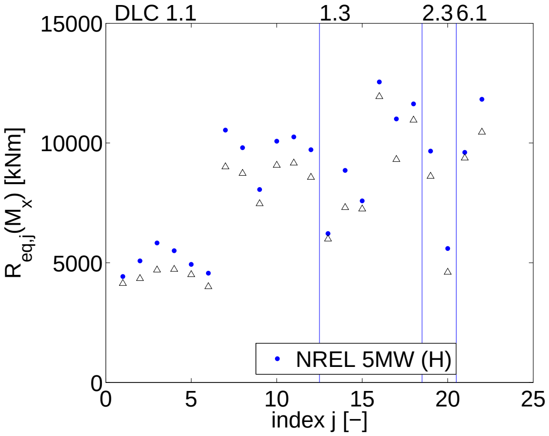

Figure 6.7: Equivalent fatigue loads for flapwise bending moment for the reduced DLC's calculated for the point optimized design based on B1-xx profiles. Note that triangles represent the optimized turbine.

6.5 Power curve optimization using high-lift airfoils

The title of this section is misleading because AEP is not optimized but instead constrained to the value of the reference turbine. In practice the blade is optimized for AEP until the value is above the reference, i.e. the blade is in the design space. The optimization is then switched to the primary objective and the constraint on AEP is applied.

The final optimized blade has an AEP which is lower than the reference turbine. It is noted that there often is a trade-off between AEP and fatigue loads, i.e. reducing fatigue loads is associated with a reduction in AEP. A general explanation for this is not known by the author, it is simply a numerical result. A possible explanation is that the B1-xx profiles have higher drag, which is the case for the 21% percent profile which for B1-xx has a $^{l}/_{d}$ ≈110 versus $^{l}/_{d}$ ≈135 for the DUxx profile. The 21% percent profiles are used on a part of the blade which is heavily loaded and $^{l}/_{d}$ is therefore very important. It is questionable whether the good performance of the DUxx profiles can be obtained in practice when leading edge roughness is present, and instead the lower AEP resulting from the use of B1-xx profiles has been accepted. The constraint on AEP was set to minimum 21.1 GWh in the final aeroelastic optimization for low fatigue loads.

Figure 6.8 shows distributed properties of the final design. The aerodynamic coefficients are plotted for both 8 and 11 m/s which corresponds to the highest and lowest λ, below rated power. This shows the relevant upper and lower limits on C_l, between which the airfoils should have low drag. Above rated power this is not important.

Figure 6.9 shows $R_{eq,j}(M_x)$ for the reduced DLC's. $R_{eq,j}(M_x)$ is reduced in all DLC's.

The aerodynamic shape of the final blade is tabulated below.

```
Radius     Chord     Twist     Thick     Abs. Thick
(m)        (m)       (deg.)    (-)       (m)
---------------------------------------------------
 0.00e+00  3.79e+00  1.36e+01  9.88e+01  3.75e+00
 1.50e+00  3.80e+00  1.32e+01  9.88e+01  3.75e+00
 5.00e+00  3.94e+00  1.24e+01  9.88e+01  3.89e+00
 5.31e+00  3.95e+00  1.23e+01  9.88e+01  3.91e+00
 5.80e+00  3.98e+00  1.22e+01  9.88e+01  3.94e+00
 6.45e+00  4.03e+00  1.20e+01  9.88e+01  3.98e+00
 7.27e+00  4.09e+00  1.18e+01  9.33e+01  3.81e+00
 8.24e+00  4.16e+00  1.16e+01  7.81e+01  3.25e+00
 9.38e+00  4.24e+00  1.13e+01  6.59e+01  2.79e+00
 1.07e+01  4.33e+00  1.09e+01  5.58e+01  2.41e+00
 1.21e+01  4.42e+00  1.05e+01  4.76e+01  2.10e+00
 1.36e+01  4.50e+00  1.01e+01  4.09e+01  1.84e+00
 1.53e+01  4.56e+00  9.59e+00  3.55e+01  1.62e+00
 1.71e+01  4.60e+00  9.07e+00  3.13e+01  1.44e+00
 1.90e+01  4.60e+00  8.51e+00  2.82e+01  1.30e+00
 2.09e+01  4.56e+00  7.92e+00  2.58e+01  1.18e+00
 2.30e+01  4.46e+00  7.30e+00  2.42e+01  1.08e+00
 2.51e+01  4.32e+00  6.65e+00  2.31e+01  1.00e+00
 2.73e+01  4.14e+00  6.00e+00  2.25e+01  9.30e-01
 2.95e+01  3.92e+00  5.33e+00  2.20e+01  8.64e-01
 3.17e+01  3.68e+00  4.66e+00  2.18e+01  8.01e-01
 3.40e+01  3.43e+00  3.99e+00  2.16e+01  7.40e-01
 3.62e+01  3.18e+00  3.34e+00  2.14e+01  6.80e-01
 3.85e+01  2.94e+00  2.71e+00  2.12e+01  6.23e-01
 4.07e+01  2.72e+00  2.11e+00  2.09e+01  5.70e-01
 4.29e+01  2.52e+00  1.55e+00  2.06e+01  5.21e-01
 4.50e+01  2.34e+00  1.02e+00  2.03e+01  4.77e-01
 4.70e+01  2.18e+00  5.33e-01  2.00e+01  4.36e-01
 4.90e+01  2.03e+00  9.36e-02  1.97e+01  3.99e-01
 5.09e+01  1.88e+00 -2.99e-01  1.94e+01  3.64e-01
 5.27e+01  1.72e+00 -6.45e-01  1.91e+01  3.29e-01
 5.43e+01  1.56e+00 -9.46e-01  1.89e+01  2.94e-01
 5.59e+01  1.38e+00 -1.20e+00  1.86e+01  2.58e-01
 5.73e+01  1.20e+00 -1.42e+00  1.84e+01  2.21e-01
 5.86e+01  1.01e+00 -1.60e+00  1.82e+01  1.83e-01
 5.97e+01  8.18e-01 -1.75e+00  1.79e+01  1.47e-01
 6.07e+01  6.34e-01 -1.87e+00  1.77e+01  1.12e-01
 6.15e+01  4.66e-01 -1.96e+00  1.75e+01  8.16e-02
 6.21e+01  3.21e-01 -2.03e+00  1.73e+01  5.56e-02
 6.26e+01  2.08e-01 -2.08e+00  1.72e+01  3.57e-02
 6.29e+01  1.34e-01 -2.11e+00  1.71e+01  2.28e-02
 6.30e+01  1.00e-01 -2.12e+00  1.70e+01  1.70e-02
```

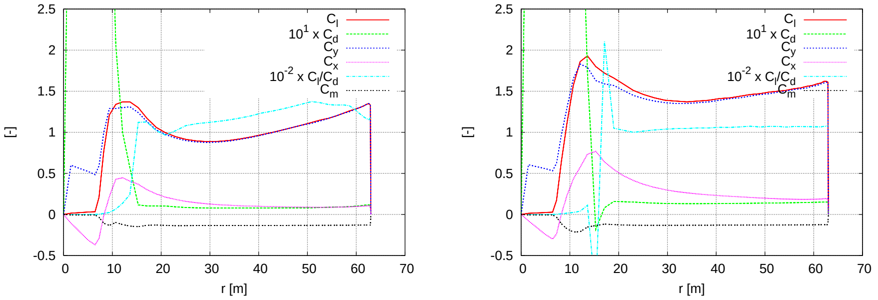

(a) Aerodynamic coefficients at V_0=8 m/s. (b) Aerodynamic coefficients at V_0=11 m/s.

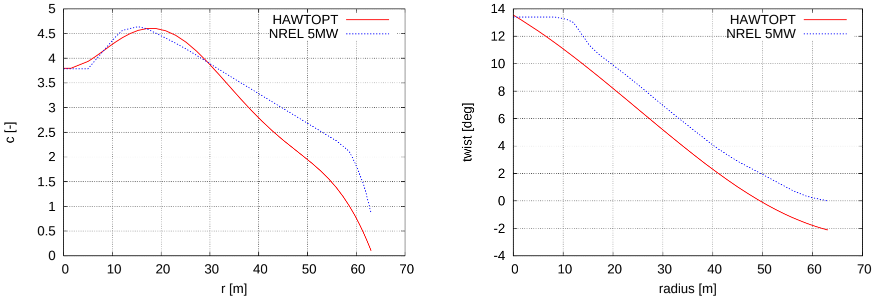

(c) Chord (d) Twist, β

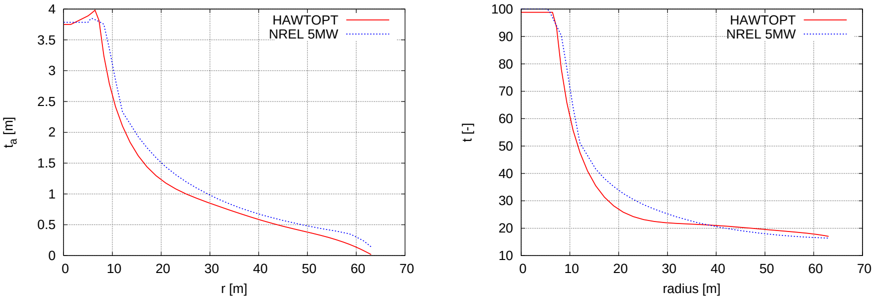

(e) Absolute thickness (f) Relative thickness

Figure 6.8: Plots of parameters for the NREL 5MW reference layout and the final power curve optimization.

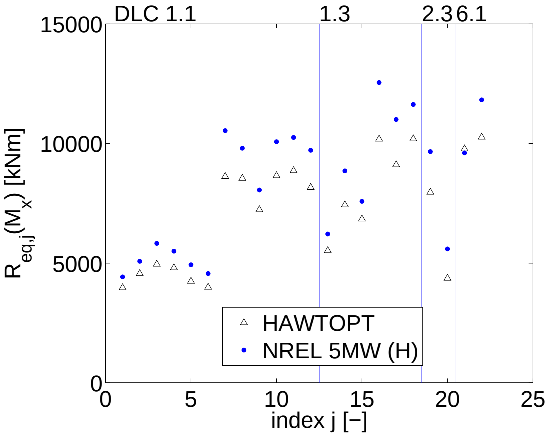

Figure 6.9: Equivalent fatigue loads for flapwise bending moment for the reduced DLC's calculated for the AEP optimized design based on B1-xx profiles

6.6 Comparison of designs

An overview of key properties for the reference and designed blades are given below.

Table 6.3 compares the mass and eigenfrequencies. Note that the high lift blade has relatively high eigenfrequencies, these are reduced slightly in the final design. The differences in blade mass is small and the final blade is 4% lighter than the reference (NREL 5MW (H)).

Table 6.4 compares energy production and design point. The two blades which are optimized in a single design point have an annual energy production which is 1.5% lower than the reference blade. The AEP is lost at the off design conditions below rated power, which in our case is the low windspeeds. The loss of AEP is not acceptable but it is still close to the reference value. Thus, a reasonable design can be obtained from a single design point. The final AEP optimized design has an AEP which is 1.0% lower than the reference design. This was discussed in Section 6.5.

Table 6.5 shows the fatigue sensitivity parameters, c_1 and c_2 in the root (r=0) they are smallest for blade 6.4 which is slender and designed using high lift airfoils. The maximum value of c_2 follows the same trend - note that this maximum value is usually found around $r^* \approx {}^1\!/_3$.

Table 6.6 shows the numerically determined equivalent fatigue loads. $R_{eq,1(100s)}(M_x)$ denotes the 100 second aeroelastic calculation based on DLC 1. $R_{eq}(M_x)$ refers to the weighted equivalent load of the reduced DLC's. $R_{eq}(M_x)$ follows the same trend as in Table 6.5 where the high lift blade shows the lowest analytical fatigue sensitivity. However, $R_{eq,1(100s)}(M_x)$ does not follow this trend and this shows that a single, short, aeroelastic calculation does not necessarily provide a correct picture of the overall fatigue sensitivity. However, the result of the optimizations, which was made using $R_{eq,1(100s)}(M_x)$, was still a reduction in R_{eq}. It is also noted that the final design has an even lower $R_{eq}(M_x)$ than the single point optimized blade using B1-xx profiles. Probably this is because the optimizer had not converged completely in the single point optimization. On the final blade a 15% reduction in $R_{eq}(M_x)$ was obtained, relative to the reference design. The equivalent edgewise fatigue load $R_{eq}(M_y)$ was reduced with 8.5%.

		M [kg]	f_1 [Hz]	f_2 [Hz]	f_3 [Hz]
6.1	NREL 5MW	16880	0.672	1.05	1.95
6.2	NREL 5MW (H)	16330	0.665	1.06	1.94
6.3	Point Opti. (DUxx)	15945	0.658	1.03	1.89
6.4	Point Opti. (B1-xx)	15500	0.798	1.19	2.25
6.5	AEP Opti. (B1-xx)	15700	0.720	1.17	2.03

Table 6.3: Structural key parameters for blades

		AEP [GWh]	Airfoils	λ	C_l
6.1	NREL 5MW	21.3425	DUxx	7.7	0.95
6.3	Point Opti. (DUxx)	21.0414	DUxx	6.4	$\approx$1.4
6.4	Point Opti. (B1-xx)	20.9682	B1-xx	6.4	$\approx$1.6-1.8
6.5	AEP Opti. (B1-xx)	21.1034	B1-xx	6.4-8.6	$\approx$1.4-1.6

Table 6.4: Aerodynamic key parameters for blades. λ and C_l refers to the design point, which for 6.3 and 6.4 are at rated wind speed. For 6.5 this refers to the wind speeds below rated power ($5< V_0 <11$ m/s), which are important for AEP.

		$c_1(r=0)$	$c_2(r=0)$	$\max(c_2)$
6.1	NREL 5MW	2.545e+05	2.572e+06	5.043e+06
6.2	NREL 5MW (H)	2.545e+05	2.572e+06	5.043e+06
6.3	Point Opti. (DUxx)	2.200e+05	2.190e+06	4.350e+06
6.4	Point Opti. (B1-xx)	1.870e+05	1.861e+06	3.498e+06
6.5	AEP Opti. (B1-xx)	1.935e+05	1.955e+06	3.730e+06

Table 6.5: Simplified fatigue parameters for blades.

		$R_{eq,1(100s)}(M_x)$	$R_{eq}(M_x)$	$R_{eq}(M_y)$
6.1	NREL 5MW	-	-	-
6.2	NREL 5MW (H)	4202.0	5983.0	5270.9
6.3	Point Opti. (DUxx)	3142.0	5787.5	5376.2
6.4	Point Opti. (B1-xx)	3466.0	5258.1	4966.1
6.5	AEP Opti. (B1-xx)	3492.0	5074.4	4826.9

Table 6.6: Fatigue parameters according to reduced DLC's.

6.7 Conclusions

The single point optimizations at rated wind speed has yielded sound designs, but with an undesirable reduction in AEP of approximately 1.5% relative to the reference turbine. The power curve optimization was carried out by constraining AEP to 21.1 GWh. This is 1.0% below AEP for the reference turbine, but this has been accepted in this work because the loss can be regained by increasing the radius[1], which will be associated with a small increase in fatigue loads. The final design is close to the result of the point optimizations, which was expected in the discussion of the design methodology in Chapter 5.

The 100 s DLC used for aeroelastic evaluation of fatigue loads gave a misleading indication of the fatigue-sensitivity in the case of B1-xx high lift airfoils compared to the DUxx medium lift airfoils. However, the aeroelastic results of the reduced set of DLC's showed that a good design was obtained anyway. The analytical fatigue parameter c_1 was used for initial optimization and this yielded designs close to optimum with respect to low fatigue loads. Thus, an initial optimization can be made fast by minimizing c_1.

The c_2 fatigue parameter was found to decrease in all cases. However, in general it is important to constrain it. It is worth to mention that the reductions in fatigue loads are larger than those indicated by R_{eq} because S_{eq} are reduced further due to the thinner blade leading to smaller material strains for the same load.

The design strains, which are evaluated according to the quasi-steady design loads, are small, and for the final design the extreme values was ϵ_z=0.0025 and ϵ_z=-0.0023. Unsteady loads will increase this, but it is assumed this will be limited to between 50-100%. This is well below the ultimate strain for most materials and therefore has ultimate failure not been considered. Note that this may not be the case for very large turbines (10-20 MW) which experience very large gravity loads.

---

[1] From the definition of C_P it follows that the radius should be increased by a factor $\sqrt{1.01}$=1.005 in order to increase the power by 1.0%.

CHAPTER 7

Conclusion

The present project is about wind turbine rotor optimization which is multidisciplinary. As a minimum it involves aerodynamic, structural and numerical issues, making it a very complex task. Tools have been improved and developed and is has been demonstrated that a design with reduced fatigue loads can be obtained. In this thesis focus is on the experience gained regarding optimization of PRVS turbines and the description of key parameters. This includes the developed conceptual models for the structural layout which are based on as few parameters as possible. More complicated issues, such as $\mathrm{BEM}_{\mathrm{cor}}$ and the aeroelastic simulation tools, have been referred to.

Three articles are included in this thesis. The first describes $\mathrm{BEM}_{\mathrm{cor}}$, which is a corrected blade element momentum method with an accuracy comparable to the actuator disc method but at the same time much faster. This method has been used in all numerical calculations. The second article describes aerodynamic optimization using $\mathrm{BEM}_{\mathrm{cor}}$ compared to the traditional BEM method. This shows that there are differences in the design optima especially regarding the blade twist and it is possible to obtain a lower blade root bending moment. Besides from this $\mathrm{BEM}_{\mathrm{cor}}$ gives more accurate predictions of AEP and it is therefore a useful tool in rotor optimization. The third article describes fatigue loads on a 5MW wind turbine due to atmospheric turbulence. The analysis is carried out numerically and analytically and has resulted in an expression for the equivalent fatigue load. Based on this, two fatigue sensitivity parameters have been defined which depend on the key parameters for the blade design. The sensitivity parameters where used with success in the numerical design process where they replaced aeroelastic calculations in the initial optimization iterations.

Aerodynamic design has been studied extensively. Besides from numerical optimizations using BEM_{cor}, analytical design methods have also been used. In this thesis a method has been presented which is based on a prescribed constant thrust, which is equivalent to a constant axial induction. The effects of tip losses and wake swirl losses are included. The resulting set of simple equations describes the power, thrust and root flap moment coefficients as function of tip speed ratio, thrust and the airfoil lift to drag radio, which are key parameters. The lift to drag ratio only affects the power coefficient and an inviscous power coefficient is defined, which is useful for optimizations where focus is on structural and aeroelastic properties. Another important result is that a given design can be expressed using a design parameter $(c^* C_l N_B)$. This means that there is freedom in selecting the lift coefficient C_l and the resulting value of the normalized chord c^* will depend on it. Therefore, C_l is a key parameter and the choice of it will affect both the drag characteristics and the structural properties, which depend on the chord. The conclusions have been used in the set up for aeroelastic optimizations.

It has been described how a conceptual structural model can be made, and it has been used to define input to the aeroelastic simulations. The cross section properties are found using dimensionless coefficients, which are based on the knowledge of airfoil shapes with various relative thicknesses. The basic input is the defined tip deflection at rated wind speed where the quasi steady loads are largest. The blade structure is then laid out by varying the distributed thickness of the main load carrying spars according to a prescribed deflection shape. This method resulted in stable numerical optimizations and a realistic design.

BEM_{cor} was implemented for improved quasi steady aerodynamic calculations. Besides from the issues mentioned earlier, it is noted that it was almost as stable as the traditional BEM method, but a little slower. However, it is still a fast method and very useful for heavy optimizations. The stability problems were limited to very few cases where the problems probably could have been solved by changing damping parameters in the iterative scheme. Another solution was to use BEM for initialization of the design before using BEM_{cor}.

Aeroelastic optimizations are challenging for a number of practical issues: 1) The design space is very large and the global optimum is not easily found. 2) numerical instabilities causes the time consuming calculations to fail or the optimizations to diverge. Other practical problems may also arise and therefore the general optimization procedure used in this project, which is relatively stable, have been described. It is based on initial optimizations in a single design point, which for PRVS turbines is the rated wind speed. An important part of the procedure is the determination of a reasonable range of the design lift coefficient, which is a key component influencing the chord length and therefore both the fatigue sensitivity to turbulence as well as the structural properties. A major problem with the approach is that the AEP may be lower than for a reference turbine, even after subsequent power curve optimizations. It is not clear whether this is caused by the single point optimization procedure or because airfoils different from the reference turbine have been used. However, the final result is still a good design.

In the optimizations the aeroelastic code HAWC2 has been used for evaluation of fatigue loads and these were calculated from a single 100 second simulation. A simulation of 100 seconds is not representative for the many operation conditions of a wind turbine, but the optimizations yielded blades which in general had an improved performance with respect to the optimization objective. For time savings the optimizations were initialized using the analytical fatigue sensitivity parameter which was minimized. This yielded a good initial design, and this reduced the number of necessary aeroelastic calculations in the subsequent optimizations.

A blade has been optimized for reduced fatigue loads - the reference turbine was the NREL 5MW fictitious turbine. This has resulted in a blade which is designed around a high lift coefficient and a small chord, i.e. a very slender blade. The flapwise fatigue loads were reduced by 15% and the AEP was reduced by 1% relative to a reference turbine. It is therefore indicated that high lift profiles are superior to medium or low lift when designing for low fatigue damage.

The developed numerical tools are now implemented in the turbine optimization code HAWTOPT. The inclusion of the structural model means that more freedom can be used in the design process, and the effects of new concepts on the turbine design and its aeroelastic properties can be determined quickly.

Not all the work carried out in the PhD project has been described in this thesis. This includes data analysis of wind tunnel measurements using high frequency microphones distributed chordwise over the surface of airfoils. This has resulted in knowledge about the laminar to turbulent transition in the boundary layer, which is important for the airfoil properties and the roughness sensitivity, which affects the drag. It has earlier been described that accurate profile data are very important in numerical optimization and such experimental work is therefore important.

7.1 Future work

The tools developed in this project will be used in the future work at Risø DTU. A specific project is Light Rotor which aims at developing a 10 MW rotor. This will include the design of a new airfoil family and the experience gained in this project will be used.

One apparent problem with the structural model is that the mass decreases with chord length. It is well known that the opposite is usually the case and one reason for this is that the shell thickness near the leading and trailing edge has been defined as a fixed fraction of the chord. If the chord and the absolute profiles thickness are decreased more material must be put into the main spar to obtain the required stiffness but this mass increase is canceled by the savings in the other structural sections. Because of this a better model should be developed which considers the buckling loads in the β sectors and the edgewise stiffness requirements and define the γ sector accordingly. Note that it is possible to cope with the buckling requirements by varying the core thickness in a sandwich constructions in the β sector, and maintaining the absolute shell thickness of the surface material (i.e. a fixed value of h_β). This will only make minor changes to E_{11} and ρ but may change G_{12}, thus it should be ensured that torsion is not important. In any case it is necessary to make a thorough analysis of the structural integrity and make adjustments in the engineering input to the structural module.

The blade angular deformation due to torsion should be included in the blade layout module. The module should also be able to handle a user specified undeformed shape. This may include sweep, prebend etc.

Bibliography

[1] Bak C. Aerodynamic design of wind turbine rotors. *Wind energy systems: Optimising design and construction for safe and reliable operation.*, JD S, JN S (eds.). Woodhead Publishing Limited, 2010.

[2] Hansen MOL. *Aerodynamics of Wind Turbines*. second edn., Earthscan, 2008.

[3] Burton T, Sharpe D, Jenkins N, Bossanyi E. *Wind Energy Handbook*. John Wiley & Sons, 2001.

[4] Fuglsang P. Aerodynamic Design Guidelines for Wind Turbine Rotors. *A Collection of the 1998 ASME Wind Energy Symposium Technical Papers at the 36th AIAA Aerospace Sciences Meeting and Exhibit* 2002; .

[5] Johansen J, Madsen HA, Gaunaa M, Bak C, Sørensen NN. 3D Navier-Stokes Simulations of a Rotor Designed for Maximum Aerodynamic Efficiency. *Proceedings of the 42nd AIAA Aerospace Sciences Meeting and Exhibit*, ASME Wind Energy Symposium, American Institute of Aeronautics and Astronautics, 2007.

[6] Snel H. Review of Aerodynamics for Wind Turbines. *Wind Energy* 2003; **6**:203–211.

[7] Bak C. key parameters in aerodynamic rotor design. *Research in Aeroelasticity EFP-2006* 2007; .

[8] Døssing M. Vortex lattice modelling of winglets on wind turbine blades. *Risø-R-1621(EN). (M. Sc. thesis)*, Risø DTU, Wind Energy Department 2007.

[9] Gaunaa M, Sørensen NN, Døssing M. Prediction of steady aerodynamic performance of rotors with winglets using simple prescribed wake methods 2011; .

[10] Gaunaa M, Johansen J. A Theoretical and Numerical Investigation of the Maximum Aerodynamic Efficiency of Wind Turbine Rotors with Winglets. *Technical Report*, DTU-Risø National Laboratory 2007.

[11] Madsen HA, Bak C, Døssing M, Mikkelsen R, Øye S. Validation and modification of the blade element momentum theory based on comparisons with actuator disc simulations. *Wind Energy* 2010; **13**(4):373–389.

[12] Timmer WA, van Rooij RPJOM. Summary of the Delft University wind turbine dedicated airfoils. *Proceedings of the AIAA-2003-0352*, 2003.

[13] Fuglsang P, Bak C. Development of the Risø wind turbine airfoils. *Wind Energy* 2004; **7**:145–162.

[14] Fuglsang P. Vingedesign. *Forskning i Aeroelasticitet EFP-2002. Bak C. (ed)* 2002; :49–64.

[15] Fuglsang P, Madsen HA. Optimization method for wind turbine rotors. *J. Wind Engineering and Industrial Aerodynamics. Vol 80.* 1999; .

[16] Fuglsang P, Thomsen K. Site Specific Design Optimization of Wind Turbines. *J. Solar Engineering* 2001; .

[17] Fuglsang P, Bak C, Schepers JG, Bulder B, Cockerill TT, Claiden P, Olesen A, van Rossen R. Site Specific Design Optimization of Wind Turbines. *Wind Energy* 2002; **5**:261–279.

[18] Jonkman J, Butterfield S, Musial W, Scott G. Definition of a 5-MW Reference Wind Turbine for Offshore System Development. *Technical Report NREL/TP-500-38060*, NREL National Renewable Energy Laboratory 2009.

[19] Nygaard TA. Optimization of Wind Turbine Rotors. PhD Thesis, NTNU Trondheim. Norges teknisk-naturvitenskapelige universitet. Institut for mekanikk, termo- og fluidmekanikk 1999.

[20] Merz KO. Conceptual Design of a Stall-Regulated Rotor for a Deepwater Offshore Wind Turbine. *Seminar Proceedings. 6th PhD Seminar on Wind Energy in Europe. NTNU Trondheim* 2010; .

[21] Hansen MH. Improved modal dynamics of wind turbines to avoid stall-induced vibrations. *Wind Energy* 2003; **6**:179–195.

[22] Hansen MH. Aeroelastic stability analysis of wind turbines using an eigenvalue approach. *Wind Energy* 2004; **7**:133–144.

[23] Hansen MH. Aeroelastic instability problems for wind turbines. *Wind Energy* 2007; **10**:551–577.

[24] Riziotis VA, Voutsinas SG, Politis ES, Chaviaropoulos PK. Aeroelastic stability of wind turbines: the problem the methods and the issue. *Wind Energy* 2004; **7**:373–392.

[25] Frandsen ST. Turbulence and turbulence generated structural loading in wind turbine clusters. *Doctoral thesis* 2007.

[26] Kristensen L, Fransen ST. Model for power spectra of the blade of a wind turbine measured from the moving frame of reference 1982; .

[27] Connel JR. Turbulence spectrum observed by a fast rotating wind turbine blade, Rep. PNL-3426, Battelle Pacific Northwest Laboratory, Richland, WA 99352 1980; .

[28] Døssing M. High Frequency Microphone Measurements for Transition Detection on Airfoils. *Risø R-report ISBN 978-87-550-3674-1*, Risø DTU, Wind Energy Department 2008.

[29] Bak C, Døssing M. Forskning i Aeroelasticitet EFP-2007. Wind Energy Department, Aeroelastic Design. Risø DTU 2007; :70–73.

[30] Døssing M. High Frequency Microphone Measurements for Transition Detection on Airfoils - Risø B1-18 Appendix Report. *Risø R-report ISBN 978-87-550-3675-8*, Risø DTU, Wind Energy Department 2008.

[31] Døssing M. High Frequency Microphone Measurements for Transition Detection on Airfoils - Risø C2-18 Appendix Report. *Risø R-report ISBN 978-87-550-3676-5*, Risø DTU, Wind Energy Department 2008.

[32] Døssing M. High Frequency Microphone Measurements for Transition Detection on Airfoils - NACA-0015 Appendix Report. *Risø R-report ISBN 978-87-550-3677-2*, Risø DTU, Wind Energy Department 2008.

[33] Døssing M. A detailed investigation of the corrected BEM method and the potential for improving blade design. EWEC 2009, conference paper, Marseilles, 2009.

[34] Døssing M, Bak C. A numerical and analytical investigation of blade fatigue loads on the NREL 5MW wind turbine. *Seminar Proceedings. 6th PhD Seminar on Wind Energy in Europe. NTNU Trondheim* 2010; .

[35] Drela M. XFOIL: An Analysis and Design System for Low Reynolds Number Airfoils. Lecture Notes in Engineering: Low Reynolds Number Aerodynamics, T.J. Mueller (ed.), Springer Verlag, New York, **54** 1989; .

[36] Bak C, Johansen J, Andersen PB. Three-dimensional corrections of airfoil characteristics based on pressure distributions 2006; .

[37] Larsen TJ. How to HAWC2, the user's manual. *Risø-R-1597(ver. 3-9)(en)*, Risø DTU, Technical University of Denmark 2009.

[38] Johansen J, Madsen HA, Gaunaa M, Bak C, Sørensen NN. Design of a wind turbine rotor for maximum aerodynamic efficiency. *Wind Energy* 2009; **12**:261–273.

[39] Megson THG. *Aircraft Structures for Engineering Students*, vol. Third Edition. Arnold, 1999.

[40] Bir GS. User's Guide to PreComp (Pre-Processor for Computing Composite Blade Properties. *NREL/TP-500-38929* 2006.

[41] Vanderplaats GN. *Numerical Optimization Techniques for Engineering Design with Applications.* McGraw-Hill Book Company, New York, 1984.

[42] IEC 61400-1. International Standard, Wind Turbines - Part 1: Design requirements (Third edition). *IEC 61400-1:2005(E)* 2005.

[43] Hansen MH, Gaunaa M, Madsen HA. A Beddoes-Leishman type dynamic stall model in state-space and indicial formulations. *Technical Report*, Risø National Laboratory 2004.

[44] Madsen HA, Mikkelsen R, Øye S, Bak C, Johansen J. A Detailed investigation of the Blade Element Momentum (BEM) model based on analytical and numerical results and proposal for modifications of the BEM model. *Journal of Physics: Conference Series 75 012016* 2007; .

[45] Madsen HA. A CFD analysis of the actuator disc flow compared with momentum theory results. *Proceedings of IEA Joint Action, Aerodynamics of Wind Turbines 10th Symposium*, 1996.

[46] Glauert H. Airplane propellers. *Aerodynamic Theory Volume IV.* 1963; .

[47] Madsen HA. Forskning i Aeroelasticitet EFP-2001. Wind Energy Department, Aeroelastic Design. Risø DTU. *Risø-R-1349(DA)* 2002; .

[48] Bak C. Forskning i Aeroelasticitet EFP-2002. Wind Energy Department, Aeroelastic Design. Risø DTU. *Risø-R-1434(DA)* 2004; .

[49] Bak C. Forskning i Aeroelasticitet EFP-2004. Wind Energy Department, Aeroelastic Design. Risø DTU. *Risø-R-1509(DA)* 2005; .

[50] Bak C. Research in Aeroelasticity EFP-2005. Wind Energy Department, Aeroelastic Design. Risø DTU. *Risø-R-1559(EN)* 2006; .

[51] Bak C. Research in Aeroelasticity EFP-2006. Wind Energy Department, Aeroelastic Design. Risø DTU. *Risø-R-1611(EN)* 2007; .

[52] Bak C. Research in Aeroelasticity EFP-2007. Wind Energy Department, Aeroelastic Design. Risø DTU. *Risø-R-1649(EN)* 2008; .

[53] Buhl T. Research in Aeroelasticity EFP-2007ii. Wind Energy Department, Aeroelastic Design. Risø DTU. *Risø-R-1698(EN)* 2009; .

[54] Chaviaropoulos PK. Similarity Rules for W/T Up-Scaling. *UPWIND Project, 1st Draft* 2006.

[55] Zenkert D, Battley M. *Foundations of Fibre Composites.* Department of Mechanical Engineering Technical University of Denmark, 2009.

[56] Sundström B. *Handbok och formelsamling i Hållfasthetslära.* Institutionen för hållfasthetslära, 1999.

[57] Bir GS, Migliore P. Preliminary Structural Design of Composite Blades for Two- and Three-Blade Rotors. *NREL/TP-500-31486* 2004.

[58] Jeppesen B, Krenk S. Cross Section - Program Description and User Manual. *Risø-M-2801* 1989.

[59] Hui Chen, Wenbin Yu, Capellaro M. A Critical Assesment of Computer Tools for Calculating Composite Wind Turbine Blade Properties 2009; .

[60] Giguére P, Selig MS. Blade Geometry Optimization for the Design of Wind Turbine Rotors. *A Collection of the 2000 ASME Wind Energy Symposium Technical Papers at the 38th AIAA Aerospace Sciences Meeting and Exhibit* 2000; .

[61] Fuglsang P, Sangill O, Hansen P. Design of a 21 m blade with risø-a1 airfoils for active stall controlled wind turbines. *Technical Report* 2002.

[62] Hendriks HB, Schepers JG, G vT, J SA, K BG. Aeroelastically optimised cost efficient wind turbine, a case study. *Proc. EUWEC'96, Goteborg, Sweden, pp 116-119* 1996; .

[63] Thomsen K. The statistical variation of wind turbine fatigue loads. *Technical Report* 1998.

[64] Eurocode 3: Design of steel structures - Part 1-9: Fatigue. DS/EN 1993-1-9 + AC. *Technical Report* 2007.

[65] Matsuiski M, Endo T. Fatigue of metals subjected to varying stress, Japan Soc. Mech. Engineering. 1969; .

[66] Suresh S. *Fatigue of Materials. Second Edition.* Cambridge University Press, 1998.

[67] Anderson JD. *Fundamentals of Aerodynamics*, vol. Fourth Edition. McGraw-Hill International Editions, 2005.

[68] White FM. *Viscous Fluid Flow*, vol. Second Edition. McGraw-Hill International Editions, 1991.

Nomenclature

a	Axial induction factor	-
a'	Tangential induction factor	-
$a\,,b$	Prescribed v-deflection coefficients	
$\mathbf{A}$	Structural matrix	
A	Weibull parameter	m/s
A	Rotor swept area (undeformed)	m^2
A_0	Closed section area	m^2
A_1	Aerodynamic design coefficient	-
A_2	Aerodynamic design coefficient	-
c	Blade chord length	m
$\mathbf{C}$	Chord scaling matrix (fixed rel. shell thk.)	m^2, m^4
C	Weibull parameter	-
c_1	Fatigue load sensor	m^4/s
c_2	Fatigue stress sensor	m/s
C_A	Structural coefficient	-
C_{A_0}	Structural coefficient	-
C_d	Drag coefficient	-
$C_{D_{xy}}$	Structural coefficient	-
C_F	Flapwise bending moment coefficient (Aerodynamic)	-
$C_{F,F}$	Tip loss correction on flap moment coefficient	-
C_I	Structural coefficient	-
C_l	Lift coefficient	-
C_p	Local power coefficient	-
C_P	Power coefficient	-
$C_{P,a'}$	Wake swirl correction on power coefficient	-
$C_{P,d}$	C_P component due to drag forces	-
$C_{P,l}$	C_P component due to lift forces	-

C_q	Local torque coefficient	-
C_S	Structural coefficient	-
C_t	Local thrust coefficient	-
C_T	Thrust coefficient	-
$C_{T,F}$	Tip loss correction on thrust coefficient	-
C_{t2}	Thrust corrected for tip losses (C_t/F)	-
$C_{t2,d}$	Design C_{t2}	-
C_x	Local force coefficient, edge	-
C_x	Tangential force coefficient	-
C_y	Local force coefficient, flap	-
C_y	Axial force coefficient	-
d	Single-cycle damage	-
d	Blade section drag	N/m
$\mathbf{D}$	Chord scaling matrix (fixed abs. shell thk.)	m, m^3
D	Fatigue damage	-
E	Elastic modulus	Pa
EA	Longitudinal stiffness	N
ED_{xy}	Moment of centrifugal stiffness	Nm^2
EI_x, EI_y	Moment of stiffness inertia	Nm^2
$EI_{x'}$, $EI_{y'}$	Moment of stiffness inertia about principal axis	Nm^2
ES	Moment of stiffness	Nm
f	Tip slope factor	-
f	Eigenfrequency	Hz
f_{eq}	Equivalent fatigue cycle frequency	Hz
f_j	Fraction of lifetime - timeseries j	-
f_t	Profile thickness factor	-
$f(V_0)$	Wind speed distribution	(m/s)$^{-1}$
$f_W(V_0)$	Weibull wind distribution	(m/s)$^{-1}$
F	Prandtl's tip loss factor	-
F_T	Correlation function, tip loss on thrust	-
F_F	Correlation function, tip loss on flap moment	-
g	Gravitational acceleration	m/s^2
G	Shear modulus (in plane)	Pa
GJ	Torsion stiffness	Nm^2
$\mathbf{h}$	Absolute shell thickness vector	m
h	Laminate thickness	-
h_A	Weibull parameter	m
i	Bin index	-
I	Turbulence intensity	-
I_{ref}	IEC reference turbulence intensity	-
j	Timeseries index	-
k_1, k_2, k_3	Constants, $a(C_t/F)$ relation	-
k_x, k_y	Shear factor	-
k	Coefficient relating load and stress	Pa/N, Pa/Nm

l	Blade section lift	N/m
l	Turbulence length scale	m
m	Wöhler-curve parameter	-
m	Blade section mass	Kg/m
$\mathbf{M}$	Bending moment vector	Nm
M	Blade mass	Kg
M_e	Edgewise bending moment (aerodynamic)	Nm
M_f	Flapwise bending moment (aerodynamic)	Nm
M'_i	Bending moment about principal axes	Nm
M_x	Edgewise bending moment	Nm
M_y	Flapwise bending moment	Nm
M_F	Root flapwise bending moment (aerodynamic)	Nm
M_S	Shaft driving moment (aerodynamic)	Nm
n	lifetime cycles	-
n'	Average RFC cycles per second	Hz
n'_{tip}	n' evaluated at blade tip	Hz
n_{eq}	Equivalent number of fatigue cycles	-
n_t	RFC of timeseries of length t	-
N	Cycles to failure (Wöhler-curve)	-
N_B	Number of blades	-
obj	Objective function	
$\mathbf{p}$	Distributed load vector	N/m
p_x	Distributed load (edgewise)	N/m
p_y	Distributed load (flapwise)	N/m
p_z	Distributed load (spanwise)	N/m
p_w	Pressure from wake rotation	-
p_W	Cumulative Weibull wind distribution	-
P	Power	W
$\mathbf{r}$	Moment-arm vector	m
r	Coordinate, radius	m
$\mathbf{R}$	Coordinate change matrix	-
R	Rotor radius	m
R	Load-range	N, Nm
R_{eq}	Equivalent fatigue load	N, Nm
$\mathbf{s}$	Strain evaluation point	m
s	Surface curve parameter	m
S	Stress-range	Pa
S_{eq}	Equivalent fatigue stress	Pa
S_0	Wöhler-curve parameter	Pa
t	Timeseries length	s
t	Profile relative thickness	-
t_a	Profile absolute thickness	m
$\mathbf{T}$	Internal force vector	N
T	Thrust	N

T	Wind turbine lifetime	s
u	Blade deflection, edgewise	m
v	Blade deflection, flapwise	m
v_a	Axial velocity in rotor plane	m/s
v_{ave}	Average wind speed	m/s
v_{rel}	Local relative velocity	m/s
v_t	Velocity in rotor plane, relative to blade - edgewise	m/s
V_{ref}	IEC reference wind speed	m/s
V_0	Wind speed	m/s
$\mathbf{x}$	Relative shell thickness vector	-
x	Continuous RFC variable	-
x	Blade coordinate - edgewise	m
x_i	Sector position, chordwise	m
x_{SC}	Position, shear center	m
x_{EA}	Position, elastic axis	m
x_{CG}	Position, center of gravity	m
x_{AC}	Position, aerodynamic center	m
$\mathbf{y}$	Structural property vector	
y	Blade coordinate, flapwise	m
y	Cross section coordinate (relative to EA)	m
y_{EA}	Position, elastic axis	m
y_{CG}	Position, center of gravity	m
z_0	Roughness length	m
$\mathbf{z}$	Absolute-change in shell thickness vector	m
z_{hub}	Hub height	m
z, r	Blade coordinate, Spanwise	m
α_d	Design angle of attack	radians (degree)
α	Local angle of attack	radians (degree)
α	Main spar relative thickness	-
α	Shear factor	-
β	Twist	radians (degree)
β	Relative thickness	-
χ	Dimensionless tip deflection	-
δ	Shear web thickness	-
Δ	Prefix denoting range	-
Δv_w	Correction for wake rotation	-
Δv_e	Correction for wake expansion	-
ϵ	Strain	-
ϵ_a	cyclic strain amplitude (fatigue tests)	-
γ	Leading/Trailing edge laminate thickness	-
$\mathbf{\Gamma}$	Bound circulation vector	m^2/s
κ	Curvature	m^{-1}
λ	Tip speed ratio	-
λ_d	Design tip speed ratio	-

λ_r	Local speed ratio	-
ν	Angle to first principal axis (relative to chord)	radians (degree)
ν_{12}	Poissons ratio	-
Ω	Rotational speed	s^{-1}, RPM
ϕ	Inflow angle	radians (degrees)
Φ	Tip slope (dimensionless)	-
ρ	Mass density	kg/m^3
ρS	Moment of mass	kg
σ_1	Turbulence standard deviation - wind direction	m/s
σ_a	Cyclic stress amplitude (fatigue tests)	Pa
θ	Azimuth angle (0=blade pointing up)	radian (degree)
θ	Deformation angle	radian (degree)
$\theta\prime$	Deformation angle about principal axis	radian (degree)
θ_c	Angle to chord line (relative to rotor plane)	radians (degree)
θ_p	Pitch angle	radians (degree)
θ_z	Angle to first principal axis (relative to rotor plane)	radians (degree)
AC	Aerodynamic center	
ACD	Actuator disc method	
AEP	Annual energy production	Wh
AED	Aeroelastic design group. Risø DTU, Denmark	
ASR	Active stall regulated turbine	
BEM	Blade element momentum method	
BEM_{cor}	BEM method with corrections	
C	Cost	
CFD	Computational fluid dynamics	
CG	Center of gravity	
COE	Cost of energy	
DLC	Design loadcase	
EA	Elastic axis	
EOG	Extreme operating gust	
ETM	Extreme turbulence model	
EWM	Extreme wind model	
HAWT	Horizontal axis wind turbine	
HAWC2	Aeroelastic code [37]	
NTM	Normal turbulence model	
PRVS	Pitch regulated variable speed	
Re	Reynolds number	
RFC	Rainflow count	
RPM	Revolutions per minute	
SC	Shear center	
TI	Turbulence intensity	
B1-xx	Risø airfoil family	
DUxx	TU Delft airfoil family	

APPENDIX A

Basic theory

The following is a summary of basic rotor aerodynamic theory.

A.1 Geometrical definitions

Figures 4.3 and A.1 illustrates relevant quantities.

Local relative velocity (not including spanwise flow)

$$v_{rel} = \sqrt{v_a^2 + v_t^2} \tag{A.1}$$

Angle to chord line (relative to rotor plane)

$$\theta_c = \theta_p + \beta \tag{A.2}$$

Angle to first principal axis (relative to rotor plane)

$$\theta_z = \theta_p + \beta + \nu \tag{A.3}$$

Angle of attack

$$\alpha = \phi - \theta_p - \beta \tag{A.4}$$

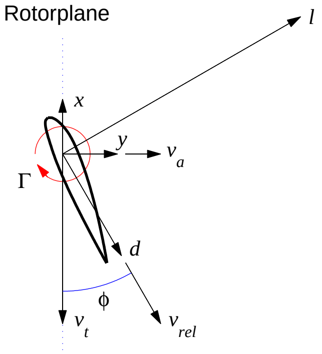

Figure A.1: Sketch of basic properties relative to a blade section

Inflow angle (relative to rotor plane)

$$\phi = \arctan\left(\frac{v_a}{v_t}\right) \tag{A.5}$$

Relations

$$v_{rel}\sin\phi = v_a \tag{A.6}$$

$$v_{rel}\cos\phi = v_t \tag{A.7}$$

A.2 2D aerodynamic forces

Lift and drag coefficients

$$C_l = \frac{l}{{}^1\!/_2\rho v_{rel}^2 c} \tag{A.8}$$

$$C_d = \frac{d}{{}^1\!/_2\rho v_{rel}^2 c} \tag{A.9}$$

$$C_d = \frac{C_l}{{}^l\!/_d} \tag{A.10}$$

Tangential force coefficient

$$C_x = C_l \sin\phi - C_d \cos\phi \tag{A.11}$$

Normal force coefficient

$$C_y = C_l \cos\phi + C_d \sin\phi \tag{A.12}$$

Local power coefficient

$$C_p = \frac{\Omega v_{rel}^2 C_x c N_B}{V_0^3 2\pi} \tag{A.13}$$

Local thrust coefficient

$$C_t = \frac{v_{rel}^2 C_y c N_B}{V_0^2 2\pi r} \tag{A.14}$$

Local torque coefficient

$$C_q = \frac{v_{rel}^2 C_x c N_B}{V_0^2 2\pi r} \tag{A.15}$$

Relations

$$C_q = \frac{C_p}{\lambda_r} \tag{A.16}$$

$$\frac{C_q}{C_t} = \frac{C_x}{C_y} \tag{A.17}$$

Using (A.21) to calculate the inflow angle the following is true with great accuracy for large $^l/_d$

$$\frac{C_p}{C_t} = \lambda_r \left(\frac{v_a}{v_t} - \frac{1}{^l/_d} \right) \tag{A.18}$$

A.2.0.1 Ideal energy conversion

If the flow angle is estimated using ideal energy conversion then the following equations are good approximations

$$C_d = 0 \tag{A.19}$$

$$C_x = C_l \sin\phi \tag{A.20}$$

$$C_y = C_l \cos\phi \tag{A.21}$$

$$\frac{C_x}{C_y} = \tan\phi = \frac{v_a}{v_t} \tag{A.22}$$

Note that ideal energy conversion (d=0) is a very good approximation when related to calculation of angles, e.g. inflow angle ϕ. However, the drag is not negligible when calculating shaft power, edgewise bending moments and other properties related to forces in the rotor plane.

A.3 Dimensional analysis, aerodynamics

Tip speed ratio and local speed ratio

$$\lambda = \frac{\Omega R}{V_0} \tag{A.23}$$

$$\lambda_r = \frac{\Omega r}{V_0} = \frac{r}{R}\lambda \tag{A.24}$$

For similar turbines operating at similar λ, the following dimensionless quantities are constant. Note that similar turbine means similar geometrical shape or similar load distribution (both may be expressed dimensionless). A similar load distribution may be obtained for different geometries.

Power coefficient

$$C_P = \frac{P}{{}^1\!/\!{}_2\rho V_0^3 \pi R^2} \tag{A.25}$$

Thrust coefficient

$$C_T = \frac{T}{{}^1\!/\!{}_2\rho V_0^2 \pi R^2} \tag{A.26}$$

Flapwise root moment coefficient

$$C_F = \frac{M_F N_B}{{}^1\!/\!{}_2\rho V_0^2 \pi R^3} \tag{A.27}$$

Flapwise moment coefficient

$$C_f = \frac{M_f N_B}{{}^1\!/\!_2 \rho V_0^2 \pi R^3} \tag{A.28}$$

Dimensionless bound circulation

$$\Gamma^* = \frac{\Gamma}{V_0 R} \tag{A.29}$$

Note that the dimensionless velocities v_a^*, v_t^*, and v_{rel}^* are also constant due to flow similarity.

A.4 Mechanical properties due to aerodynamics

Power coefficient

$$C_P = \frac{2}{R^2} \int_{blade} r C_p \, dr \tag{A.30}$$

Thrust coefficient

$$C_T = \frac{2}{R^2} \int_{blade} r C_t \, dr \tag{A.31}$$

Flapwise bending moment coefficient (about rotor centre)

$$C_F = \frac{2}{R^3} \int_0^R r^2 C_t \, dr \tag{A.32}$$

Flapwise bending moment coefficient at radius r

$$C_f = \frac{2}{R^3} \int_r^R (r' - r) r' C_t \, dr' \tag{A.33}$$

A.5 Blade element momentum method

A.5.1 Tip losses

Prandtl's tip loss factor is defined as

$$F = \frac{2}{\pi} \arccos\left(e^{-f}\right) \tag{A.34}$$

where

$$f = \frac{N_B}{2} \frac{R-r}{r \sin\phi} \tag{A.35}$$

Linearization around r^*=1 yields a good approximation over the radii where tip losses are significant

$$f \cong -A_1(r^* - 1)\,, \quad A_1 >\approx 6 \tag{A.36}$$

where

$$A_1 = \frac{1}{2} N_B \sqrt{1 + \frac{(1+a')^2 \lambda^2}{(1-a)^2}} \cong \frac{1}{2} N_B \sqrt{1 + \frac{\lambda^2}{(1-a)^2}} \tag{A.37}$$

Note that increasing A_1 is equivalent to decreasing F. To summarize, a good approximation to (A.34) is

$$F = \frac{2}{\pi} \arccos\left(e^{A_1(r^*-1)}\right) \tag{A.38}$$

A_1 can often be considered as a constant design parameter.
The point where tip losses become significant r^*_F can be found by setting f to an appropriate value. E.g. setting f=-4.0 yields

$$r^*_F = 1 - \frac{4.0}{A_1} \quad \Leftrightarrow \quad F = 0.988 \tag{A.39}$$

A.5.2 Induction factors

Relation between axial induction and actuator disc thrust (Ref. [11])

$$a = k_3 \left(\frac{C_t}{F}\right)^3 + k_2 \left(\frac{C_t}{F}\right)^2 + k_1 \frac{C_t}{F} \tag{A.40}$$

For an undeflected, unconed rotor

$$k_3 = 0.08921\,, \quad k_2 = 0.05450\,, \quad k_1 = 0.25116 \tag{A.41}$$

Momentum theory solution for tangential induction

$$a' = \frac{C_q}{4(1-a)\lambda_r} \tag{A.42}$$

If the flow angle is calculated using ideal energy conversion then a' can be written as

$$a' = \frac{C_t}{4(1+a')\lambda_r^2} \Rightarrow a' = \frac{1}{2}\sqrt{1+\frac{C_t}{\lambda_r^2}} - \frac{1}{2} \tag{A.43}$$

An iteration loop is necessary in order to update and converge all forces and flow properties.
It is safe to substitute C_t/F for C_t because a' is negligible in the tip region. Thus, the following expression is, with good accuracy, also valid everywhere on the blade

$$a' = \frac{1}{2}\sqrt{1+\frac{C_t/F}{\lambda_r^2}} - \frac{1}{2} \tag{A.44}$$

A.5.3 Velocities and corrections for wake expansion and rotation

It is possible to include corrections for wake expansion and rotations. The derivation and calculation of these are explained in [11]. The result is 2 corrections on the axial flow velocity, which becomes

$$v_a = (1 - a + \Delta v_w - \Delta v_e)V_0 \tag{A.45}$$

where Δv_w is a correction for wake rotation and Δv_e is a correction for wake rotation. The tangential velocity is

$$v_t = \lambda_r(1+a')V_0 \tag{A.46}$$

Thus, the velocities may be expressed dimensionless as

$$v_a^* = \frac{v_a}{V_0}\,, \quad v_t^* = \frac{v_t}{V_0} \tag{A.47}$$

A.5.4 Blade design parameter

Combining (A.21) and (A.14) yields

$$C_t = \frac{v_{rel}^2 C_l c N_B \cos\phi}{V_0^2 2\pi r} \tag{A.48}$$

I.e. the drag component in the axial direction is assumed negligible compared to the lift. Rewritting with dimensionless quantities and rearranging yields

$$c^* C_l = \frac{C_t 2\pi}{N_B} \frac{r^*}{{v_{rel}^*}^2 \cos\phi} \tag{A.49}$$

This result can be regarded as independent of number of blades if tip losses are neglected. In that case the following is a constant which represents the 3D aerodynamic design, i.e. the design thrust at desired tip speed ratio.

$$c^* C_l N_B \tag{A.50}$$

A.6 Lifting line theory

Joukowsky theorem

$$\mathbf{L} = \rho \mathbf{Q} \times \mathbf{\Gamma} \tag{A.51}$$

For turbines the dimensionless bound circulation is

$$\Gamma^* = C_l {}^1\!/_2 v_{rel}^* c^* \tag{A.52}$$

Inviscous power coefficient due to lift forces

$$C_{P,l} = \frac{2 N_B \lambda}{\pi} \int_{blade} r^* v_a^* \Gamma^* \, dr^* \tag{A.53}$$

Viscous power coefficient due to drag forces calculated from known lift to drag ratio

$$C_{P,d} = -\frac{2 N_B \lambda}{\pi} \int_{blade} \left({}^l\!/_d\right)^{-1} r^* v_t^* \Gamma^* \, dr^* \tag{A.54}$$

Power coefficient

$$C_P = C_{P,l} + C_{P,d} \tag{A.55}$$

Appendix B

Analytical design of turbines with constant thrust

In the analysis wake swirl losses and tip losses are taken into account. The BEM corrections for wake rotation and expansion are not included, but the method still provides a good first approximation.

The design thrust is defined as

$$C_{t2,d} = ({}^{C_t}/_{F})_{design} \tag{B.1}$$

This is related to a constant design value of a through equation (A.40). The actual mechanical thrust on the blade is

$$C_t = C_{t2,d} F \tag{B.2}$$

B.1 Thrust and tip losses

Neglect drag forces when calculating the thrust. The thrust coefficient integral (A.31) becomes

$$C_T = 2 C_{t2,d} \int_0^1 r^* F \, dr^* \tag{B.3}$$

Alternatively write this as the thrust calculated by neglecting tip loss (first term) plus the thrust caused by tip loss (second term)

$$C_T = 2C_{t2,d}\int_0^1 r^*\,dr^* + C_{T,F} = C_{t2,d} + C_{T,F} \tag{B.4}$$

This yields

$$\frac{C_{T,F}}{C_{t2,d}} = 2\int_0^1 r^* F\,dr^* - 1 \tag{B.5}$$

Assume a'=0. Then, because a is constant, A_1 is also a constant design parameter, describing the whole turbine. The tip loss is therefore only a function of r^* and the constant A_1

$$F = F(A_1, r^*) \tag{B.6}$$

By varying A_1 and numerically integrating (B.5) a series of data has been obtained. The following expression fits the data well for A_1 >5

$$\frac{C_{T,F}}{C_{t2,d}} = -\frac{1.392}{1.2 + A_1} \tag{B.7}$$

Figure B.1 shows the numerically integrated value of $C_{T,F}$ and the polynomial fit $B.7$.

B.2 Flapwise moment and tip losses

Equation (A.32) combined with (B.2) yields the following integral for the flap moment coefficient

$$C_F = C_{t2,d} 2\int_0^1 {r^*}^2 F\,dr^* \tag{B.8}$$

This can also be rewritten as C_F without tip loss (first term) plus the contribution from tip loss (second term)

$$C_F = {}^2\!/_3 C_{t2,d} + C_{F,F} \tag{B.9}$$

Combining these equations yields

$$\frac{C_{F,F}}{C_{t2,d}} = 2\int_0^1 {r^*}^2 F\,dr^* - {}^2\!/_3 \tag{B.10}$$

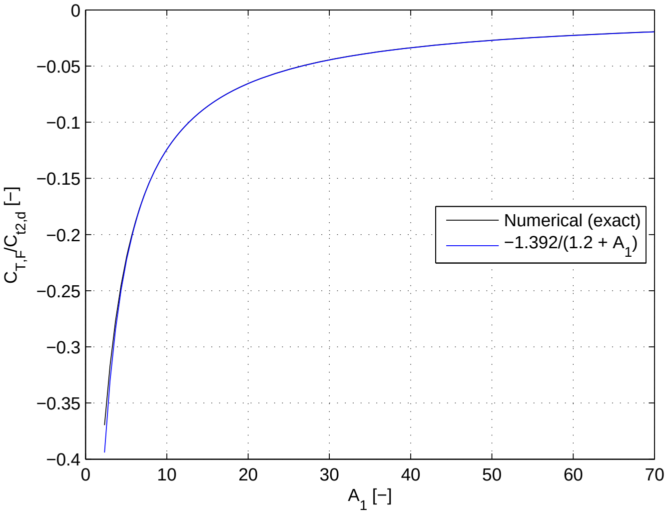

Figure B.1: $C_{T,F}$ versus A_1.

The integral in the above has been solved numerically for varying values of A_1. The following expression fits the data well for $A_1 > 5$

$$2\int_{blade} {r^*}^2 F\, dr^* = 2/3 - \frac{1.4}{2.3 + A_1} \tag{B.11}$$

Inserting above yields

$$\frac{C_{F,F}}{C_{t2,d}} = -\frac{1.4}{2.3 + A_1} \tag{B.12}$$

Figure B.2 shows the numerically integrated value of $C_{F,F}$ and the polynomial fit B.12. Note that this decrease in the flap moment is the same for all sections of the blade where tip losses are not present. In theory tip losses are present everywhere but here it will be defined that they are zero for $r^* < r^*_F$. The local flap moment is

$$C_f(r^*) = C_{t2,d} 2 \int_{r^*}^{1} (r - r^*) r F\, dr \tag{B.13}$$

This integral is divided into two and it is assumed that tip losses are not important in the first (F=1)

$$\frac{C_f(r^*)}{C_{t2,d}} = 2\int_{r^*}^{r^*_F} (r - r^*) r\, dr + 2\int_{r^*_F}^{1} (r - r^*) r F\, dr \tag{B.14}$$

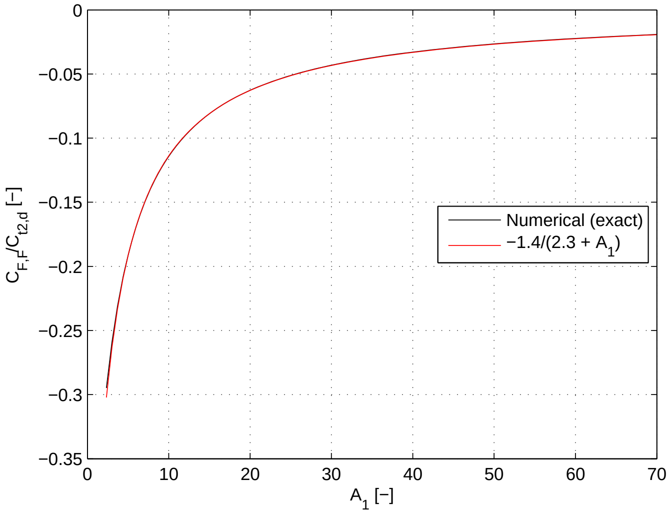

Figure B.2: $C_{F,F}$ versus A_1.

The first integral in (B.14) has solution

$$2\int_{r^*}^{r_F^*} (r - r^*) r \, dr = {}^2\!/_3 {r_F^*}^3 + {}^1\!/_3 {r^*}^3 - r^* {r_F^*}^2 \tag{B.15}$$

The second integral in (B.14) is divided into two

$$2\int_{r_F^*}^{1} (r - r^*) r F \, dr = 2\int_{r_F^*}^{1} r^2 F \, dr - 2r^* \int_{r_F^*}^{1} r F \, dr \tag{B.16}$$

These integrals are of the same types as in (B.5) and (B.10). However, the limits are not correct and should be from 0 to 1. This can be obtained as seen below, where it is again used that F=1 for $r^* < r_F^*$. The first integral:

$$2\int_{0}^{r_F^*} r^2 \, dr + 2\int_{r_F^*}^{1} r^2 F \, dr = 2\int_{0}^{1} r^2 F \, dr \tag{B.17}$$

$$\Leftrightarrow 2\int_{r_F^*}^{1} r^2 F \, dr = 2\int_{0}^{1} r^2 F \, dr - 2\int_{0}^{r_F^*} r^2 \, dr \tag{B.18}$$

Inserting (B.10) and solving the last integral yields

$$2\int_{r_F^*}^{1} r^2 F \, dr = \frac{C_{F,F}}{C_{t2,d}} + {}^2\!/_3 - {}^2\!/_3 {r^*}^3 \tag{B.19}$$

By the same method and inserting (B.5) the second integral is rewritten:

$$2\int_{r_F^*}^{1} rF\,dr = 1 + \frac{C_{T,F}}{C_{t2,d}} - {r_F^*}^2 \tag{B.20}$$

Substituting everything back into () and simplifying yields the final result

$$C_f(r^*) = C_{t2,d}\left({}^1\!/\!{}_3 {r^*}^3 - r^* + {}^2\!/\!{}_3\right) + C_{F,F} - r^* C_{T,F} \tag{B.21}$$

where

$$r^* < r_F^* \tag{B.22}$$

However, test examples show that this limit can be extended significantly to

$$r^* < \frac{r_F^* + 1}{2} = 1 - \frac{2}{A_1} \tag{B.23}$$

B.3 Power and wake swirl losses

Combining (A.18), (A.30) and (B.2) yields the local power coefficient

$$C_p = C_{t2,d} F\left(\frac{1-a}{1+a'} - \frac{\lambda_r}{{}^l\!/\!{}_d}\right) \tag{B.24}$$

and the integrals for the total power coefficient

$$C_P = C_{t2,d}(1-a)2\int_0^1 \frac{1}{1+a'} r^* F\,dr^* - \frac{\lambda}{{}^l\!/\!{}_d} C_{t2,d}2\int_0^1 {r^*}^2 F dr^* \tag{B.25}$$

Wake swirl losses are represented by a' appearing in the denominator. Alternatively write this as an integral where a' is neglected (first term) plus the power caused by wake swirl (second term) plus the power caused by drag (third term)

$$C_P = 2C_{t2,d}(1-a)\int_0^1 r^* F\,dr^* + C_{P,a'} + C_{P,d} \tag{B.26}$$

where

$$C_{P,d} = -\frac{\lambda}{{}^l\!/\!{}_d} C_{t2,d}2\int_0^1 {r^*}^2 F dr^* \tag{B.27}$$

Using (B.3) this can be rewritten as

$$C_P = (1-a)C_T + C_{P,a'} + C_{P,d} \tag{B.28}$$

Comparing (B.27) with (B.8) it is seen that

$$C_{P,d} = -\frac{\lambda}{{}^{l}\!/_{d}} C_F \tag{B.29}$$

It will be assumed that wake swirl losses are independent of tip losses and drag losses. This means that $C_{P,a'}$ can be evaluated on a rotor where those losses are neglected, i.e. F=1 everywhere and $C_{P,d}$=0. Setting F=1 means that C_T=$C_{t2,d}$. Substituting into (B.28) yields

$$2C_{t2,d}(1-a)\int_0^1 \frac{1}{1+a'} r^*\, dr^* = (1-a)C_{t2,d} + C_{P,a'} \tag{B.30}$$

$$\Leftrightarrow \frac{C_{P,a'}}{C_{t2,d}(1-a)} = \int_0^1 \frac{2}{1+a'} r^* dr^* - 1 \tag{B.31}$$

The analytical solution can be found by use of equation (A.44)

$$\frac{C_{P,a'}}{C_{t2,d}(1-a)} = {}^{1}\!/_{4} A_2 \ln(A_2) + \sqrt{1+A_2}\left(\frac{1}{A_2} + {}^{1}\!/_{2}\right) \tag{B.32}$$

$$- {}^{1}\!/_{2} A_2 \ln(1+\sqrt{1+A_2}) - 1 - \frac{1}{A_2} \tag{B.33}$$

where A_2 is

$$A_2 = \frac{C_{t2,d}}{\lambda^2} \tag{B.34}$$

A polynomial fit valid for A_2 <0.065 is

$$\frac{C_{P,a'}}{C_{t2,d}(1-a)} = 4.906 A_2^2 - 1.173 A_2 - 0.002362 \tag{B.35}$$

Note that the effect of tip losses on the power carries over directly through the thrust coefficient in (B.28).

B.4 Circulation and viscous drag losses

Equation (B.25) on differential form is

$$dC_P = 2C_{t2,d}(1-a)\frac{1}{1+a'} r^* F\, dr^* \tag{B.36}$$

The power coefficient based on inviscous theory is equation (A.53). On differential form it is

$$dC_{P,l} = \frac{2N_B\lambda}{\pi} r^* v_a^* \Gamma^*\, dr^* \tag{B.37}$$

Substituting v_a^*=$(1-a)$ and comparing the above expressions yields

$$\Gamma^* = C_{t2,d} \frac{\pi}{N_B \lambda} \frac{F}{(1+a')} \tag{B.38}$$

Substituting this result into (A.54) yields an expression for the power losses due to viscous drag

$$C_{P,d} = -2\lambda C_{t2,d} \int_0^1 \left({}^l\!/\!_d\right)^{-1} r^{*2} F \, dr^* \tag{B.39}$$

Assuming constant ${}^l\!/\!_d$ and rewriting yields

$$\frac{C_{P,d}}{\lambda C_{t2,d} \left({}^l\!/\!_d\right)^{-1}} = -2 \int_0^1 r^{*2} F \, dr^* \tag{B.40}$$

The integral is the same as the one appearing in (B.10). Combining with the above yields

$$\frac{C_{P,d}}{\lambda C_{t2,d} \left({}^l\!/\!_d\right)^{-1}} = -\frac{C_{F,F}}{C_{t2,d}} - {}^2\!/\!_3 \tag{B.41}$$

Using (B.9) this can finally be written as

$$\frac{C_{P,d}}{\lambda \left({}^l\!/\!_d\right)^{-1}} = -C_F \tag{B.42}$$

This should *not* be interpreted as if $C_{P,d}$ depends on C_F. It is merely a result of both depending on the same type of integral (i.e. (B.10))

B.5 Flow angle, lift coefficient and chord

The flow angle can be calculated using Equation (A.44) and the BEM equations with Δv_w=Δv_e=0.

$$\tan\phi = \frac{1-a}{{}^1\!/\!_2 \left(1 + \sqrt{1 + \frac{A_2}{r^{*2}}}\right) \lambda r^*} \tag{B.43}$$

The blade twist is then defined by the design angle of attack α_d

$$\beta = \phi - \alpha_d - \theta_p \tag{B.44}$$

The design parameter follows from (A.49) which may be rearranged as

$$c^* C_l N_B = C_{t2,d} \frac{2\pi F r^*}{((1-a)^2 + \lambda^2 r^{*2}(1+a')^2)\cos\phi} \tag{B.45}$$

$$c^* C_l N_B \cong C_{t2,d} \frac{2\pi F r^*}{(1-a)^2 + \lambda^2 r^{*2}} \tag{B.46}$$

$$c^* C_l N_B \approx C_{t2,d} \frac{2\pi r^*}{(1-a)^2 + \lambda^2 r^{*2}} \tag{B.47}$$

(B.47) is only valid near the center of the blade where tip-losses and wake swirl is negligible.

B.6 Resume

Design parameters (model input)

$$\lambda\,, \quad C_{t2,d} = \left({}^{C_t}\!/_{F}\right)_{design} \tag{B.48}$$

$$\tag{B.49}$$

Design coefficients

$$A_1 = \frac{1}{2} N_B \sqrt{1 + \frac{\lambda^2}{(1-a)^2}} \tag{B.50}$$

$$A_2 = \frac{C_{t2,d}}{\lambda^2} \tag{B.51}$$

Momentum theory

$$a = k_3 C_{t2,d}^3 + k_2 C_{t2,d}^2 + k_1 C_{t2,d} \tag{B.52}$$

$$a' = \frac{1}{2}\sqrt{1 + \frac{A_2}{r^{*2}}} - \frac{1}{2} \tag{B.53}$$

Integral quantities

$$C_T = C_{t2,d} + C_{T,F} \tag{B.54}$$

$$C_F = {}^2\!/_3 C_{t2,d} + C_{F,F} \tag{B.55}$$

$$C_{P,d} = -C_F \lambda \left({}^{l}\!/_{d}\right)^{-1} \tag{B.56}$$

$$C_P = (1-a)C_T + C_{P,a'} + C_{P,d} \tag{B.57}$$

Distributed quantities

$$\Gamma^* = C_{t2,d}\frac{\pi}{N_B\lambda}\frac{F}{(1+a')} \tag{B.58}$$

$$C_t = C_{t2,d}F \tag{B.59}$$

$$C_p = C_{t2,d}F\left(\frac{1-a}{1+a'} - \frac{\lambda_r}{{}^{l}\!/\!{}_{d}}\right) \tag{B.60}$$

$$C_f = C_{t2,d}\left({}^{1}\!/\!{}_{3}{r^*}^3 - r^* + {}^{2}\!/\!{}_{3}\right) + C_{F,F} - r^*C_{T,F} \quad , \; r^* < \frac{r_F^* + 1}{2} \tag{B.61}$$

Tip loss correction on total thrust (A_1 >5)

$$C_{T,F} = -\frac{1.392}{1.2 + A_1}C_{t2,d} = F_T(A_1)C_{t2,d} \tag{B.62}$$

Tip loss correction on flap moment (A_1 >5)

$$C_{F,F} = -\frac{1.4}{2.3 + A_1}C_{t2,d} = F_F(A_1)C_{t2,d} \tag{B.63}$$

Correction for wake swirl losses (A_2 <0.065)

$$C_{P,a'} = \left(4.906A_2^2 - 1.173A_2 - 0.002362\right)C_{t2,d}(1-a) \tag{B.64}$$

APPENDIX C

Fatigue

The following is a description of fatigue analysis of timeseries. The analysis is based on the Palmgreen-Miner theory of linear damage accumulation and rainflow-counting (RFC) of timeseries of loads.

A discussion of the same topic is given by Thomsen [63]. A thorough discussion of fatigue data for fibre laminates is found in [55]. Data for metals can be found in e.g. [56].

C.1 Material data

Fatigue test data is presented in SN-graph's (Wöhler curves) which shows the cycles to failure N versus stress S. In this text S is the stress range, but note that the reported stress often is the amplitude of a cyclic load σ_a. They are related as

$$S = 2\sigma_a \tag{C.1}$$

For fibre composites the strain amplitude ϵ_a is often used instead of the stress. The reason is that ϵ_a is relatively independent of fibre angles and volume fractions. σ_a, on the other hand, depends heavily on the fibre angles and volume fractions. In this case:

$$S = 2E\epsilon_a \tag{C.2}$$

Where E is the elastic modulus, which must correspond to the direction of applied stress. A simplified material SN-curve, representing the high-cycle fatigue, can be defined as

$$\log S_0 - \frac{1}{m}\log N = \log S \quad \Leftrightarrow \quad N = \left(\frac{S_0}{S}\right)^m \tag{C.3}$$

Where S_0 and m are material constants. Representative values for the material constants for unidirectional glass-epoxy composite materials are

$$m = 10 \tag{C.4}$$

$$S_0 = 2E \cdot 0.031 \tag{C.5}$$

In this form the SN-curve is extremely simplified. Among other things, the data depends on the mean stress level, which often is different from zero. The allowable stress ranges are smaller than the largest described by (C.3) because otherwise the material will go into low cycle fatigue and finally reach the yield stress. The uncertainties makes it very complicated to make an exact assessment of the fatigue damage and because of this the concept of an equivalent load is introduced next.

C.2 Load-stress relations

For a given load R, e.g. a bending moment, the stress may depend on many factors. It will be assumed that a linear relation holds

$$S = kR \tag{C.6}$$

E.g. using Bernoulli-Euler beam theory the axial strain in the outermost fibre, at distance y from the neutral axis, due to a bending moment M, is

$$\epsilon = \frac{M}{EI_x}y \tag{C.7}$$

The fibre stress is

$$\sigma = \frac{E(y)y}{EI_x}M \quad \Rightarrow \quad k = \frac{E(y)y}{EI_x} \tag{C.8}$$

Where $E(y)$ is the elastic modulus at y.

C.3 Damage analysis and equivalent load

The analysis aims at determining the component damage in an arbitrarily selected lifetime T, based on a representative timeseries of a given load, in timespan t.

The input to the fatigue analysis is a timeseries of a given load. Using Rainflow counting the series is rearranged into bins where each bin holds the number of cycles n_i of a defined magnitude R_i. This is the range of the cycle and not the amplitude

$$R_i = R_{i,max} - R_{i,min} \tag{C.9}$$

Index i refers to the bin number. The bins are defined in order to cover the entire range of signal-values. In the following the material stress S is relevant and this can be related to R using (C.6).

The damage d_i for one cycle of stress range S_i is

$$d_i = \frac{1}{N_i} \tag{C.10}$$

The total damage for the actual number of cycles n_i is

$$D_i = \frac{n_i}{N_i} \tag{C.11}$$

The total damage from all bins (i.e. the entire signal) is

$$D = \sum D_i = \frac{1}{S_0^m} \sum n_i S_i^m \tag{C.12}$$

The timeseries typically has a duration of t=10 min. The bin values $n_{i,t}$ must then be linear extrapolated to the equivalent lifetime values T before using (C.12).

$$n_i = T\frac{n_{i,t}}{t} = Tn_i' \tag{C.13}$$

The material will fail if $D \geq 1$. Although, in practice $D \geq 0.7\text{-}3.0$.

It is useful to define an equivalent stress amplitude S_{eq}, which under n_{eq} cycles will cause the same fatigue damage. I.e.

$$D = n_{eq}\frac{S_{eq}^m}{S_0^m} \tag{C.14}$$

n_{eq} can be selected arbitrary. One possibility is to let it correspond to an equivalent frequency f_{eq} (e.g. 1 Hz) in the component lifetime

$$n_{eq} = f_{eq} T \tag{C.15}$$

The specific definition of n_{eq} is often complicating things unnecessary making it harder to interpret results. This can be overcome by not using it at all and instead use only the equivalent frequency f_{eq}, from which the entire analysis can be made. Since D is given by (C.12) the correct equivalent stress can be found

$$S_{eq} = \left(\frac{\sum n_i S_i^m}{n_{eq}}\right)^{1/m} = \left(\frac{\sum n_i' S_i^m}{f_{eq}}\right)^{1/m} \tag{C.16}$$

S_{eq} is independent of T and n_i' are under quasi steady conditions independent of t, so S_{eq} does not depend on sampling time or total lifetime (in practice there will often be variations with sampling time depending on the signal).

An equivalent *load* can also be defined

$$R_{eq} = \frac{S_{eq}}{k} = \left(\frac{\sum n_i R_i^m}{n_{eq}}\right)^{1/m} = \left(\frac{\sum n_i' R_i^m}{f_{eq}}\right)^{1/m} \tag{C.17}$$

The damage is

$$D = n_{eq} \frac{k^m R_{eq}^m}{S_0^m} = f_{eq} T \frac{k^m R_{eq}^m}{S_0^m} \tag{C.18}$$

The equivalent load has the advantage that it can be calculated using only a load history and 1 material constant, m. A meaningful relative comparison of the damage from various timeseries is made by comparing R_{eq}^m calculated using the same f_{eq}.

C.4 Several timeseries

In case of several timeseries the total damage is found by summation

$$D = \sum_j D_j = \sum_j \sum_i D_{ij} = \sum_j \frac{1}{S_0^m} \sum_i n_{ij} S_{ij}^m \tag{C.19}$$

where j is the index of timeseries. When referring to the previous section a subscript j should therefore be added to the notation there. The rainflow counted values $n_{ij,t}$ must again be extrapolated to their lifetime values where T_j is the actual lifetime of timeseries j.

$$n_{ij} = T_j \frac{n_{ij,t}}{t_j} = T_j n'_{ij} \tag{C.20}$$

T_j is now defined as a fraction of the total lifetime T

$$T_j = f_j T \tag{C.21}$$

Where f_j is the proportion of the lifetime represented by timeseries j. n_{eq} is defined as before

$$n_{eq} = T f_{eq} \tag{C.22}$$

It is again usefull to define an equivalent stress S_{eq} of the same form form as in equation (C.14). Comparing (C.14) with (C.19) the correct value is found

$$S_{eq} = \left(\frac{\sum_j \sum_i n_{ij} S_{ij}^m}{n_{eq}} \right)^{1/m} = \left(\sum_j f_j \frac{\sum_i n'_{ij} S_{ij}^m}{f_{eq}} \right)^{1/m} \tag{C.23}$$

Assuming the same f_{eq}, this can be written in terms of $S_{eq,j}$ found for the individual timeseries using (C.16).

$$S_{eq} = \left(\sum_j f_j S_{eq,j}^m \right)^{1/m} \tag{C.24}$$

Where $S_{eq,j}$ could be determined independent of sampling time and lifetime. In terms of equivalent loads the relations are

$$R_{eq} = \left(\frac{\sum_j \sum_i n_{ij} R_{ij}^m}{n_{eq}} \right)^{1/m} = \left(\sum_j f_j \frac{\sum_i n'_{ij} R_{ij}^m}{f_{eq}} \right)^{1/m} = \left(\sum_j f_j R_{eq,j}^m \right)^{1/m} \tag{C.25}$$

The total damage is

$$D = f_{eq} T \frac{k^m R_{eq}^m}{S_0^m} \tag{C.26}$$

C.5 Formulas on integral form

The binned formulation is not useful for analytical analysis, and a more general formulation is presented below.

The range of stress is described by a function $S(x)$, and the number of cycles is a distribution function $n(x)$. x is a general variable and can for instance be the stress itself ($x{=}S$, $S(x){=}S$, $n(x){=}n(S)$, $dx{=}dS$). The number of cycles from x to $x{+}dx$ is

$$dn' = \frac{n(x)}{T}\,dx = n'(x)\,dx \tag{C.27}$$

Values of n' can be approximated from a binned RFC as

$$n'(x_i) = \frac{n_i(x_i)}{t\Delta x_i} \tag{C.28}$$

Where Δx_i is the width of the bin. The summation transforms into an integral

$$\sum n_i' S_i^m \Rightarrow \int n'(x)S(x)^m\,dx \tag{C.29}$$

and the damage in unit time is

$$D' = \frac{1}{S_0^m}\int n'(x)S(x)^m\,dx \tag{C.30}$$

Assume the distributions them self are distributed, e.g. as a function of wind speed v

$$n' = n'(x,v) \quad S = S(x,v) \tag{C.31}$$

The damage then becomes a function of v and the damage in time dt is

$$dD = D'(v)dt \tag{C.32}$$

Where $dt(v)$ is the infinitesimal time at v during the whole lifetime T. $dt(v)$ is found from the wind speed probability function $f(v)$ and the total lifetime T

$$dt = Tf(v)dv \tag{C.33}$$

The damage in time T is found by integrating (C.32)

$$D = \frac{T}{S_0^m}\int f(v)\int n'(x,v)S(x,v)^m\,dx\,dv \tag{C.34}$$

This can also be written using the discrete form in equation (C.29)

$$D = \frac{T}{S_0^m}\int f(v)\sum n_i'(v)S_i(v)^m\,dv \tag{C.35}$$

or as

$$D = \frac{1}{S_0^m} \sum T_j \int n_j'(x) S_j(x)^m \, dx \tag{C.36}$$

The definitions of the equivalent stress are

$$S_{eq} = \left[\frac{1}{f_{eq}} \int f(v) \int n'(x,v) S(x,v)^m \, dx \, dv \right]^{1/m} \tag{C.37}$$

and

$$S_{eq} = \left[\frac{1}{f_{eq}} \int f(v) \sum n_i'(v) S_i(v)^m \, dv \right]^{1/m} \tag{C.38}$$

and

$$S_{eq} = \left[\frac{1}{f_{eq}} \sum f_j \int n_j'(x) S_j(x)^m \, dx \right]^{1/m} \tag{C.39}$$

WIND ENERGY
Wind Energ. 2010; **13**:373–389

RESEARCH ARTICLE

Validation and modification of the Blade Element Momentum theory based on comparisons with actuator disc simulations

Helge Aa. Madsen[1], Christian Bak[1], Mads Døssing[1], Robert Mikkelsen[2] and Stig Øye[2]

[1] Division of Wind Energy, Risø National Laboratory for Sustainable Energy, Technical University of Denmark, PO 49, DK-4000 Roskilde, Denmark
[2] Department of Mechanical Engineering, Technical University of Denmark, Niels Koppels Allé, Building 403, DK 2800, Kgs. Lyngby, Denmark

ABSTRACT

A comprehensive investigation of the Blade Element Momentum (BEM) model using detailed numerical simulations with an axis symmetric actuator disc (AD) model has been carried out. The present implementation of the BEM model is in a version where exactly the same input in the form of non-dimensional axial and tangential load coefficients can be used for the BEM model as for the numerical AD model. At a rotor disc loading corresponding to maximum power coefficient, we found close correlation between the AD and BEM model as concerns the integral value of the power coefficient. However, locally along the blade radius, we found considerable deviations with the general tendency, that the BEM model underestimates the power coefficient on the inboard part of the rotor and overestimates the coefficient on the outboard part. A closer investigation of the deviations showed that underestimation of the power coefficient on the inboard part could be ascribed to the pressure variation in the rotating wake not taken into account in the BEM model. We further found that the overestimation of the power coefficient on the outboard part of the rotor is due to the expansion of the flow causing a non-uniform induction although the loading is uniform. Based on the findings we derived two small engineering sub-models to be included in the BEM model to account for the physical mechanisms causing the deviations. Finally, the influence of using the corrected BEM model, BEM_{cor} on two rotor designs is presented. Copyright © 2009 John Wiley & Sons, Ltd.

KEYWORDS
rotor aerodynamics; BEM theory; induction; swirl; wake expansion; actuator disc model; wind turbine; energy conversion

Correspondence
Helge Aa. Madsen, Research Specialist, Programme of Aeroelastic Design, Wind Energy Division, Risø DTU, Denmark.
E-mail: hama@risoe.dtu.dk

Received 22 December 2008; Revised 5 June 2009; Accepted 29 June 2009

NOTATIONS

a	axial induction factor
a_{cor1}	axial induction factor after correction for wake rotation
$a`$	tangential induction factor
c	chord length (m)
C_d	drag coefficient
C_l	lift coefficient
$C_{P_{av}}$	average power coefficient
C_{p_a}	power coefficient for axial loading
C_{p_s}	power coefficient based on shaft power
C_{P_t}	power coefficient for tangential loading
$C_{P_{tot}}$	power coefficient for total energy conversion at rotor disc
C_Q	local torque coefficient—tangential loading on actuator disc
C_T	local thrust coefficient—axial loading on actuator disc
C_x	projection of lift and drag coefficients on tangential direction
C_y	projection of lift and drag coefficients on axial direction

$k_1 k_2 k_3$	constants in polynomial for $a(C_T)$
$k1, k2, k3$	constants of polynomial trend lines for wake expansion
$k_{massflow}$	mass flow factor—ratio between total mass flow in the standard BEM model and total mass flow in the corrected BEM$_{cor}$ model
dQ	torque on differential annular element dr
dT	thrust on differential annular element dr
N_B	number of blades
p	pressure
p_w	pressure from rotation of wake flow (swirl)
r	radial position
R	rotor radius (m)
X_a	volume force in axial direction
v_a	axial velocity
v_{a-cor}	final corrected axial velocity
v_{a-cor1}	axial velocity corrected for rotation of wake
v_r	radial velocity
v_t	tangential velocity
V_r	length of relative velocity vector
V_0	free stream velocity (m s)

GREEK LETTERS

λ	tip speed ratio
λ_r	local tip speed ratio
Δp_w	pressure component from wake rotation computed with the AD model
Δv_e	axial correction velocity from wake expansion
$\Delta v1_e$	variable term of axial correction velocity from wake expansion
$\Delta v2_e$	constant term of axial correction velocity from wake expansion
Δv_w	correction velocity from wake rotation
ϕ	angle from rotor plane to relative velocity vector
ρ	mass density (kg m^{-3})
Ω	angular rotor shaft velocity (rad s^{-1})

1. INTRODUCTION

It is well known that the blade element momentum (BEM) model, being the most common engineering model for computation of aerodynamic forces in aerodynamic and aeroelastic design models, is derived on basis of a number of assumptions for the flow properties through the rotor and in the wake. The BEM model has originally been developed by Glauert[1] who also discusses the assumptions that must be introduced in order to derive the simple relations for axial and tangential induction. One of these assumptions is to disregard the pressure term from rotation of the wake. This assumption has later been considered by e.g. Wilson and Lissaman[2] and de Vries[3] made a more detailed analytical study of the consequences of this assumption. From his study, the influence of making different assumptions about wake expansion and about the pressure term from wake rotation is shown in Figure 1. Including the pressure term from wake rotation and at the same time including the wake expansion, de Vries showed that the power loss from wake rotation at low tip speed ratio is almost cancelled by the increased mass flow through the rotor because of the low pressure in the centre of the wake from wake rotation. This is, thus, different from the theory of Glauert, where only the loss from the wake rotation is included, and this leads to the decrease in rotor power coefficient at low tip speed ratio as shown by the dashed line in Figure 1. However, the analysis was carried out for a constant bound circulation along the blade span and cannot just be expanded for use on arbitrary loadings on the rotor. Later, Sharp[4] made a similar study and he also came to the conclusion that the rotor power coefficient does not decrease at low tip speed ratio but can even exceed the Lanchester-Betz limit, and the same was concluded by Xiros.[5] One of the limitations in the study of both de Vries and Sharp is the assumption of a constant circulation along the blade span and of a constant axial velocity distribution at the rotor disc. Lam[6] worked a little further on the analysis of Sharp and showed one more possible solution for the maximum C_P based on the same C_P equation as sharp. This other theoretical solution means zero induction at the rotor disc and an induction of 1 in the far field corresponding to infinite expansion. One of the complications in above mentioned studies is that the constant circulation in combination with the wake swirl results in a singularity at the turbine axis where the tangential flow velocity becomes infinite. Introducing a hub vortex in his model Wood[7] tries to overcome this by introducing a hub vortex and comes to the same qualitative trend of an increasing power coefficient as function of a decreasing tip speed ratio as found by Sharp, however now with a model that differs from the one used by Sharp.

Besides disregarding the pressure term from wake rotation, there are other assumptions behind the simple set of equations used for computation of the induction and of the aerodynamic forces in the BEM model. The most uncertain point might be that the equations are derived using the momentum equation on integral form, but at the end the induction, equations are used on differential form where the stream tubes are assumed to be independent of each other (also called strip theory). This has big advantages in solving the equations and it also gives a robust model, which is desirable when using the BEM model together with numerical optimization for rotor design.

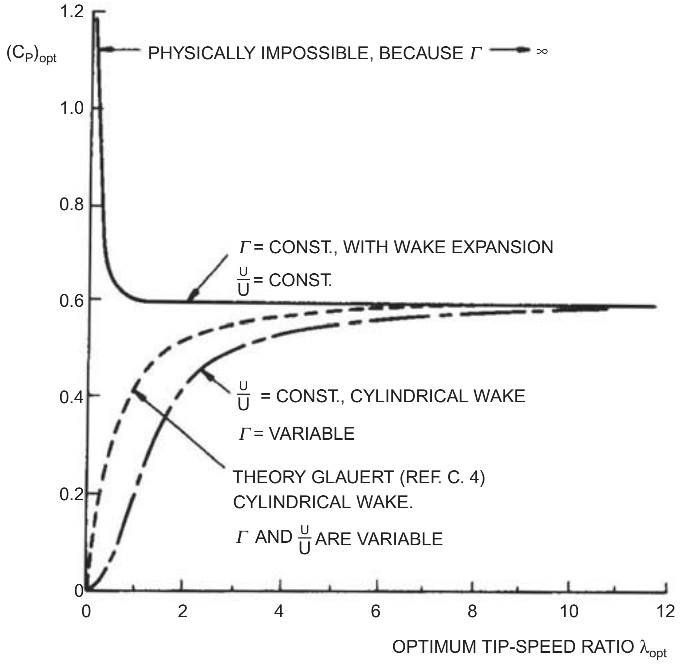

Figure 1. The influence on the power coefficient vs. tip speed ratio, from different assumptions on wake expansion and induction characteristics from the study of de Vries.[3] Figure reproduced from de Vries[3].

However, it is uncertain how good this assumption is, and in particular, when the loading on the rotor is varying considerably in radial direction as is the case in the root and tip region.

In order to validate the BEM model and investigate the influence of the assumptions behind the simplified set of equations describing the flow through the rotor we have carried out a thorough comparison with numerical results from an actuator disc (AD) model.[8–13] The major difference between the BEM model and the AD model is that the full set of equations are solved in the AD model using a computational fluid dynamics (CFD) code, which, in the present case, is the commercial code FIDAP.[14] A comparison of the results from the two models will thus reveal the importance of the assumptions behind the simplified set of equations in the BEM model.

The organization of the paper is the following. First, there is a description of the AD model and the BEM model. Then, a section with comparisons of results from the two models follows. On the basis of this comparison, we then present two sub-models to be included in the BEM model in order to model the influence of the pressure term from wake rotation and the influence on the induction from wake expansion. These sub-models are not limited to specific load distribution or limited tip speed ratio range and the resulting modified BEM model can thus be used for design and analysis work in industry. At the end of the paper the influence of using the modified BEM model is shown for two rotor designs.

2. ACTUATOR DISC MODEL COMPUTATIONS

The loading on the actuator disc C_y, C_x is derived from the lift and drag projections normal and tangential to the rotor plane:

$$\begin{aligned} C_y &= C_l\cos(\phi) + C_d\sin(\phi) \\ C_x &= C_l\sin(\phi) - C_d\cos(\phi) \end{aligned} \tag{1}$$

where ϕ is the angle from the rotor plane to the relative velocity vector, Figure 2.

The infinitesimal thrust dT and torque dQ on an infinitesimal annular element dr can be written as

$$\begin{aligned} dT &= \frac{1}{2}\rho V_r^2 C_y c N_B dr \\ dQ &= \frac{1}{2}\rho V_r^2 C_x c N_B r dr \end{aligned} \tag{2}$$

Wind Energ. 2010; **13**:373–389 © 2009 John Wiley & Sons, Ltd.
DOI: 10.1002/we

where V_r is the relative velocity to the blade section, ρ is density of mass, c is chord length and N_B is number of blades.

We then derive the local thrust coefficient C_T and the local torque coefficient C_Q:

$$C_T = \frac{dT}{\frac{1}{2}\rho V_0^2 2\pi r dr} = \frac{V_r^2 C_y c N_B}{V_0^2 2\pi r}$$
$$C_Q = \frac{dQ}{\frac{1}{2}\rho V_0^2 r 2\pi r dr} = \frac{V_r^2 C_x c N_B}{V_0^2 2\pi r} \tag{3}$$

where V_0 is the free stream velocity.

For the energy conversion in inviscid flow ($C_d = 0$), we can derive the ratio between C_T and C_Q as follows:

$$\frac{C_Q}{C_T} = \frac{\frac{dQ}{r}}{dT} = \frac{C_x}{C_y} = \tan(\phi) \Rightarrow C_Q = C_T \tan(\phi) \tag{4}$$

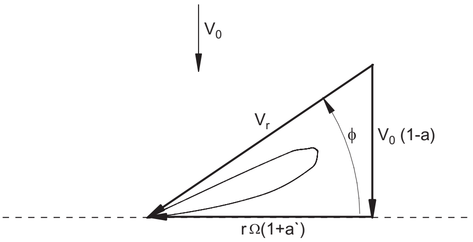

Figure 2. The velocity triangle at the airfoil section.

This equation shows that if we specify a rotor loading by C_T, then we shall apply a corresponding loading C_Q as given by equation (4). However, as C_Q depends on the actual flow angle ϕ, which is a part of the flow solution, an iteration loop is necessary in order to reach a final solution for a specified axial loading C_T. We can now study the energy conversion in a rotor simply by specifying the loading expressed by C_T and C_Q.

2.1. Mesh and computational conditions

The general purpose CFD code FIDAP was used for the present computations. In the past the code has been used for several studies using the actuator disc model. The previous studies comprised: comparison with the BEM model, influence of turbulent mixing and high loading,[15] aerodynamics of coned rotors,[16] yawed flow aerodynamics,[17,18] and dynamic induction.[19] Based on experience from these studies the set-up for the present simulations was chosen. Axisymmetric, swirling flow has been assumed and a mesh stretching 10R in upstream and radial direction and 20R in downstream direction has been used. The disc itself is modelled with two layers of elements in the stream-wise direction and has a extension of 0.05R (Figure 3). Further, the simulations were run for laminar flow with a Reynolds number of 1000 based on rotor radius.

3. THE BEM MODEL COMPUTATIONS

The present implementation form of the BEM model has been chosen because it makes it possible to use induction

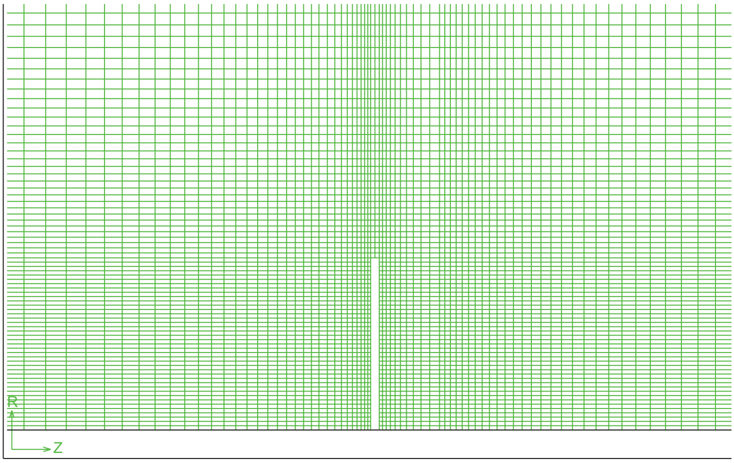

Figure 3. Detailed view on the mesh close to the actuator disc. The disc is modelled with two elements in the streamwise direction and has a total width of 0.05R. The dimensions of the total mesh are: 10R upstream, 10R radial and 20R in the downstream direction.

characteristics from a more detailed numerical model in simulation cases where the standard BEM model fails. This can, for example, be coned rotors, rotors with high blade deflections or rotors with winglets on the blades. The present implementation has further the advantage that the input to the model are exactly the same two load coefficients C_T, C_Q as used as input for the AD model and this means that the two models easily can be compared.

Momentum theory relates the induction a to the axial thrust coefficient C_T by:

$$C_T = 4a(1-a) \tag{5}$$

For angular momentum, we have, for an annular element:

$$dQ = \rho(2\pi r dr) r V_0 (1-a)(2ra`\Omega) \tag{6}$$

and the torque dQ is derived as:

$$dQ = \frac{1}{2}\rho V_r^2 r C_x c N_B dr \tag{7}$$

Combining equations (6) and (7) and introducing the tangential load coefficient C_Q defined in equation (3), we get:

$$a` = C_Q \frac{V_0}{4r(1-a)\Omega} = C_Q \frac{1}{4(1-a)\lambda_r} \tag{8}$$

with $\lambda_r = \dfrac{r\Omega}{V_0}$ inserted

The tangential velocity is computed as:

$$a` = C_Q \frac{V_0}{4r(1-a)\Omega} \Rightarrow 2ra`\Omega = v_t = \frac{V_0 C_Q}{2(1-a)} \tag{9}$$

The flow through the disc as function of the load coefficients C_T, C_Q can now be found by equations (5) and (9). For the solution of equation (5), we express the induction as function of C_T using a third order polynomial:

$$a = k_3 C_T^3 + k_2 C_T^2 + k_1 C_T \tag{10}$$

The constants have been found so that equation (5) is fulfilled for loadings C_T up to 0.7–0.8, but ensuring that we have a smooth transition to an empirical relation at higher loadings where equation (5) is not valid. At high loadings, we have based the shape of the curve on several different inputs; the Glauert empirical relation and AD simulations at high loadings.[14] The following values for the constants have been used: $k_3 = 0.08921$, $k_2 = 0.05450$, $k_1 = 0.25116$.

Now, there can be rotor designs such as coned rotors, where the $a(C_T)$ relation as given by equation (10) does not hold. Axial velocity contours for a rotor with a coning of 20º, computed with the AD model, is shown in Figure 4. Induction at different radial positions on the disc as function of local loading for this simulation have been extracted and plotted in Figure 5. It is seen that the curves do not follow the standard Glauert relation. On a major part of the rotor, the $a(C_T)$ slope is less than the Glauert relation, and only close to the tip the induction is stronger. With the present implementation of the BEM model, these

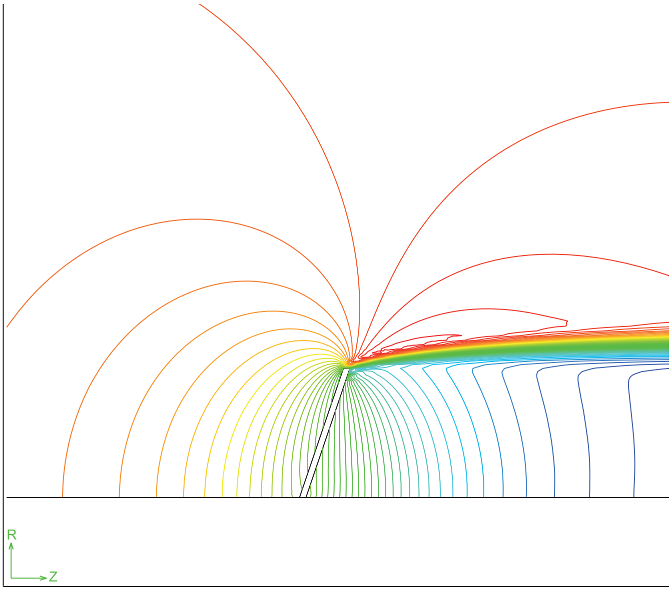

Figure 4. Axial velocity contours for an AD simulation on a 20° coned rotor with a constant loading and $C_T = 0.89$.

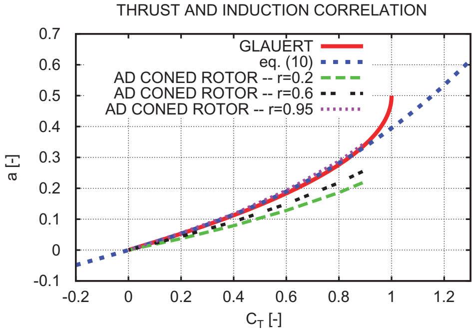

Figure 5. The relation between loading C_T and induction factor as used in the present formulation of the BEM code and compared with the Glauert correlation. Further, the computed correlation for a coned rotor at different radial stations is shown.

$a(C_T)$ relations as function of radius can now be used instead of the standard Glauert relation, and we get a much more accurate simulation with the BEM model. More results on the induction characteristics for coned rotors and rotors with deflected blades can be found in Madsen[16] and Mikkelsen.[20]

4. POWER CONVERSION COEFFICIENTS

The power conversion in the actuator disc over an annular element is, according to de Vries[3]:

$$dP = \Omega dQ = v_a dT - \frac{1}{2}\frac{v_t}{r}dQ \tag{11}$$

We now derive non-dimensional power coefficients for the individual terms in equation (11).

For the total energy conversion, we have

$$C_{P_{tot}} = \frac{dP}{\frac{1}{2}\rho V_0^3 2\pi r dr} \tag{12}$$

and for the shaft power

$$C_{P_s} = \frac{\Omega dQ}{\frac{1}{2}\rho V_0^3 2\pi r dr} = \frac{r\Omega}{V_0}C_Q = C_Q\lambda_r \tag{13}$$

where λ_r is the local tip speed ratio.

For the energy conversion by the axial volume forces, we have

$$C_{P_a} = \frac{v_a dT}{\frac{1}{2}\rho V_0^3 2\pi r dr} = \frac{v_a C_T}{V_0} \tag{14}$$

and for the tangential volume forces, combining equations (2) and (11)

$$C_{P_t} = \frac{\frac{1}{2}\frac{v_t}{r}dQ}{\frac{1}{2}\rho V_0^3 2\pi r dr} = \frac{\frac{1}{2}\frac{v_t}{r}}{\frac{1}{2}\rho V_0^3 2\pi r dr}\frac{1}{2}\rho V_r^2 C_x c N_B r dr \tag{15}$$

Inserting C_Q from equation (3) and combining with equation (9), we get

$$C_{P_t} = \frac{1}{2}v_t\frac{C_Q}{V_0} = \frac{1}{2}\frac{v_t}{V_0}\frac{v_t 2(1-a)}{V_0} = \frac{v_t^2(1-a)}{V_0^2} \tag{16}$$

For the non-dimensional power coefficients, we now have the same relation as for the power balance shown in equation (11)

$$C_{P_{tot}} = C_{P_s} = C_{P_a} - C_{P_t} \tag{17}$$

It should be noted that in the following, all variables are non-dimensionalized as follows:

$$v^* = v/V_0, r^* = r/R, p^* = p/(\rho V_0^2), \lambda = \frac{\Omega R}{V_0}, \lambda_r = \frac{\Omega r}{V_0} \tag{18}$$

However, for simplification the star is not written.

The non-dimensionalization reduces the expression for the power coefficients to

$$C_{P_a} = v_a C_T \tag{19}$$

and

$$C_{P_t} = v_a v_t^2 \tag{20}$$

5. COMPARISON OF BEM AND AD RESULTS

A number of different load distributions have been used in the numerical study on which the present results are based. Here, the results will first be shown for a tip speed ratio of 6 and a constant loading of $C_T = 0.95$, which, however, decreases linearly to zero at the rotor centre in order to avoid a tangential loading increasing to infinity (Figure 6).

The comparison of the axial and tangential velocities at the rotor disc (Figure 7) shows that the induction computed by the AD model is less than the induction by the BEM model on the inner part of the rotor, whereas the opposite tendency is seen on the outer part of the rotor. It should be noted that exactly the same loading has been used in the two models, as the tangential loading only was found by the AD model using a few iterations to find the tangential loading for the converged solution.

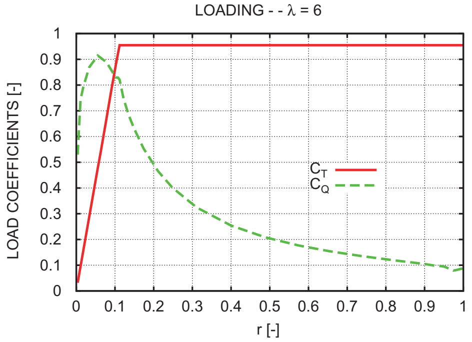

Figure 6. A constant thrust coefficient $C_T = 0.95$ (except close to the rotor centre) as function of radius and the corresponding tangential loading for inviscid flow (airfoil $C_d = 0.0$) at a tip speed ratio of 6. C_Q from the converged AD solution.

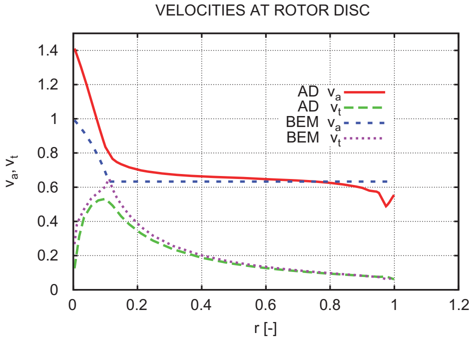

Figure 7. The axial and tangential velocities at the rotor disc, computed with the AD and BEM models, respectively, using the loading shown in Figure 6.

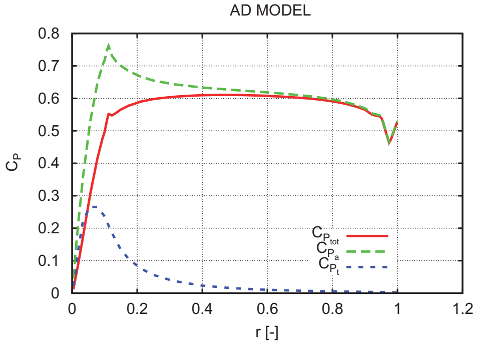

Figure 8. The power coefficients as defined by equations (12), (14) and (16), computed with the AD model.

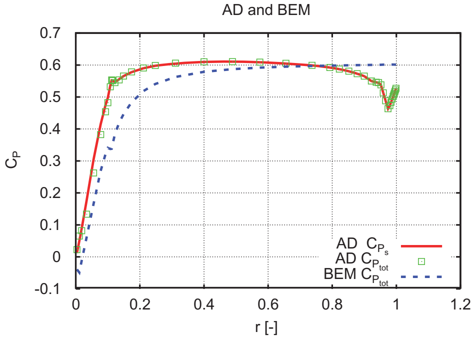

Figure 9. Comparison of the local power coefficients computed by the AD model and the BEM model, respectively.

In Figure 8, it appears that the power coefficient for the axial loading can exceed the Betz limit considerably, as its maximum is around 0.75 at a radial position of 0.1. However, it is also at this radial position that the power coefficient for the tangential loading has its maximum, and this represent power supplied to the flow in the form of wake flow rotation. The total power coefficient being derived as the difference between the two mentioned coefficients decreases only slightly inboard and this confirms the findings of de Vries[3] and Sharp,[4] who found that the losses due to wake rotation would be counterbalanced because of the increased axial flow on the inner part of the rotor.

The differences in flow velocities comparing the AD and the BEM model respectively, leads to considerable deviations in the local C_P coefficients as seen in Figure 9. On the inboard part of the rotor, the C_P coefficient computed by the AD model is considerably higher than the C_P from the BEM model, and is seen to exceed the Betz limit of 0.59 on part of the rotor. It should also be noted that the shaft power C_P and the total $C_{P_{tot}}$ derived from the power conversion in the fluid, as shown by equation (17), coincide completely as they should do.

In order to see the integrated effect of the deviations, the local average $C_{P_{av}}$ (this coefficient is the average power coefficient over the rotor area from rotor centre to the actual radial position) for the two models is shown in Figure 10. On almost the whole rotor, the BEM model underestimates the power coefficient, but at the rotor edge, the curves coincide showing that, in average, over the whole rotor area, the two models give almost the same power coefficient.

The example shown here is representative for a big number of comparisons performed as background for the paper although the deviations decrease for decreasing loading. In the following sections, the causes of the deviations will be discussed as well as derivation of two sub-models to the BEM model to account for the deviations.

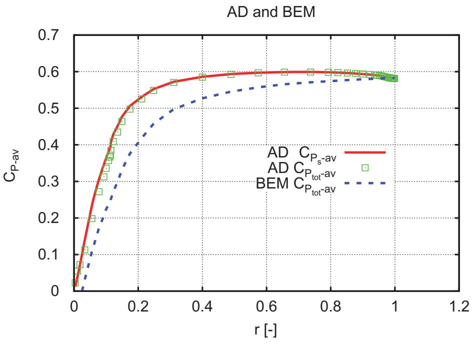

Figure 10. The local, average $C_{P\text{–}av}$ coefficient derived from the distributions shown in Figure 6 (the average C_P from the rotor centre and to the actual radial position).

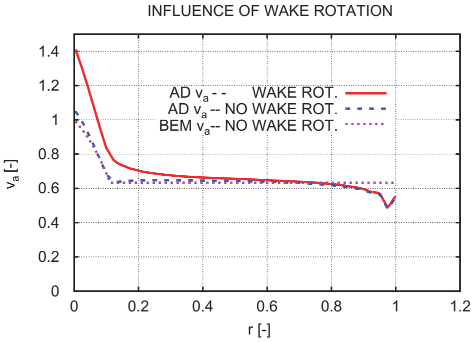

Figure 11. The axial velocity at the rotor from the AD model computed with and without tangential loading, respectively. BEM results for the same axial loading.

6. MODEL FOR SIMULATION OF THE INFLUENCE OF THE PRESSURE VARIATION FROM WAKE ROTATION

To illustrate the cause of the deviations on the inboard part of the rotor, the AD model was run with and without the tangential loading but with the same axial loading in the two cases. The axial loading was the same as shown in Figure 6 with C_T equal to 0.95.

Excluding the tangential loading in the AD simulations results in an axial velocity profile at the rotor disc correlating very well with the BEM results except on the outboard part of the rotor (Figure 11). However, for the case with tangential loading, and thus with wake rotation, the induction in the AD results is much less on the inboard part of the rotor. The difference is due to the pressure component caused by the wake rotation as shown in Figure 12. Towards the rotor centre, the decrease in pressure is seen to be considerable. The shortcoming in the standard BEM model is thus that the balance between external, axial loading and the change of axial momentum is not correct because of the influence on axial momentum from the wake rotation pressure component.

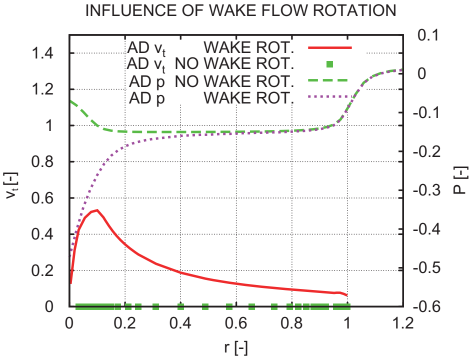

Figure 12. The pressure distribution behind the rotor as function of radial position for the same case as shown in Figure 11.

The mechanism behind the increased axial velocity due to wake rotation is thus simple, and the same is the proposed sub-model to simulate this. The sub-model contains three steps:

- compute the radial pressure variation at the rotor disc from the induced tangential velocity distribution
- derive the axial velocity component corresponding to this pressure variation and add it to the local velocity at the disc
- compute an updated tangential velocity corresponding to the new a using equation (8)
- repeat the loop with the new tangential velocity and continue until convergence

The non-dimensional pressure term from the wake rotation is computed as:

$$p_w = \int_1^r \frac{v_t^2}{r} dr \tag{21}$$

where $v_t = 2a`\lambda_r$ is the tangential velocity computed in the BEM model.

The pressure component from wake rotation Δp_w computed with the AD model and derived as the difference in pressure with tangential loading and without, respectively, is shown in Figure 13 at four positions just behind the rotor disc and compared with the pressure p_w computed with the sub model (equation (21)). The suction computed by the AD model is seen to reach its lowest value at a position y = 0.3 downstream the disc, but does not completely reach the value of p_w computed on basis of the BEM wake rotation. This is probably due to the viscous effects in the AD due to the strong velocity gradients (the tangential velocity is discontinuous across the disc). At the rotor disc, the AD model pressure correlates best with $0.7p_w$, as shown in Figure 13.

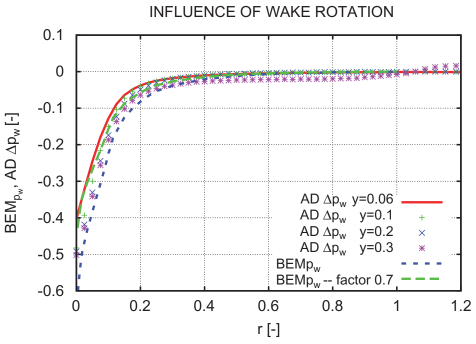

Figure 13. Comparison of the radial pressure distribution from wake rotation behind the rotor disc computed with the AD model and compared with the pressure derived from the BEM wake rotation.

We now assume that we can derive the axial velocity component related to this pressure from wake rotation from the following equation (linearized Euler equation):

$$\frac{\partial v_w}{\partial y} = -\frac{\partial p_w}{\partial y} \tag{22}$$

Integrating this equation, the velocity correction term Δv_w is seen to be equal to p_w. For the velocity correction term from the wake rotation, we thus get:

$$\Delta v_w = 0.7 p_w \tag{23}$$

The corrected axial velocity v_{a-cor1} through the rotor disc can now be computed as:

$$v_{a-cor1} = (1-a) + \Delta v_w \tag{24}$$

and the corresponding axial induction factor is:

$$a_{cor1} = (1 - v_{a-cor1}) \tag{25}$$

We now also update the tangential induction factor to correspond to the new axial induction factor using equation (8):

$$a`_{cor1} = C_Q \frac{1}{4(1-a_{cor1})\lambda_r} \tag{26}$$

When comparing the velocity profiles at the rotor disc, including this additional velocity term from wake rotation, an excellent correlation with the AD model is observed on the inboard part of the rotor (Figure 14). On the outboard part, there is still a deviation that will be discussed in the next section. It is also seen that the tangential velocity profile computed with the corrected BEM now correlates better with the AD model results because of the more accurate mass flow through the disc.

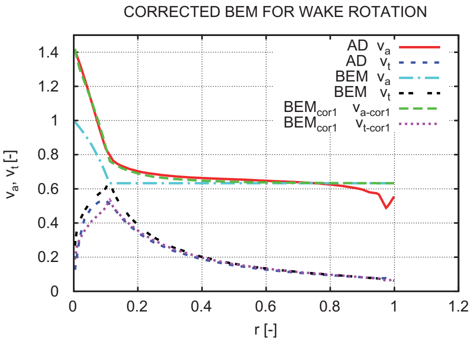

Figure 14. The effect of the correction of the BEM model to include an additional velocity term from the wake pressure because of wake rotation.

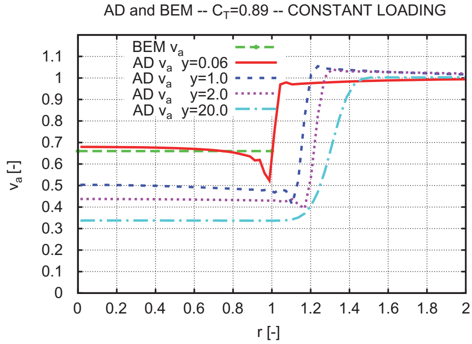

Figure 15. Axial velocity profiles at several down-stream positions from the rotor, computed with the AD model for constant loading and no tangential loading.

7. MODEL FOR SIMULATION OF THE DECREASED INFLOW AT THE TIP REGION DUE TO WAKE EXPANSION

The other characteristic deviation when comparing the BEM model with AD results is the reduced inflow at the tip region which is not modelled by the BEM model. This is illustrated in Figure 15, where the axial velocity profiles computed by the AD model for a constant axial loading with C_T = 0.89 and no tangential loading C_Q = 0.0 are shown. The BEM model gives a constant induction, whereas the AD model shows a decreasing velocity (bigger induction) at the tip region, but with the opposite tendency towards the rotor centre. However just 1 diameter downstream, the velocity profile is more uniform, and far downstream, it has become completely uniform. The corresponding radial velocity profiles shown in Figure 16 are a good measure of the rate of expansion and show

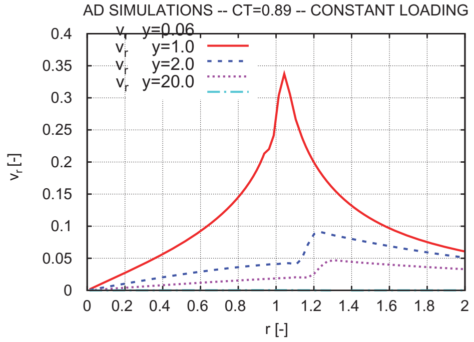

Figure 16. Radial velocity profiles at the same positions as the axial velocity profiles in Figure 15.

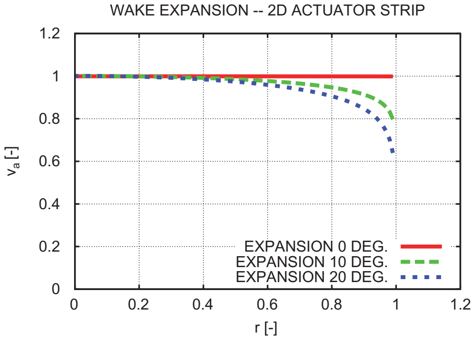

Figure 18. The velocity distribution at the rotor disc for the vortex system shown in Figure 17 for different wake expansion angles. Note the absolute level of the distributions were adjusted to 1 at the centre.

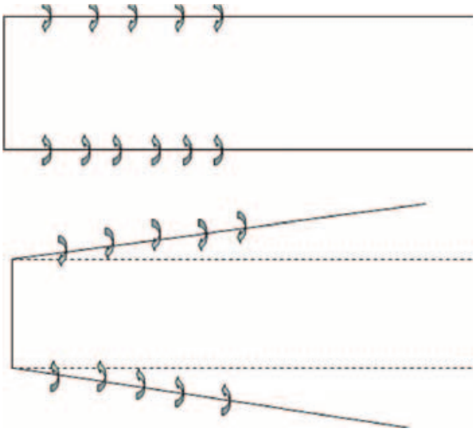

Figure 17. A simple 2D fixed wake model to illustrate the influence of wake expansion. Velocity distributions at the rotor disc found by numerical integration of the describing equations.

clearly the big difference in rate of expansion at the rotor disc compared to the conditions further downstream. The reduced inflow at the tip is a general characteristic of the results from non-linear flow models as, e.g. the results of actuator disc simulations presented by Sørensen.[21]

The above results indicate that the reduced inflow at the tip region are due to the rate of wake expansion, which causes the streamlines at the rotor disc to be in an angle different to ninety degrees to the rotor disc.

A simple 2D vortex model for a constant loaded actuator strip is used to illustrate the influence of the angle of the vortex paths (assumed to follow the streamlines) to the rotor disc, Figure 17. The total axial induction at the disc has been computed by numerical integration of the induction from the constant strength vortex elements distributed along the lines passing through the edges of the disc. When the vortex system lies on a path perpendicular to the disc we get a uniform induction over the disc but when they are in an angle different from ninety degrees we get a reduced inflow (increased induction) towards the edges of the actuator strip (Figure 18). This simple 2D model illustrates the mechanism behind the reduced inflow in the tip region but more detailed, quantitative insight can be obtained using an axisymmetric vortex model of a rotor as presented by Øye.[22]

The proposed sub-model to be included in the BEM model to account for the reduced inflow in the tip region from wake expansion is therefore based on the assumption of a close relation between the reduced inflow Δv_e and the radial velocity distribution v_r. During the process of deriving this correlation, it was found convenient to split the velocity deviation Δv_e in two parts, $\Delta v1_e$ varying along the radius and a constant term $\Delta v2_e$. $\Delta v1_e$ was derived as the difference between the BEM and the AD velocity profiles for radial positions greater than 0.3 and the $\Delta v1_e$ term was adjusted to 0 at the starting point (Figure 19). The other term $\Delta v2_e$ was assumed to be constant over the whole rotor, but still linked to the radial velocity but now just at one radial position.

The correlation between $\Delta v1_e$ and v_r, shown in Figures 19 and 20, at different radial stations, was now determined and approximated with third-order polynomial trend lines. The variation of the factors in each of these polynomials was then derived as function of radius with the following result:

$$k3 = -15.83r + 20.73 \tag{27}$$

$$k2 = -0.52r - 0.90 \tag{28}$$

$$k1 = 1.58r^2 - 1.63r + 0.51 \tag{29}$$

The correction velocity $\Delta v1_e$ can now be found as:

$$\Delta v1_e = k3v_r^3 + k2v_r^2 + k1v_r \tag{30}$$

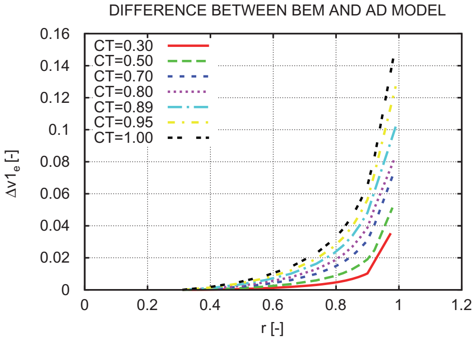

Figure 19. Difference in axial velocity at the rotor disc computed with the BEM and the AD model, respectively. Constant loading and no tangential loading.

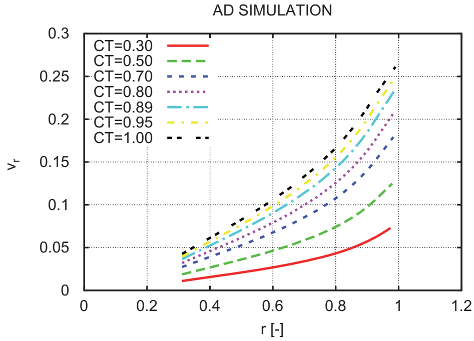

Figure 20. Radial velocity as function of radial position computed with the AD model for different, constant loadings and no tangential loading.

The other constant term $\Delta v2_e$ was computed as the difference between the BEM and AD velocities at radius 0.3, and this term was correlated to the radial velocity at radius 0.9. The following correlations were derived:
Interval $0.05 \le v_{r09} < 0.15$:

$$\Delta v2_e = 1.0361 v_{r09}^2 - 0.0961 v_{r09} + 0.00003 \tag{31}$$

Interval $0.15 \le v_{r09} < 0.20$:

$$\Delta v2_e = -2.3894 v_{r09}^2 + 0.9642 v_{r09} - 0.0817 \tag{32}$$

For $v_{r09} < 0.05$, equation (31) was used with $v_{r09} = 0.05$, and for $v_{r09} \ge 0.2$, equation (32) was used with $v_{r09} = 0.20$

The final term for modelling changes in axial velocity from wake expansion was then derived as:

$$\Delta v_e = \Delta v1_e - \Delta v2_e \tag{33}$$

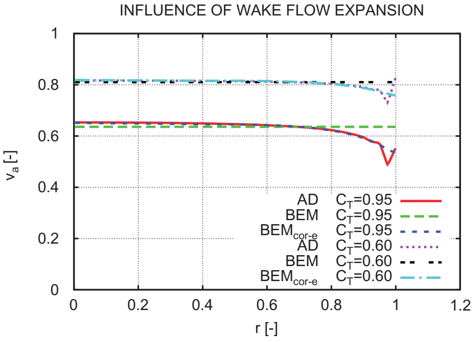

Figure 21. Illustration of result from the sub-model for modelling the influence of wake expansion.

However, the radial velocity cannot be computed with the BEM method. Therefore, the equation from the analytical solution for v_r for a two-dimensional actuator disc, as presented by Madsen,[15] was used. A modification of the analytical equation was made in order to fit the present AD results for an axisymmetric disc:

$$v_r = \frac{1}{2.24}\frac{C_{T_{av}}}{4\pi}\ln\left[\frac{0.04^2 + (r+1)^2}{0.04^2 + (r-1)^2}\right] \tag{34}$$

The average $C_{T_{av}}$ as function of radius was derived as:

$$C_{T_{av}} = \frac{\int_0^r C_T 2\pi r dr}{\pi r^2} \tag{35}$$

The C_T used in the above equation was found from equation (10), but using an induction factor corresponding to the axial flow velocity after the pressure correction given by equation (25). As the pressure correction has the influence of increasing the flow velocity through the disc, the corresponding C_T will decrease and even become negative on the inner part, which results in a negative radial velocity close to the centre line. One example of the influence of the two velocity correction terms for wake expansion as given by equations (30)–(32) is shown in Figure 21. Corrected axial velocity distributions at the disc are shown in comparison with AD, and standard BEM results for C_T of 0.60 and 0.95, respectively. However, it should be noted that the C_T derived from the corrected induction from wake rotation is only used for derivation of the radial velocity, and there is no update at this stage of the input C_T.

One example of the variation of the two correction terms Δv_w, Δv_e is shown in Figure 22 for the loading shown in Figure 6. At this high loading, the Δv_w is considerable on the inboard part of the rotor.

As we now have derived two engineering sub-models that have been directly calibrated against a numerical AD model, we propose in the final equation for the corrected

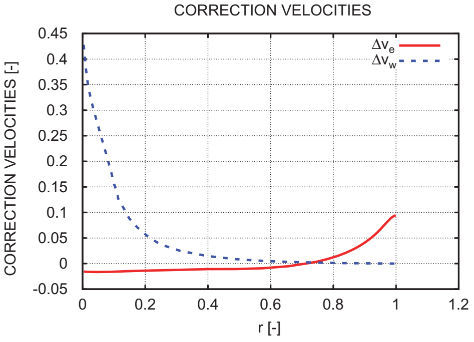

Figure 22. The two velocity correction terms for pressure from wake rotation and reduced tip region inflow from wake expansion at the loading shown in Figure 6.

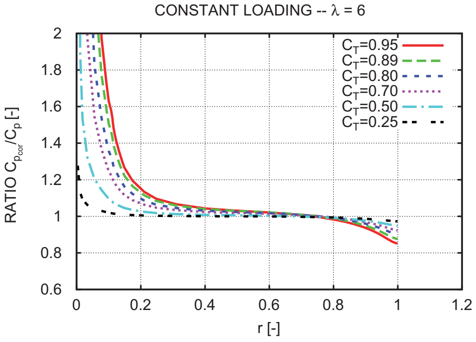

Figure 23. Comparison of the standard BEM and the BEM$_{cor}$ model for a constant loading and a tip speed ratio of 6 at different thrust coefficients.

Table I. Variation of the mass flow factor $k_{massflow}$ as function of thrust coefficient C_T for a constant loading and a tip speed ratio of 1.

C_T	0.2	0.4	0.6	0.8	0.89	0.95
$k_{massflow}$	1.005	1.007	1.004	1.001	1.001	1.004

Table II. Ratio of integrated C_P computed with the BEM$_{cor}$ and BEM model, respectively, for the simulation case shown in Figure 23.

C_T	0.95	0.89	0.80	0.70	0.50	0.25
$\frac{BEM_{cor}\ C_P}{BEM\ C_P}$	1.00	1.00	1.00	1.00	0.99	0.99

axial velocities in the BEM model to include an optional mass flow factor $k_{massflow}$, which adjusts the total mass flow in the corrected model to be the same as in the uncorrected BEM model:

$$v_{a-cor} = k_{massflow}((1-a) + \Delta v_w - \Delta v_e) \tag{36}$$

We denote it optional because in general, it should be set to 1 as there is no direct link between the physical mechanism behind the two correction terms: i) pressure term from wake rotation; and ii) wake expansion causing reduced inflow in the tip region. However, it turned out, as shown previously, that the two terms almost cancel each other, and in this way, the value of the factor will be computed to be close to 1. The reason to introduce the mass flow factor is that there could be applications (e.g. where the BEM model is used in an aeroelastic model for certification of turbines) where it is desirable to link a corrected BEM model as close as possible to an uncorrected BEM, but still introducing the changes from the two sub-models with influence on the load distribution on the blades. As an example, the mass flow factor for the load distribution in Figure 6 has been derived for different C_T, and as seen in Table I, the factor is, in this case, very close to 1.0.

8. RESULTS

8.1. Influence of loading and tip speed ratio

In order to provide an overview of the influence of the two correction terms in the BEM$_{cor}$, model a comparison with the standard BEM model is made for different constant loadings at a tip speed ratio of 6. The comparison is made by showing the ratio between the C_P for the BEM and BEM$_{cor}$ model in Figure 23, and the increase in deviations between the two models for increasing loading is clear. On the inboard part of the rotor, the deviations are much more pronounced than on the outer part. However, because of the increasing relative contribution to the total rotor area, the total power for the two models remains almost the same independent of loading as shown in Table II. It should be noted that the mass flow factor has not been applied.

The influence of tip speed ratio when comparing the BEM and BEM$_{cor}$ model is shown in Figure 24. As the tip speed ratio decreases, the influence of the pressure from wake rotation increases, causing the ratio of the power coefficients to increase considerably on the inboard part of the rotor. On the outer part of the rotor, the changes are small and this means that the BEM$_{cor}$ model predicts a higher total C_P for decreasing lambda, as shown in Table III.

8.2. Comparison of simulations on rotor 1

Next computations results for the constant loaded rotor (see loading in Figure 6) with the corrected BEM model is shown in Figures 25 and 26 in comparison with the AD results and results from the standard BEM model. The introduction of the correction models is seen to improve the correlation with the AD results substantially and the axial velocity profiles at the disc almost coincide (Figure 25 left graph). Also, for the radial velocity, the correlation is good, in particular on the outboard part (Figure 25 right). For the local C_P shown in the left figure in Figure 26, there is also a very good correlation between the corrected BEM model and the AD results, whereas the BEM model underpredicts C_P on the inboard 60% of the rotor and overpredicts C_P on the outboard part. In total, these deviations almost cancel out as shown on the right graph in Figure 26, where the local, average $C_{P_{av}}$ is shown as function of radius.

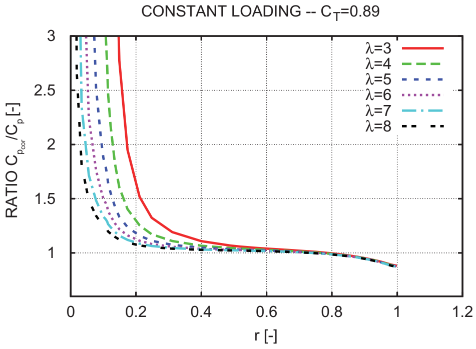

Figure 24. Comparison of the standard BEM and the BEM$_{cor}$ model at a constant loading with a thrust coefficient of 0.89 and for different tip speed ratios.

Table III. Ratio of integrated C_P computed with the BEM$_{cor}$ and BEM model, respectively, for the simulation case shown in Figure 25.

λ	3	4	5	6	7	8
$\frac{BEM_{cor}\ C_P}{BEM\ C_P}$	1.04	1.02	1.01	1.00	0.99	0.99

8.3. Comparison of simulations on rotor 2

The loading on rotor 2, shown in Figure 27, was derived in order to obtain constant induction on the main part of the rotor for a lambda of 8. As seen in Figure 28, a constant velocity, and thus, also a constant induction, was obtained on a major part of the rotor from radius 0.1 to radius 0.7 when computed with the AD and the BEM$_{cor}$ model. From radius 0.7 and to the tip, a constant loading was chosen, as seen in Figure 27. This particular loading was the one chosen for the design of the rotor presented in Johansen *et al.*[10,13] It appears clearly from Figure 28 that the standard BEM computes a lower velocity in the region from radius 0.7 and inboard. A high local C_P was obtained on a major part of the rotor as seen in Figure 29, and exceeds 0.6 from about radius 0.7 and to 0.1, which is quite different from the results of the standard BEM model. When looking in Figure 30 at the local average $C_{P_{av}}$, this is underestimated

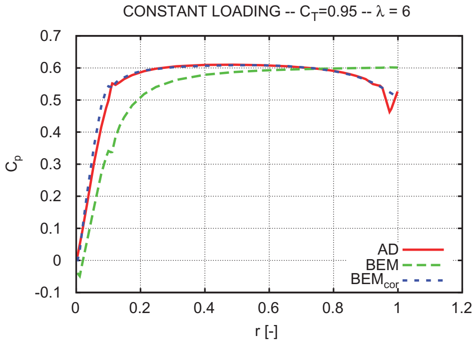

Figure 26. In the left figure, the local power coefficient computed with the BEM, BEM$_{cor}$ and AD model is shown. To the right is the average $C_{P_{av}}$ computed with the BEM$_{cor}$ is shown in comparison with AD results.

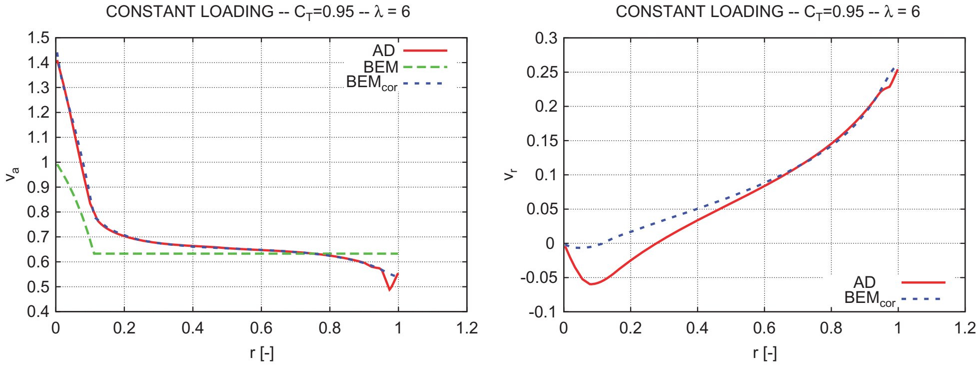

Figure 25. In the left figure, the axial velocity distribution at the disc computed with the BEM, BEM$_{cor}$ and AD model is shown. To the right is the radial velocity computed with the BEM$_{cor}$ model shown in comparison with AD results.

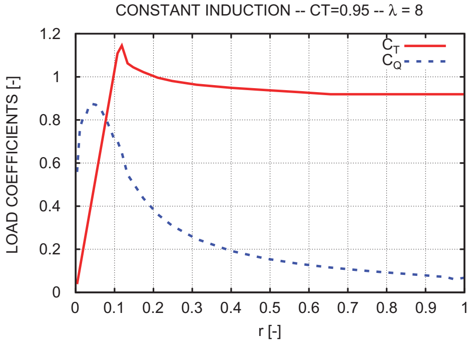

Figure 27. The loading on rotor 2 was derived in order to obtain constant induction over a major part of the rotor.

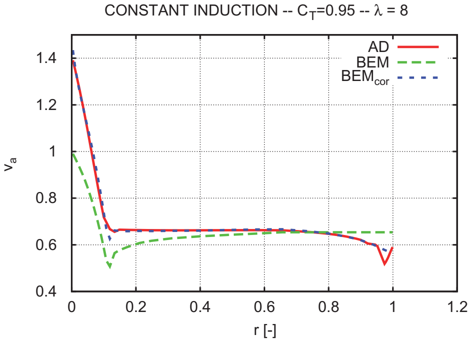

Figure 28. The axial velocity distribution at the rotor disc for rotor 2 computed with the AD, the BEM and the BEM_{cor} model.

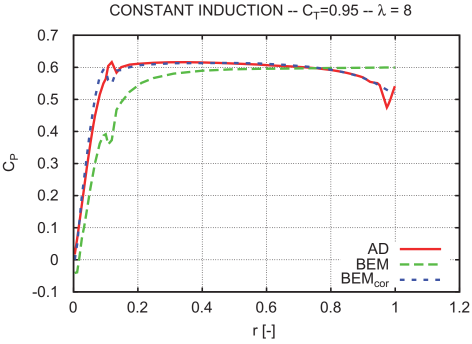

Figure 29. The local C_P for rotor 2 computed with the AD, the BEM and the BEM_{cor} model.

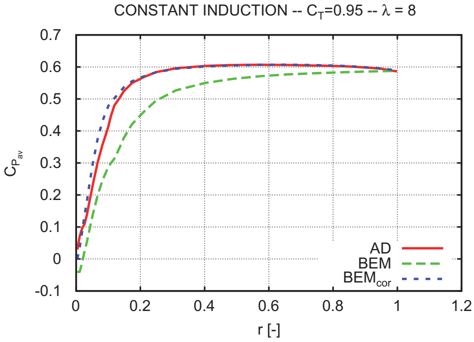

Figure 30. The local average $C_{P_{av}}$ for rotor 2 computed with the AD, the BEM and the BEM_{cor} model.

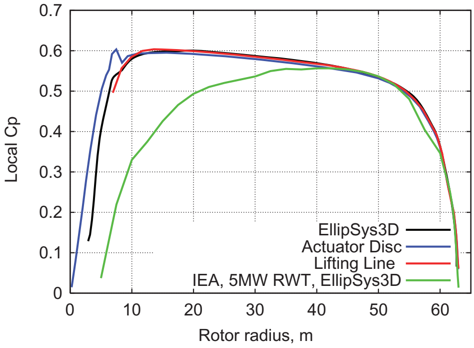

Figure 31. The graph reproduced from Johansen et al.[10] shows the C_P as function of radius from computations with the AD model, a lifting line model and a full 3D CFD model EllipSys3D, respectively, on a 5 MW rotor with the design objective of maximum C_P. Tip speed ratio 8 and a thrust coefficient of 0.89.

by the BEM method until the tip where all models give the same result which is the integrated C_P for the whole rotor.

As mentioned above, the loading in Figure 27 was the basis for the design of the rotor presented in Johansen *et al.*,[10,13] where the design target was maximum rotor efficiency. The three-bladed rotor was designed for a tip speed ratio of 8, and the 15% thick Risø-B1-15 airfoil was used along the whole blade span. Simulations on this rotor with three different models, the AD model, a lifting line model and a full 3D CFD model EllipSys3D were presented in Johansen *et al.*[10,13] and one of the graphs showing the local power coefficient along the blade radius is presented below in Figure 31. It is seen that there is a close correlation between the three model results and with the EllipSys3D being the most advanced and detailed model

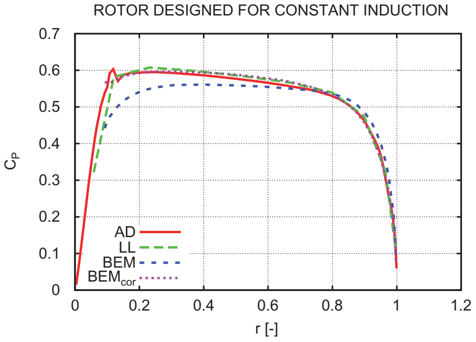

Figure 32. Simulated C_P on the same rotor as in Figure 31 with the AD model, a lifting line model, the BEM and the BEM_{cor} model.

this is a validation of the AD model results. The presented case also confirms that a high C_P on a real rotor in viscid flow can be obtained on the inboard part of the rotor although the local tip speed ratio is low. This confirms that the loss from the wake rotation is compensated by the increased power conversion from the axial loading due to the increased mass flow from the low pressure in the wake.

Finally, computations with the BEM and BEM_{cor} model have been run on the same rotor, Figure 32. The tendencies in comparing the BEM and BEM_{cor} results are the same as conclude several times in this paper. The BEM model under predicts the C_P considerably on the inboard part of the rotor and over predicts on the outer part.

9. SUMMARY AND DISCUSSION

A detailed investigation of the BEM model has been carried out on basis of numerical results from an AD model. The comparisons show that the BEM model overestimates the induction on the inboard part of the rotor due to neglecting the pressure term in the wake from wake rotation. At the tip, the tendency is opposite and the increased induction on the outboard part of the rotor computed with the AD model seems to be due to wake expansion. Two engineering sub-models to be incorporated in the BEM model have been developed, and the specific implementation in the BEM loop is summarized in Appendix A.

The results of the corrected BEM model correlates very well with AD simulations for a number of different load forms. The BEM_{cor} model has also the advantage that the flow quantities in the stream tubes are no longer independent as both correction terms are based on integral quantities. The study has shown that the integrated C_P computed with the standard BEM model correlates very well with AD results at tip speed ratios from 6–8, and this also holds for the BEM_{cor} model. However, the distribution of local C_P is quite different when comparing the standard BEM model with the BEM_{cor} model for rotors with high loading, and in particular, high loading on the inboard part.

For decreasing tip speed ratios below 6, an increase in integrated C_P is predicted with the BEM_{cor} model, and is 4% at a tip speed ratio of 3.

As most industrial blade designs are developed using aerodynamic models based on the BEM theory, an inclusion of modelling the two mechanisms described in the present paper could lead to slightly modified trends in new designs. The main observation is that the inboard part of the blade does not necessarily have a low performance because of the low local tip speed ratio. One design trend could thus be to be more focussed on how to obtain the high loading on the inboard part of the blade in order to achieve the high performance. Another point could be to look more into the potentials of lowering the tip speed ratio at low wind speeds and in this way reduce the influence of airfoil drag and still obtain a high aerodynamic performance because the decrease in tip speed ratio does not necessarily decrease the performance as much as has previously been expected. Also, the optimal pitch setting could be changed slightly as the maximum C_P occurs at a higher thrust coefficient.

APPENDIX A

The implementation of the two sub models in the BEM loop. Equation numbers refer to the equation in the main text.

1. Compute loading coefficients

$$C_T = \frac{dT}{\frac{1}{2}\rho V_0^2 2\pi r dr} = \frac{V_r^2 C_y c N_B}{V_0^2 2\pi r}$$
$$C_Q = \frac{dQ}{\frac{1}{2}\rho V_0^2 r 2\pi r dr} = \frac{V_r^2 C_x c N_B}{V_0^2 2\pi r} \tag{3A}$$

2. Compute axial and tangential induction

$$a = k_3 C_T^3 + k_2 C_T^2 + k_1 C_T \tag{10A}$$

$$a` = C_Q \frac{1}{4(1-a)\lambda_r} \tag{8A}$$

3. Compute mass flow $\dot{m}_{BEM}$ for uncorrected BEM

$$\dot{m}_{BEM} = \int_0^1 (1-a) 2\pi r dr$$

4. Compute wake pressure as function of radius

$$p_w = \int_1^r \frac{v_t^2}{r} dr \tag{21A}$$

where $v_t = 2a`\lambda_r$.

5. Compute new axial and tangential induction due to wake pressure from wake rotation as function of radius

$$\Delta v_w = 0.7 p_w \tag{23A}$$

$$v_{a-cor1} = (1-a) + \Delta v_w \tag{24A}$$

$$a_{cor1} = (1 - v_{a-cor1}) \tag{25A}$$

$$a`_{cor1} = C_Q \frac{1}{4(1-a_{cor1})\lambda_r} \tag{26A}$$

6. Repeat from 3 until convergence
7. Derive a local, corrected C_{T-cor1} (only for computation of the radial velocity) taking into account the influence on the flow from wake rotation

$$C_{T-cor1} = 2.4803a_{cor1}^3 - 4.3767a_{cor1}^2 + 3.8559a_{cor1}$$

$$C_{Tav-cor1} = \frac{\int_0^r C_{T-cor1} 2\pi r dr}{\pi r^2} \tag{35A}$$

8. Compute the radial velocity from the average local thrust coefficient

$$v_r = \frac{1}{2.24}\frac{C_{Tav-cor1}}{4\pi}\ln\left[\frac{0.04^2 + (r+1)^2}{0.04^2 + (r-1)^2}\right] \tag{34 A}$$

9. Compute velocity correction $\Delta v1_e$ from wake expansion as function of radius

$$k3 = -15.83r + 20.73 \tag{27A}$$

$$k2 = -0.52r - 0.90 \tag{28A}$$

$$k1 = 1.58r^2 - 1.63r + 0.51 \tag{29A}$$

$$\Delta v1_e = k3v_r^3 + k2v_r^2 + k1v_r \tag{30A}$$

10. Compute velocity correction $\Delta v2_e$ from wake expansion

Interval $0.05 \le v_{r09} < 0.15$:

$$\Delta v2_e = 1.0361v_{r09}^2 - 0.0961v_{r09} + 0.00003 \tag{31A}$$

Interval $0.15 \le v_{r09} < 0.20$:

$$\Delta v2_e = -2.3894v_{r09}^2 + 0.9642v_{r09} - 0.0817 \tag{32A}$$

For $v_{r09} < 0.05$, equation (31A) was used with $v_{r09} = 0.05$, and for $v_{r09} \ge 0.2$, equation (26) was used with $v_{r09} = 0.20$

11. Compute final velocity correction Δv_e from wake expansion

$$\Delta v_e = \Delta v1_e - \Delta v2_e \tag{33A}$$

12. Compute mass flow $\dot{m}_{BEM_{cor}}$ for corrected BEM

$$\dot{m}_{BEM_{cor}} = \int_0^1 (1 - a + \Delta v_w - \Delta v_e) 2\pi r\, dr$$

13. Compute mass flow factor $k_{massflow}$

$$k_{massflow} = \frac{\dot{m}_{BEM_{cor}}}{\dot{m}_{BEM}}$$

14. Compute final corrected velocity v_{a-cor} at disc and corrected induction a_{cor}

$$\begin{aligned} v_{a-cor} &= k_{massflow}((1-a) + \Delta v_w - \Delta v_e) \\ a_{cor} &= (1 - v_{a-cor}) \end{aligned} \tag{36A}$$

15. Compute corresponding final corrected $a`_{cor}$ and final corrected tangential **velocity** v_{t-cor}

$$a`_{cor} = C_Q \frac{1}{4(1-a_{cor})\lambda_r} \tag{8A}$$

This is now the final, corrected velocities at the rotor disc and a new rotor loading C_T, C_Q derived from the corrected velocities at the rotor disc can be computed. However, for the results shown in the present paper, except the results in Figure 32, C_Q has not been updated when using the BEM and BEM$_{cor}$ models but corresponds in all cases to the AD results. This has been done to in order to show a comparison between the models where the loading has been exactly the same.

REFERENCES

1. Glauert H. Airplane propellers. In *Aerodynamic Theory Volume IV*, Durand WF (ed.). Peter Smith Publisher Inc.: Gloucester; 1963.
2. Wilson RE, Lissaman PBS. Applied aerodynamics of wind power machines. Oregon State University, May 1974.
3. de Vries OM. Fluid dynamic aspects of wind energy conversion. *AGARD Advisory Group for Aerospace Research & Development AGARD-AG-243*. July 1979; C4–C9.
4. Sharp DJ. A general momentum theory applied to an energy-extracting actuator disc. *Wind Energy* 2004; **7**: 177–188.
5. Xiros MI, Xiros NI. Remarks on wind turbine power absorption increase by including the axial force due to the radial pressure gradient in the general momentum theory. *Wind Energy* 2007; **10**: 99–102.

6. Lam GCK. Wind energy conversion limit. CUT-IN NOTE. *Wind Engineering* 2006; **30**: 431–437.
7. Wood DH. Including swirl in the actuator disk analysis of wind turbines. *Wind Enegineering* 2007; **31**: 317–323.
8. Madsen HAa, Mikkelsen R, Johansen J, Bak C, Øye S, Sørensen NN. Inboard rotor/blade aerodynamics and its influence on blade design. In *Research in aeroelasticity EFP-2005. Risø-R-1559(EN)*. Bak C (ed.). Risø National Laboratory (DK): Risø, 2005; 19–39.
9. Johansen J, Madsen HAa, Sørensen NN, Bak C. Numerical investigation of a wind turbine rotor with an aerodynamically redesigned hub-region. *Proceedings of the 2006 European Wind Energy Conference and Exhibition*, Athens, 27 Feb–2 Mar 2006. European Wind Energy Association: Brussels, 2006.
10. Johansen J, Madsen HAa, Gaunaa M, Bak C, Sørensen NN. 3D Navier-Stokes simulations of a rotor designed for maximum aerodynamic efficiency. *Proceedings of the 42nd AIAA Aerospace Sciences Meeting and Exhibit*. ASME Wind Energy Symposium, Reno, NV, 8–11 Jan 2007. American Institute of Aeronautics and Astronautics: Reston, VA, 2007.
11. Madsen HAa. Two modifications of the BEM method based on validation with results of actuator disc simulations. In *Research in Aeroelasticity EFP-2006. Risø-R-1611(EN)*. Bak C (ed.). Risø National Laboratory: Roskilde, Denmark, 2007; 11–20.
12. Madsen HAa, Mikkelsen R, Øye S, Bak C, Johansen J. Detailed investigation of the Blade Element Momentum (BEM) model based on analytical and numerical results and proposal for modifications of the BEM model. *Journal of Physics; Conference Series.* 2007; **75**: 12–16.
13. Johansen J, Madsen HAa, Gaunaa M, Bak C, Sørensen NN. Design of a wind turbine rotor for maximum aerodynamic efficiency. *Wind Energy* 2009; **12**: 261–273.
14. FIDAP 8. *Theory Manual*. Fluent Inc.: Lebanon, NH, USA, 1998.
15. Madsen HAa. A CFD Analysis of the actuator disc flow compared with momentum theory results. In *Proceedings of IEA Joint Action of 10th Symposium on Aerodynamics of Wind Turbines*, Edinburgh, 16–17 December, 1996 Pedersen BM (ed.). Technical University of Denmark: Kgs. Lyngby, Denmark, 1996; 109–124.
16. Madsen HAa, Rasmussen F. The influence on energy conversion and induction from large blade deflections. In *Proceedings of the European Wind Energy Conference 1999*, Nice, 1–5 Mar 1999. Petersen EL, Hjuler Jensen P, Rave K, Helm P, Ehmann H (eds.), James and James Science Publishers: London, 1999; 138–141.
17. Madsen HAa. Yaw simulation using a 3D actuator disc model coupled to the aeroelastic code HawC. In *IEA Joint Action. Aerodynamics of Wind Turbines. 13. Symposium*, Stockholm, 29–30 Nov 1999. Maribo Pedersen B (ed.). Technical University of Denmark: Kgs. Lyngby, Denmark, 2000; 133–145.
18. Madsen HAa, Sørensen NN; Schreck S. Yaw aerodynamics analyzed with three codes in comparison with experiment. In *AIAA Paper 2003-519. 41. Aerospace Sciences Meeting and Exhibit*, Reno, NV, 6–9 Jan 2003. American Institute of Aeronautics and Astronautics, Inc.: Reston, VA, 2003.
19. Sørensen NN, Madsen HAa. Modelling of transient wind turbine loads during pitch motion (paper and poster). In *Proceedings of the 2006 European Wind Energy Conference and Exhibition*, Athens, 27 Feb–2 Mar 2006. European Wind Energy Association: Brussels, 2006.
20. Mikkelsen R, Sørensen JN, Shen WZ. Modelling and analysis of the flow field around a coned rotor. *Wind Energy* 2001; **4**: 121–135.
21. Sørensen JN, Shen WZ, Mundate X. Analysis of wake states by a full-field actuator disc model. *Wind Energy* 1998; **1**: 73–88.
22. Øye S. A simple vortex model. In *Proceedings of the Third IEA Symposium on the Aerodynamics of Wind Turbines*, ETSU, Harwell, 1990; 5.1–5.15.

WIND ENERGY
Wind Energ. 2010; **00**:1–10
DOI: 10.1002/we

RESEARCH ARTICLE

Aerodynamic optimization of wind turbine rotors using a BEM method with corrections for wake rotation and expansion

Mads Døssing[1], Helge Aa. Madsen[1], Christian Bak[1]

[1]Division of wind energy, Risø National Laboratory for Sustainable Energy, Technical University of Denmark, PO 49, DK-4000 Roskilde, Denmark

ABSTRACT

The blade element momentum method (BEM) is widely used for calculating the quasi steady aerodynamics of horizontal axis wind turbines. Recently, the BEM method has been expanded to include corrections for wake expansion and the pressure due to wake rotation (BEM_{cor}) and more accurate solutions can now be obtained in the blade root and tip sections. It is expected that this will lead to small changes in optimum blade designs. In this work BEM_{cor} has been implemented and the spanwise load distribution has been optimized in order to find the highest possible power production. For comparison optimizations have been carried out using BEM as well. Validation of BEM_{cor} shows good agreement with the flow calculated using an advanced actuator disc method. The maximum power was found at a tip speed ratio of 7 using BEM_{cor} and this is lower than the optimum tip speed ratio of 8 found for BEM. The difference is primarily caused by the positive effect of wake rotation which locally causes the efficiency to exceed the Betz limit. Wake expansion has a negative effect which is most important at high tip speed ratios. It was further found that using BEM_{cor} it is possible to obtain a 5% reduction in flap bending moment when compared to BEM. In short, BEM_{cor} allows fast aerodynamic calculations and optimizations with a much higher degree of accuracy than the traditional BEM model. Copyright © 2010 John Wiley & Sons, Ltd.

KEYWORDS

Wind turbine; aerodynamics; optimization; blade element momentum method; wake expansion; wake rotation

Correspondence

Journals Production Department, John Wiley & Sons, Ltd, The Atrium, Southern Gate, Chichester, West Sussex, PO19 8SQ, UK.

Received . . .

1. NOTATIONS

a	Axial induction factor	-
a'	Tangential induction factor	-
b	Blade design parameter	-
c	Chord	m
C_l	Lift coefficient	-
C_d	Drag coefficient	-
C_P	Power coefficient	-
C_T	Thrust coefficient	-
C_F	Root flap moment coefficient	-
C_t	Local thrust coefficient	-
C_q	Local torque coefficient	-
C_p	Local power coefficient	-
C_x	Tangential force coefficient	-
C_y	Axial force coefficient	-
d	Drag	N
F	Tip loss	-

Prepared using weauth.cls [Version: 2010/06/17 v1.00]

$k_1,\ k_2,\ k_3$	Constants, $a(C_t/F)$ relation	-
l	Lift	N
M_F	Root flapwise bending moment	Nm
N_B	Number of blades	-
p_w	pressure from wake rotation	-
P	Power	W
r	Coordinate, radius	m
R	Rotor radius	m
T	Thrust	N
v_a	Axial wind speed relative to blade section	m/s
v_t	Tangential wind speed relative to blade section	m/s
v_r	Radial/spanwise wind speed relative to blade section	m/s
v_{rel}	Wind speed relative to blade	m/s
V_0	Wind speed	m/s
x	Coordinate, edge	m
y	Coordinate, flap	m
α	Angle of attack	radians (degrees)
β	Twist	radians (degrees)
Δv_w	Correction for wake rotation	-
Δv_e	Correction for wake expansion	-
λ	Tip speed ratio	-
Ω	Rotational speed	s^{-1}
ρ	Mass density	kg/m^3
ϕ	Inflow angle	radians (degrees)
obj	Objective function	
BEM	Blade element momentum method	
BEM_{cor}	Blade element momentum method, corrected	
ACD	Actuator disc	
CFD	Computational fluid dynamics	

2. INTRODUCTION

The blade element momentum method (BEM) in its original form has in recent years been subjected to a thorough investigation with the purpose of determining its accuracy with respect to performance on the inner part of the rotor. These investigations were initiated by the wind turbine manufacturer Enercon, Germany, claiming that the reason for their proven high power efficiency of certain turbines was the increased performance on the root part of the rotor, where the power efficiency locally was higher than the Betz limit with a power efficiency of C_P=16/27.

Madsen et al. [1][2] analyzed the phenomenon in detail and found as claimed an increase on the inner part of the rotor if it was exposed to sufficiently high loading. The explanation for this increase of power efficiency was that for wind turbines in normal operation the rotation of the wake causes an acceleration of the axial flow on the inner part. On the outer part of the rotor wake expansion causes a deceleration of the flow. Both effects are not captured in the standard BEM model and among other issues this has led to the conclusion that the power production from the inner part of the blade is underestimated and conversely overestimated on the outer part. The cause for this is believed to be the failure of the BEM method to accurately predict the axial velocities, for a given loading, correctly. The result from the work by Madsen et al. [1][2] are the BEM corrections for the axial flow. If these are implemented the method is denoted corrected blade element momentum method (BEM_{cor}).

In [1] main focus is on the derivation of the corrections and the corrected velocities are validated against an actuator disc (ACD) calculation. This is done for a defined loading and no iterations are carried out. In this work the corrections are implemented in a full BEM_{cor} algorithm where the loading is updated according to the velocities in the rotor plane. It is noted that due to numerical issues the results of BEM_{cor} are sensitive to the order in which various properties are updated when iterating and care must be taken that the implementation is validated correctly. For this reason our implementation of the BEM_{cor} algorithm has been validated thoroughly.

In this work rotor blades have been optimized using BEM and BEM_{cor} for calculation of properties along the blade span - including effects of drag and tip losses. The optimization variable is the spanwise distribution of the axial induction, which corresponds to an optimization of the aerodynamics and the optimum aerodynamic load distribution is found. The

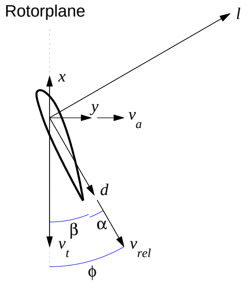

Figure 1. Sketch of the section properties

objective is either maximum power or maximum power to thrust ratio at reduced loading. The resulting power, thrust, flap bending moment and distributed properties are then studied. The optimized blade designs may deviate from what is reasonable from a manufacturer's point of view. E.g. the chord is unconstrained and very large near the blade root. However, an unconstrained optimization is necessary in order to make sure the full potential of the wake rotation is utilized. The blade layout is illustrated using the inflow angle and a design parameter. This has the advantage that the chord and twist are not ultimately defined but will depend on the design lift coefficient, which can be selected by varying the twist in order to obtain the desired angle of attack. Thus, even though the blade stiffness and other structural properties are not considered, there is some freedom in the selection of the chord. The profile thickness distribution is not considered and it is assumed that it is possible to obtain the design lift and drag.

The results of the BEM method are usually expressed using the dimensionless power and thrust coefficients which depend on the tip speed ratio. A similar dimensionless coefficient for the root flapwise bending moment has been defined.

Note that results are reported for both BEM and BEM_{cor}. Thus, they represent optimized results obtained using the two methods and this shows the fundamental differences in the predicted optima. The differences when calculating the aerodynamics of a given design is also relevant but for simplicity this is not included in this work. The single exception is the validation part where properties for a defined turbine has been calculated.

3. METHODS

The BEM_{cor} algorithm yields general results because everything can be expressed in dimensionless form. For a given blade design all variables will only depend on the tip speed ratio λ defined as

$$\lambda = \frac{\Omega R}{V_0}\,, \quad \lambda_r = \frac{\Omega r}{V_0} \tag{1}$$

where λ_r is the local speed ratio. Dimensionless parameters are

$$r^* = \frac{r}{R}\,, \quad c^* = \frac{c}{R}\,, \quad v_a^* = \frac{v_a}{V_0}\,, \quad v_t^* = \frac{v_t}{V_0}\,, \quad v_r^* = \frac{v_r}{V_0} \tag{2}$$

The power, thrust and flap moment coefficients are defined below, as well as dimensionless distributed forces etc. A dimensionless design parameter for the blade aerodynamic layout b is also defined later. Figure 1 shows the basic quantities in a blade section.

3.1. The corrected BEM method

The classic BEM method is described by e.g. Glauert [3] and Hansen [4]. The theory relates the aerodynamic forces to the induction factor a, which describes the slowing of the free wind measured in the rotorplane. The corrected BEM method (BEM_{cor}) is described in [1] and the governing equations are repeated below.

The local aerodynamic forces are expressed using a normal force coefficient C_y and a tangential force coefficient C_x

$$C_x = C_l \sin\phi - C_d \cos\phi \tag{3}$$

$$C_y = C_l \cos\phi + C_d \sin\phi \tag{4}$$

where C_l and C_d are the lift and drag coefficients, and ϕ is the flow angle (see Figure 1). In this work C_l and the lift-to-drag ratio ${}^{l}\!/\!{}_{d} = {}^{C_l}\!/\!{}_{C_d}$ is specified and $C_d = C_l\,({}^{l}\!/\!{}_{d})^{-1}$.

The local thrust coefficient C_t and the local torque coefficient C_q are defined as

$$C_t = \frac{v_{rel}^2 C_y c N_B}{V_0^2 2\pi r} \tag{5}$$

$$C_q = \frac{v_{rel}^2 C_x c N_B}{V_0^2 2\pi r} = \frac{C_x}{C_y} C_t \tag{6}$$

where N_B is the number of blades, V_0 is the free wind speed and v_{rel} is the velocity in the rotorplane relative to the moving blade section. The tip losses are calculated using Prandtl's tip loss factor F

$$F = \frac{2}{\pi} \arccos \left[\exp \left(-\frac{N_B}{2} \frac{R - r}{r \sin \phi} \right) \right] \tag{7}$$

For low loading (a <0.3) an analytical expression for the axial induction factor is valid

$$a = \left(\frac{8\pi r F \sin^2 \phi}{C_y c N_B} + 1 \right)^{-1} \tag{8}$$

However, an empirical relationship is necessary at higher loading and (8) is replaced by a polynomial which approximates an actuator disc solution at high loading and (8) at low loading (Ref. [1])

$$a = k_3 \left(\frac{C_t}{F} \right)^3 + k_2 \left(\frac{C_t}{F} \right)^2 + k_1 \left(\frac{C_t}{F} \right) \tag{9}$$

For an undeflected and unconed rotor the constants are

$$k_3 = 0.08921\,, \quad k_2 = 0.05450\,, \quad k_1 = 0.25116$$

The tangential induction a' is

$$a' = \frac{C_q}{4(1 - a)\lambda_r} \tag{10}$$

The first BEM correction Δv_w represents the increase in axial velocity through the rotorplane due to the pressure drop behind the turbine caused by wake rotation. It is defined as

$$\Delta v_w = 1.0 p_w\,, \quad p_w = \int_1^{r^*} \frac{v_t^{*2}}{r^*} \, dr^* \tag{11}$$

where v_t^* is the dimensionless tangential velocity and p_w is the dimensionless pressure due to wake rotation. In [1] the factor 1.0 is replaced by the empirical factor 0.7, which yielded a better agreement with ACD data. An explanation for this is that not all the pressure deficit is converted into axial velocity. However, in this work the value 1.0 is used because the validation shows good agreement with ACD data. It is believed that the difference in results is caused by details in the implementations and especially important is the order in which quantities are updated.

The second BEM correction Δv_e represents the decrease in axial velocity due to wake expansion. It is determined from 2nd and 3rd order polynomial fits describing the difference between BEM and ACD results. I.e.

$$\Delta v_e = \Delta v_e(v_r^*) \tag{12}$$

where v_r^* is the radial velocity evaluated using an analytical solution for a 2 dimensional ACD (Madsen [5]). The derivation of Δv_e and Δv_w is relatively complicated and is described in great detail in [1]. Here it is important to mention that the corrections are in dimensionless form (scaled by V_0) and there is flow similarity for fixed λ.

The axial velocity v_a, the tangential velocity and the flow angle are

$$v_a = (1 - a + \Delta v_w - \Delta v_e) V_0 \tag{13}$$

$$v_t = \lambda_r (1 + a') V_0 \tag{14}$$

$$\phi = \arctan \frac{v_a}{v_t} \tag{15}$$

The local angle of attack α can finally be calculated as the difference in the flow angle and the twist β

$$\alpha = \phi - \beta \tag{16}$$

The lift and drag coefficients are determined according to the angle of attack and an iteration loop is then necessary in order to find a converged solution for all quantities in Equations (3)-(16). Note that the BEM corrections only appear explicitly in Equation (13).

3.2. Power, thrust and root moment

The local shaft power coefficient is defined as

$$C_p = \frac{\Omega v_{rel}^2 C_x c N_B}{V_0^3 2\pi} = \lambda_r C_q \tag{17}$$

The shaft power, the thrust and the root flapwise bending moment can now be expressed dimensionless as

$$C_P = \frac{P}{{}^1\!/_2 \rho V_0^3 \pi R^2} = \frac{2}{R^2}\int r C_p \, dr \tag{18}$$

$$C_T = \frac{T}{{}^1\!/_2 \rho V_0^2 \pi R^2} = \frac{2}{R^2}\int r C_t \, dr \tag{19}$$

$$C_F = \frac{M_F N_B}{{}^1\!/_2 \rho V_0^2 \pi R^3} = \frac{2}{R^3}\int r^2 C_t \, dr \tag{20}$$

3.3. Optimization algorithm

The optimization algorithm is an unconstrained steepest descent method with step length determined by the golden section method (see e.g. Sun and Yuan [6]). The design variables are 36 discrete values of the axial induction a distributed along the blade span using a cosine spacing to pack the blade elements closer near the root and tip. The innermost element is at r^*=0.1 . In each iteration C_t is determined numerically using (9) and the chord is varied according to (5)

$$c = \frac{C_t V_0^2 2\pi r}{v_{rel}^2 C_y N_B} \tag{21}$$

Except C_l and ${}^l\!/_d$ which are defined, all other properties are updated according to the BEM$_{\mathrm{cor}}$ algorithm described above. The optimization objective is either the power

$$obj = -C_P \tag{22}$$

or the power to thrust ratio

$$obj = -\frac{C_P}{C_T} \exp\left(-\frac{\left(C_P - C_{P,design}\right)^2}{2 \cdot 0.05^2}\right) \tag{23}$$

The exponential is a penalty function included to keep C_P close to the desired value $C_{P,design}$. $C_{P,design}$ is a specified power and it is around this operating point the thrust is minimized. If the penalty function is not included the optimization will yield a very low power because the power to thrust ratio is highest at low loading. The penalty function is a normalized Gaussian distribution function with mean $C_{P,design}$ and standard deviation 0.05 .

3.4. Blade design parameters

The blade designs are visualized using the inflow angle ϕ and a blade design parameter b defined as

$$b = c^* C_l N_B \tag{24}$$

In this way the chord is not finally described because it will depend on the design lift coefficient and N_B. b is defined by combining (4) and (5) and assuming negligible influence of drag, i.e. $C_d \sin\phi << C_l \cos\phi$. Then

$$b = \frac{C_t V_0^{*2} 2\pi r^*}{{v_{rel}^*}^2 \cos\phi} \tag{25}$$

The quantities on the right hand side all follows from the the dimensionless aerodynamic analysis. Note that b will depend on N_B because of tip losses which affects ϕ and v_{rel}^*. However, this dependency is small and limited to the outer part of the rotor and only a small error is introduced when N_B is included in b (N_B=3 was used in the optimizations). In a final design the chord is

$$c^* = \frac{b}{N_B C_{l,design}(\alpha_{design})} \tag{26}$$

The twist is defined in order to obtain the design angle of attack

$$\beta = \phi - \alpha_{design} \tag{27}$$

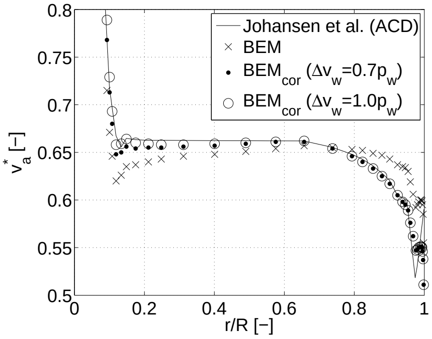

Figure 2. Dimensionless axial velocities in the rotorplane. BEM$_{cor}$ yields a good approximation to the actuator disc results.

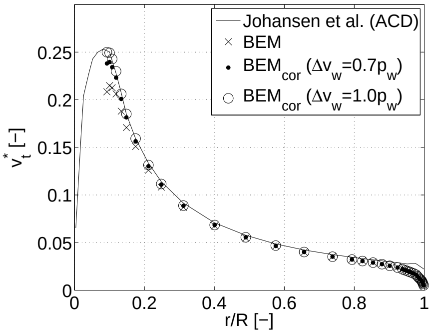

Figure 3. Dimensionless tangential velocities. Note that the kinematic velocity due to rotation is not included.

3.5. Actuator disc calculations

The ACD method is based on computational fluid dynamics (CFD) and is therefore more advanced than BEM$_{cor}$. A description of the specific implementation is given in [1]. The ACD input is the values of C_q and C_t/F calculated using BEM or BEM$_{cor}$. Note that tip losses are included by correcting the mechanical loading C_t to obtain the equivalent ACD loading C_t/F.

4. DISCUSSION

4.1. Validation

BEM$_{cor}$ was validated against ACD by comparing the velocities calculated for the same loading. As a test case the optimum rotor described in Johansen et al. [7] was used. This is a rotor designed for maximum power at λ=8 using Risø B1-15 airfoils with design C_l=1.4 and $^l/_d$=110 on the entire rotor. The rotor is a redesign of the NREL 5MW reference rotor (Jonkman et al. [8]). In the BEM and BEM$_{cor}$ calculations the actual blade shape was used (twist, chord and thickness) and actual 2D aerodynamic lift and drag data, which depends on the calculated angle of attack.

Figure 2 shows the axial velocities in the rotorplane. There is an excellent agreement with the BEM$_{cor}$ results. The results of BEM deviate near the tip and root.

The tangential velocities, seen in Figure 3, are comparable on large parts of the blades. There is a noticeable error near the tip but this is not important because the kinematic velocities due to rotation are completely dominating at large radii.

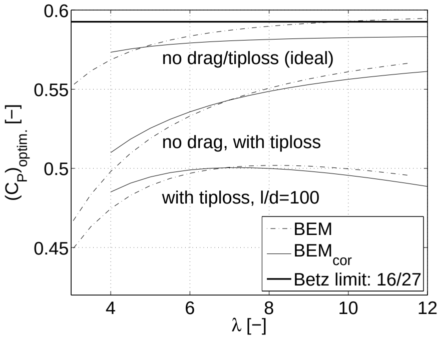

Figure 4. Optimized C_p values for different tip speed ratios.

4.2. Optimum power

It is now interesting to study the optimum power which can be obtained using BEM$_{\text{cor}}$ and compare this to the optima for BEM. The optimizations have thus been carried out using both methods. The investigation is divided into 3 parts. The first is ideal conditions without tip losses and drag. The second includes tip losses. The third includes both drag and tip losses and is therefore representative for a realistic case. Figure 4 shows the optima calculated using λ values in the range from 4 - 12. The results are discussed below.

4.2.1. Optimum power under ideal conditions

The first case, where drag and tip losses are excluded, shows an increase in C_P for increasing λ. However, using BEM$_{\text{cor}}$ the power approaches the Betz limit very slowly because of losses due to wake expansion. At λ=12 it is only 98.7% of the Betz limit whereas BEM exceeds it slightly. At $\lambda <5$ the optimum power using BEM is lowest because the positive effect of wake rotation is not included. Note that there is still a significant negative effect because of the energy lost to wake rotation, which causes the decrease in efficiency at low λ (this is explained in the classical BEM theory). Numerical values of C_P, C_T and C_F are given in Table I. Note that C_T and C_F are increasing with λ when BEM is used but decreasing when BEM$_{\text{cor}}$ is used.

4.2.2. Optimum power with tip loss included

This case is almost equivalent to the previous with the difference that tip losses are included. Tip losses affect the outer part of the rotor resulting in a drop in the optimum power. The reason for this cannot be explained easily because of the complexity in the interconnection of velocities and aerodynamic loads. The result is the centered curves in Figure 4. Note that BEM and BEM$_{\text{cor}}$ predict the same optimum power at λ=7.

4.2.3. Optimum power with tip loss and drag included

The lower curves in Figure 4 show results when tip loss and drag are included. A value of $^{l}/_{d}$=100 is used, which is representative for modern wind turbine airfoils - including leading edge roughness. The value is probably too high for the thick profiles used on the inner part of real rotors, but these will only make a small contribution to the total drag losses (however, it is not negligible). The global optimum for BEM$_{\text{cor}}$ is now at λ=7 which is lower than the global optimum for BEM, which is at λ=8.

For $\lambda <7$ the optimum C_P value is highest for BEM$_{\text{cor}}$ and for $\lambda >7$ the optimum value is highest for BEM. This was also the case when drag was excluded and the reason is that drag in most cases has a very limited effect on the flow which is governed by lift forces. Instead the drag generates a negative shaft driving torque which depends on the lift to drag ratio used and this negative power contribution will affect BEM and BEM$_{\text{cor}}$ in a similar way. The conclusion is that the break even at λ=7 is fairly general, but it may shift slightly according to the optimization which can favour a different loading depending on $^{l}/_{d}$.

Numerical values of C_P, C_T and C_F are given in Table II.

4.2.4. Optimum power - blade layouts

As examples of the actual designs, optimum C_P designs at λ=5 and λ=7 are illustrated. The designs are with tip losses and drag as described above ($^{l}/_{d}$=100). Figure 5 shows the design parameter as function of radius. This is equivalent to the chord distribution for a defined number of blades N_B and design lift C_l (e.g. N_B=3, C_l=1.4). The difference between the

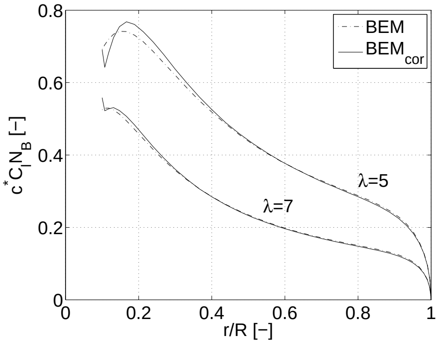

Figure 5. The blade design parameter for optimum C_P found using BEM and BEM$_{\text{cor}}$. At λ=7 there is only a small difference. At λ=5 there is some difference near the root

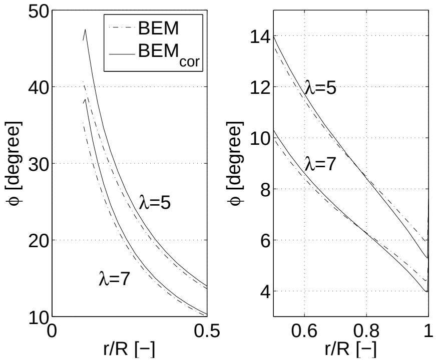

Figure 6. The inflow angle for optimum C_P found using BEM and BEM$_{\text{cor}}$. The difference in inflow angle is significant. Near the root it is approximately 5 degrees and on large parts of the blade the difference is approx. 1 degree.

BEM design and the BEM$_{\text{cor}}$ design is small. A significant difference is only observed in the root region and it is largest at λ=5. This shows that the optimum for BEM$_{\text{cor}}$ requires a slightly increased loading near the root. Overall, the difference is very small and it should be expected that structural properties, e.g. bending stiffness, are practically the same.

Figure 6 shows the inflow angle. Unlike the chord distribution there is a significant difference between BEM and BEM$_{\text{cor}}$. Near the root it is approximately 5 degrees and on large parts of the blade it is 0.5-1 degree. Thus, the more accurate design obtained using BEM$_{\text{cor}}$ has a twist which is different from the BEM design.

4.2.5. Optimum power - local power

It is interesting to study the distribution of C_p because it shows the efficiency of the local energy conversion. This is done at λ=7 for BEM$_{\text{cor}}$ and at λ=8 for BEM because these are the optimum design points for $^l/_d$=100 and are realistic practical designs. Figure 7 shows the results. The Betz limit is exceeded locally on large parts of the blade when BEM$_{\text{cor}}$ is used and drag is omitted. Note that the Betz limit is also slightly exceeded when BEM is used for optimization. This can be explained by the use of Equation (9) which is based on actuator disc calculations and therefore deviates from the momentum solution from which the Betz limit is derived.

4.3. Optimum designs at reduced loading

Up to now optimum designs have been discussed. In practice, turbines are designed to be near optimal because it causes a large increase in C_T and C_F to obtain the optimum design. Thus, C_T is reduced compared to the value at optimum C_P. In this work, the optimization objective at reduced power was defined to be the power to thrust ratio (Equation (23)), which is equivalent to minimizing the thrust for a given power.

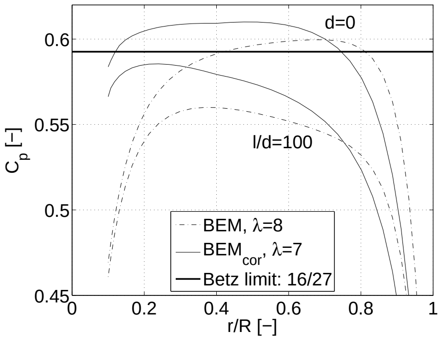

Figure 7. Local C_p distributions for the optimum designs obtained using BEM and BEM$_{\text{cor}}$. They are calculated at the λ values where the global optimum is found. BEM shows that the Betz limit is slightly exceeded, which is possible because Equation (9) is used.

The results from optimizations are seen in Figure 8, which shows C_F and C_T plotted against C_P. The calculations are for λ=6 and λ=8. $^l/_d$=110. It is worth noting that using BEM$_{\text{cor}}$ a blade can be designed which has a 5% lower root flap moment relative to one designed using BEM. The reduction is seen at λ=6 , which is a typical value at rated windspeed where the quasi steady loads are largest and therefore define the design loads for the blade structure. The difference in the moment is caused by the effects of wake rotation and expansion which are most important near the tip and root. BEM$_{\text{cor}}$ includes these and the optimizer consequently increases the aerodynamic loading near the root and decreases it near the tip. This fundamental difference shows the importance of using BEM$_{\text{cor}}$ in structural design and optimization.

5. CONCLUSION

Results of aerodynamic optimizations using both BEM and BEM$_{\text{cor}}$ have been presented. These have shown the significance of using BEM$_{\text{cor}}$, which makes it possible to obtain a degree of accuracy comparable to an actuator disc calculation.

BEM$_{\text{cor}}$ shows an optimum C_P of 0.500 at λ=7. This can be compared to the optimum C_P=0.502 at λ=8, which was found using BEM. Both results are for a realistic lift to drag ratio of 100.

At low tip speed ratios (λ <7) the optimum C_P values are highest for BEM$_{\text{cor}}$, when compared to BEM. The difference is primarily caused by the positive effect of pressure due to wake rotation. At high tip speed ratios (λ >7) the optimum C_P values are lowest for BEM$_{\text{cor}}$. This is primarily because of the negative effect of wake expansion.

The thrust and root flap moments are in general different when designs are optimized using the 2 different methods. Also in the cases where the power is the same. For optimum designs, BEM and BEM$_{\text{cor}}$ yield different inflow angles which is an important difference. The difference in chord distribution is relatively small.

It has been shown that using BEM$_{\text{cor}}$ it is possible to design a blade with a 5% reduction in root flap bending moment. Thus, BEM$_{\text{cor}}$ can lead to designs which are different from those found without taking wake expansion and rotation into account.

REFERENCES

1. Madsen HA, Bak C, Døssing M, Mikkelsen R, Øye S. Validation and modification of the blade element momentum theory based on comparisons with actuator disc simulations. *Wind Energy* 2010; **13**(4):373–389.
2. Madsen HA, Mikkelsen R, Øye S, Bak C, Johansen J. A Detailed investigation of the Blade Element Momentum (BEM) model based on analytical and numerical results and proposal for modifications of the BEM model. *Journal of Physics: Conference Series 75 012016* 2007; .
3. Glauert H. Airplane propellers. *Aerodynamic Theory Volume IV*. 1963; .
4. Hansen MOL. *Aerodynamics of Wind Turbines*. second edn., Earthscan, 2008.
5. Madsen HA. A CFD analysis of the actuator disc flow compared with momentum theory results. *Proceedings of IEA Joint Action, Aerodynamics of Wind Turbines 10th Symposium*, 1996.
6. Wenyu Sun, Ya-Xiang Yuan. *Optimization Theory and Methods, Nonlinear Programming*, vol. 1. Springer, 2006.

Table I. Summary of optimum C_P designs (ideal turbine)

No drag/tip loss	BEM			BEM$_{\text{cor}}$		
λ	C_P	C_T	C_F	C_P	C_T	C_F
4	0.5686	0.9619	0.6506	0.5733	0.9647	0.6446
5	0.5792	0.9694	0.6530	0.5790	0.9628	0.6417
9 6	0.5850	0.9719	0.6541	0.5811	0.9589	0.6398
7	0.5888	0.9737	0.6549	0.5825	0.9561	0.6386
8	0.5914	0.9751	0.6556	0.5834	0.9545	0.6378
9	0.5933	0.9760	0.6560	0.5840	0.9535	0.6373
10	0.5947	0.9769	0.6564	0.5845	0.9526	0.6370
11	0.5958	0.9775	0.6567	0.5849	0.9520	0.6367
12	0.5966	0.9780	0.6569	0.5851	0.9516	0.6365

Table II. Summary of optimum C_P designs (representative for a real turbine)

With tip loss. l/d=100	BEM			BEM$_{\text{cor}}$		
λ	C_P	C_T	C_F	C_P	C_T	C_F
4	0.4746	0.8720	0.5676	0.4851	0.8852	0.5700
5	0.4891	0.8863	0.5792	0.4946	0.8893	0.5765
6	0.4969	0.8944	0.5862	0.4990	0.8914	0.5804
7	0.5007	0.8993	0.5905	0.5005	0.8918	0.5825
8	0.5019	0.9015	0.5928	0.5000	0.8915	0.5835
9	0.5014	0.9031	0.5946	0.4982	0.8905	0.5838
10	0.4997	0.9027	0.5947	0.4956	0.8898	0.5840
11	0.4972	0.9022	0.5947	0.4923	0.8877	0.5832
12	0.4945	0.9012	0.5943	0.4886	0.8855	0.5819

7. Johansen J, Madsen HA, Gaunaa M, Bak C, Sørensen NN. 3D Navier-Stokes Simulations of a Rotor Designed for Maximum Aerodynamic Efficiency. *Proceedings of the 42nd AIAA Aerospace Sciences Meeting and Exhibit*, ASME Wind Energy Symposium, American Institute of Aeronautics and Astronautics, 2007.
8. Jonkman J, Butterfield S, Musial W, Scott G. Definition of a 5-MW Reference Wind Turbine for Offshore System Development. *Technical Report NREL/TP-500-38060*, NREL National Renewable Energy Laboratory 2009.
9. Døssing M. A detailed investigation of the corrected BEM method and the potential for improving blade design. EWEC 2009, conference paper, Marseilles, 2009.
10. Madsen HA, Mikkelsen R, Johansen J, Bak C, Øye S, Sørensen NN. Inboard rotor/blade aerodynamics and its influence on blade design. *Research in Aeroelasticity EFP-2005* 2005; :19–39.
11. Johansen J, Madsen HA, Gaunaa M, Bak C, Sørensen NN. Design of a wind turbine rotor for maximum aerodynamic efficiency. *Wind Energy* 2009; **12**:261–273.
12. Fuglsang P. Aerodynamic Design Guidelines for Wind Turbine Rotors. *A Collection of the 1998 ASME Wind Energy Symposium Technical Papers at the 36th AIAA Aerospace Sciences Meeting and Exhibit* 2002; .
13. Fuglsang P, Madsen HA. Optimization method for wind turbine rotors. *J. Wind Engineering and Industrial Aerodynamics. Vol 80.* 1999; .
14. Burton T, Sharpe D, Jenkins N, Bossanyi E. *Wind Energy Handbook*. John Wiley & Sons, 2001.

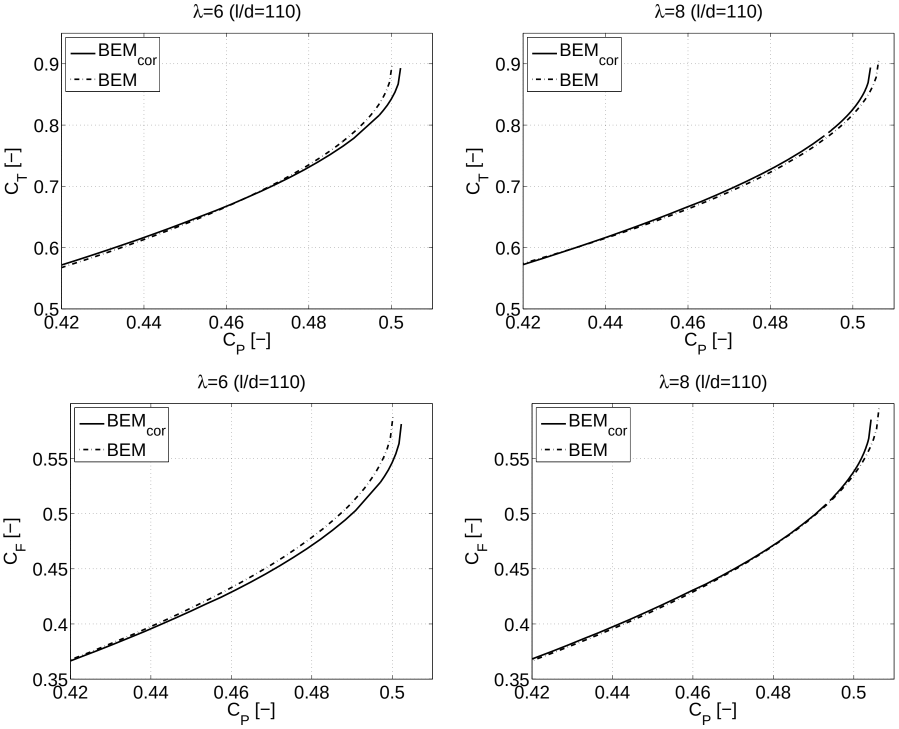

Figure 8. Optimization for low thrust versus C_P values. The results are obtained by optimizing with BEM and $\mathrm{BEM_{cor}}$

WIND ENERGY
Wind Energ. 2010; **00**:1–8
DOI: 10.1002/we

RESEARCH ARTICLE

A numerical and analytical investigation of blade fatigue loads on the NREL 5MW wind turbine

Mads Døssing[1], Christian Bak[1]

[1]Division of Wind Energy, Risø National Laboratory for Sustainable Energy, Technical University of Denmark, PO 49, DK-4000 Roskilde, Denmark

ABSTRACT

The design of blades for horizontal axis wind turbines relies heavily on numerical optimization methods. Estimating the fatigue damage requires aeroelastic simulations in the time domain. This is very time-consuming and simplified methods are much needed. We determined time simulations and resulting fatigue loads on the NREL 5MW reference turbine using HAWC2. We then derived analytical expressions which captured the most important fatigue generating-effects. The results show that gravity and turbulence generate the edgewise fatigue loads. The flapwise loads are mainly caused by turbulence. A number of other factors are also important, but the resulting equations provide a simplified means of predicting fatigue loads which should lead to improvements in blade design as well as a general understanding of the important parameters. Copyright © 2010 John Wiley & Sons, Ltd.

KEYWORDS
wind turbine blade; structural fatigue; atmospheric turbulence; blade design

Correspondence
Journals Production Department, John Wiley & Sons, Ltd, The Atrium, Southern Gate, Chichester, West Sussex, PO19 8SQ, UK.

Received . . .

1. NOTATIONS

a	Axial induction factor	-
c	Chord	m
C_l	Lift coefficient	-
D	Fatigue damage	-
E	Youngs modulus	Pa
f_{eq}	Equivalent frequency	Hz
g	Gravitational acceleration	m/s^2
I	Turbulence intensity	-
k	Proportional constant (S=kR)	Pa/Nm
l	Turbulence length scale	m
m	Wöhler-curve parameter	-
m	Blade-section mass	Kg/m
M_f	Flap-wise bending moment	Nm
M_e	Edge-wise bending moment	Nm
n'	Average RFC cycles per second	Hz
n'_{tip}	n' evaluated at blade tip (r=R)	Hz
N	Cycles (Wöhler-curve)	-
r	Coordinate, radius	m
R	Load-range	Nm
R	Rotor radius	m
S_0	Wöhler-curve parameter	Pa

Prepared using weauth.cls [Version: 2010/06/17 v1.00]

S	Stress-range	Pa
t	Simulaton time	s
T	Component lifetime	s
v	Axial wind speed	m/s
v_a	Axial wind speed in rotorplane	m/s
V_0	Wind speed	m/s
x	Continuous RFC variable	
z_{hub}	Hub height	m
α	Angle of attack	rad.
α	Shear factor	-
Ω	Rotational speed	s^{-1}
ρ	Mass density	kg/m^3
σ_1	Turbulence standard deviation	m/s
RFC	Rainflow-count	
NTM	Normal turbulence-model	
DLC	Design load-case	
HAWT	Horizontal-axis wind turbine	

2. INTRODUCTION

Wind turbine blades are designed for a typical lifetime of 20 years during which they operate in the atmospheric turbulence and under cyclic gravitational loading. This causes the loads on the blade to vary in time which cause fatigue damage. Control strategies and stability issues are also important but will not be studied in detail here. In addition to aerodynamic efficiency and production price, fatigue survivability is a main design driver and it is therefore extremely important to calculate the fatigue damage and component lifetime when designing wind turbine blades.

We have derived an analytical expression which describes the fatigue loads on wind turbine blades. The results are given in terms of equivalent fatigue loads for the edge- and flapwise bending moments. This has the advantage that the fatigue damage, which results from a complicated load history, can be quantified using a minimum of material- and structural data. We calculated equivalent loads numerically and compared them to analytical predictions to validate the theory. The NREL 5 MW fictitious reference turbine [1], which is representative for modern wind turbines in the MW range, was used as a test case. The numerical simulations of the wind turbine were made using HAWC2 [2], which is an aeroelastic code developed at RISØ DTU National Laboratory for Sustainable Energy.

We had two reasons for deducing the analytical expression. 1) It provides a simplified mean for predicting fatigue damage and is useful for initial design purposes. 2) Given the success of the analytical model we have established the important parameters which influence the fatigue damage. This knowledge is important because it clearly shows designers how they can improve the design.

The structural design requirements for blades are described in standards (IEC 61400-x [3]). An appropriate fatigue analysis based on a 10 min aeroelastic time series has to be carried out, using e.g. the Palmgreen-Miner theory for a number of design load cases (DLCs). The DLCs corresponds to typical operating conditions described by wind speed, turbulence intensity, wind shear etc. We used DLC 1.1 in [3] as the numerical reference case, which corresponds to normal operation from cut-in to cut-out wind speed in atmospheric turbulence using the normal turbulence model (NTM).

Previous work has mainly focused on the development of aeroelastic codes and the correct numerical estimation of fatigue damage - i.e. a completely numerical approach which is carried out routinely in the design and certification of wind turbines. Some good examples of the results of this approach can be found in a study by Larsen *et al.* [4]. The results are based on heavy calculations and it is hard to generalize them since wind-turbines differ very much from one manufacturer to the next. In this article we present an analysis which aims at providing this generalization. Fuglsang [5] gives a general introduction to wind turbine design and optimization, but the discussion remains qualitative. In Fuglsang & Madsen [6] the possibility of fast engineering models for estimation of fatigue damage is mentioned and a semi-empirical model is suggested. This model is based on a linear relationship between the variations in blade bending-moments and the turbulence standard deviation, and this is in agreement with the results from our work. Fuglsang approximated the linear-coefficient using empirical data and the wind speed derivative of bending moments in steady state operation. The procedure had to be repeated whenever the overall dynamics or rotational speed changed, which makes it complicated to use in general. Fuglsang [7] also describes how 2D airfoil properties affects the turbine design, and he makes aeroelastic calculations for a slender blade with reduced chord. The results are a reduction in blade fatigue loads and this is in agreement with our conclusions.

Burton *et al.* [8] describes analytical methods for calculation of varying loads on the wind turbine. The analysis takes blade eigenmodes and wind turbulence into account which is more advanced than our method, where the effect of free vibrations are ignored. A major drawback is that the results are expressed as standard deviations of loads. Another drawback is that the mass distribution and modeshapes are used as input. These data are not easily available.

3. METHODS

In the following we describe the important components of the analytical analyses. Variations in wind speed relative to the rotating blade are related to variations in bending moments by taking the blade aerodynamic layout into consideration. We used an analytical expression to describe operation in shear and an engineering model in the case of turbulence. The fatigue damage is expressed using equivalent loads. The variation in bending moment due to gravity is taken as the difference in the static moments in the horizontal blade positions.

3.1. Fatigue Analysis

The fatigue analysis is based on the Palmgreen-Miner theory. A simplified material SN-curve (Wöhler-curve) is defined as

$$\log S_0 - \frac{1}{m}\log N = \log S \quad \Leftrightarrow \quad N = \left(\frac{S_0}{S}\right)^m \tag{1}$$

where S_0 and m are material constants (glassfiber: $m \approx$10, $S_0 \approx 0.062$E , E=Youngs modulus) and N is the number of cycles to failure at stress range S (note that many Wöhler-curves uses the stress amplitude σ_a and this should be multiplied by 2 to obtain the stress range). Using the relationship above, the equivalent fatigue load R_{eq} from a binned rainflow count (RFC) or a distributed RFC is

$$R_{eq}^m = \frac{1}{f_{eq}}\sum n_i' R_i^m \,, \quad R_{eq}^m = \frac{1}{f_{eq}}\int n'(x)R(x)^m \, dx \tag{2}$$

where R is the load ranges and n_i' is the average number of cycles per second. It is assumed that R can be related to S through a linear relationship S=kR. In the distributed form, x is a general variable which is usefull if the load range distribution $R(x)$ depends on a variable. As a special case x=R and the expression is simply the integral form of the binned summation

$$R_{eq}^m = \frac{1}{f_{eq}}\int n'(R)R^m \, dR \tag{3}$$

R_{eq} is the range af a cyclic load with frequency f_{eq} which generates the same fatigue damage as the distributed RFC. The actual fatigue damage in time T is

$$D = f_{eq}T\frac{k^m R_{eq}^m}{S_0^m} \tag{4}$$

where $D >$1 indicates failure. Datapoints in a distributed RFC can be approximated from a numerically determined binned RFC using the formula

$$n'(x_i) = \frac{n_i'}{\Delta x_i} \tag{5}$$

where Δx_i is the bin width of bin i.

3.2. Range of flapwise bending moment

The range-of-change of lift coefficient ΔC_l at radius r is related to the axial velocity range in the rotor plane Δv_a by assuming a linear lift slope ($dC_l/d\alpha$)

$$\Delta C_l = \frac{dC_l}{d\alpha}\Delta\alpha \cong \frac{dC_l}{d\alpha}\frac{\Delta v_a}{v_{rel}} \cong \frac{dC_l}{d\alpha}\frac{\Delta v_a}{\Omega r} \tag{6}$$

where α is the angle of attack, v_{rel} is the inflow velocity relative relative to the blade and Ω is the turbine rotational speed. It is assumed that the important variations in the inflow have a duration which is long enough to reach a quasi-steady state. The range of aerodynamic flapwise bending moment ΔM_f can then be found as

$$\Delta M_f = {}^1\!/_2\rho\Omega \int_r^R \Delta v_a(r'-r)r'\frac{dC_l}{d\alpha}c \, dr' \tag{7}$$

where c is the chord.

3.3. Equivalent flap-wise load due to wind-shear

The case where the wind turbine operates without turbulence in a power law shear is simple because the variations in axial velocities are given analytically as

$$\Delta v_a = (1-a)V_0 \left[\left(1+\frac{r}{z_{hub}}\right)^{\alpha} - \left(1-\frac{r}{z_{hub}}\right)^{\alpha} \right] \tag{8}$$

Note that the axial induction a diminishes Δv_a which is determined as the difference in local windspeed when the blade is pointing up relative to pointing down. The cyclic variations in loads vary with the frequency of rotation so the RFC is binned with 1 bin and the quantities in (2) are

$$n_1' = \frac{\Omega}{2\pi}\,, \quad R_1 = \Delta M_f(\Delta v_a) \tag{9}$$

Fully written out the equivalent load for M_f is

$$R_{eq}(M_f) = \left(\frac{\Omega}{f_{eq}2\pi}\right)^{1/m} \Omega^1\!/_2\rho \int_r^R (1-a)V_0 \left[\left(1+\frac{r}{z_{hub}}\right)^{\alpha} - \left(1-\frac{r}{z_{hub}}\right)^{\alpha} \right] (r'-r)r'\frac{dC_l}{d\alpha}c\,dr' \tag{10}$$

Note that α in the exponent is the shear factor, but in the derivative the angle of attack.

3.4. RFC of axial velocities in a turbulent windfield

The RFC of axial velocities is usually expressed in terms of the power-spectra. Kristensen & Frandsen [9] describes this and compares results with data from the 200 kW Gedser turbine. The theory is advanced so we developed a different and simplified approach. n'_{tip} denotes the distributed RFC of the turbulent, undisturbed wind calculated in the moving frame of reference of the blade tip, with ranges Δv. Other important parameters are the turbulence standard deviation σ_1 at hub height, the rotational speed Ω, rotor radius R, a characteristic turbulence length scale l, the power-law shear factor α and the hub height z_{hub}. A dimensional analysis yields the functional relationship

$$\frac{\sigma_1 n'_{tip}}{\Omega} = f\left(\frac{\Delta v}{\sigma_1}, \frac{\Omega l}{\sigma_1}, \frac{\Omega R}{\sigma_1}, \frac{R}{z_{hub}}, \alpha\right) \tag{11}$$

Figure 1 shows distributed RFCs calculated using HAWC2. The results can be approximated using only the first dimensionless group

$$\frac{\sigma_1 n'_{tip}}{\Omega} = 3.0\exp\left(-\frac{\Delta v}{\sigma_1}\right) = f\left(-\frac{\Delta v}{\sigma_1}\right)\,, \quad \frac{\Delta v}{\sigma_1} \in [0,\ 8.0] \tag{12}$$

Note that this approximation was found for R=63 m, and it may be different for other radii depending on $\Omega R/\sigma_1$. The effect of α is clearly seen in Figure 1. The shear in the atmospheric boundary layer shifts some of the cycles right towards larger Δv.

3.5. Equivalent flapwise load due to turbulence

It is assumed that n'_{tip} is valid on a major part of the blade so that n'=n'_{tip}. Using x=Δv as distribution variable in (2) the other quantities are

$$n'(x) = (1-a)n'_{tip}(x)\,, \quad R(x) = \Delta M_f(x)\,, \quad x = \Delta v = \Delta v_a \tag{13}$$

Note that n' was scaled by the axial induction because this slows the rate of turbulent eddies flowing through the rotor plane. A representative value for a must be used (e.g. a evaluated at 70% radius). The velocity ranges are assumed to be the same in the rotor plane as in the indisturbed windfield. After integration by substitution the equivalent load for M_f was found

$$R_{eq}^m(M_f) = \frac{1}{f_{eq}} 3.0\Omega(1-a) \left(\sigma_1 {}^1\!/_2\rho\Omega \int_r^R (r'-r)r'\frac{dC_l}{d\alpha}c\,dr'\right)^m \int_0^{8.0} y^m e^{-y}\,dy \tag{14}$$

where y=$\Delta v/\sigma_1$ is the substituted integration variable. The two remaining integrals can be solved numerically. The first depends on the aerodynamic properties of the blade and the second on the dimensionless shape of the RFC. The blade properties are therefore completely decoupled from the properties of the atmospheric wind. Note that this equation is valid for R=63 m because it was based on (12).

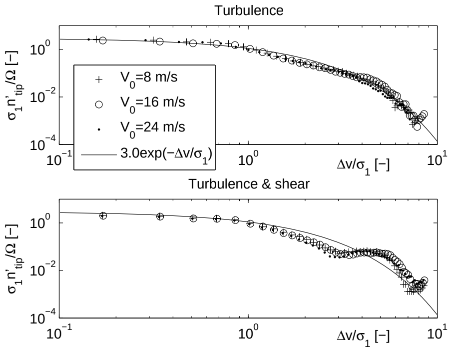

Figure 1. Distributed rainflow count of axial velocities plotted using dimensionless groups

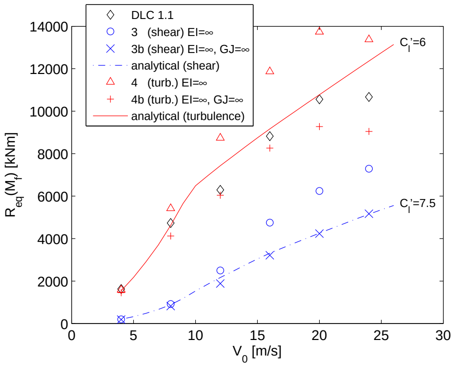

Figure 2. 1 Hz equivalent flapwise root-bending moment. Equations: *Analytical (shear)* (10). *Analytical (turbulence)* (14)

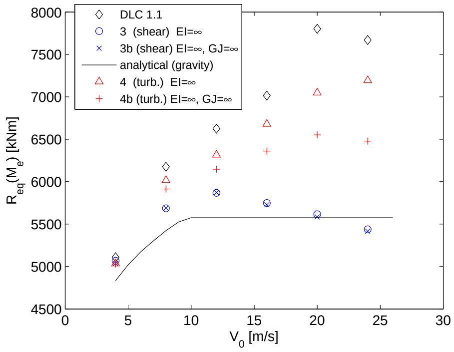

Figure 3. 1 Hz equivalent edgewise root-bending moment. Equation: *analytical (gravity)* (15)

3.6. Equivalent edge-wise load due to gravity

The range of the edgewise bending moment ΔM_e is approximated as the difference in the static moment due to gravity, between the two horizontal blade-positions. Without going into details the equivalent load is

$$R_{eq}^m(M_e) = \frac{\Omega}{2\pi f_{eq}} \left(2g \int_r^R (r' - r) m \, dr' \right)^m \tag{15}$$

where m is the mass density per spanwise length.

4. RESULTS

Table II shows parameters for 5 different cases of numerical simulations. Case 1 is design load case 1.1 (DLC 1.1) in [3], where the normal turbulence model (NTM) is used. The conditions are representative for a turbine under normal operation conditions. Case 3 is without shear and 4 is without turbulence. Except for Case 1, the blade bending stiffness'es are set very high (∞) in order to eliminate effects from bending deformations. The torsion stiffness is either actual values or ∞. The lift-slope $dC_l/d\alpha$ is denoted C_l' figures. The analytical equations are calculated using the static value ($dC_l/d\alpha$=7.5 rad^{-1}) and a reduced value (6.0 rad^{-1}) corresponding to a dynamic lift curve. The static value is set according to the information in the NREL 5 MW documentation [1] and is relatively high when compared to the theoretical value of 2π rad^{-1}.

Figure 2 shows Equations (10) and (14) against numerical results calculated using HAWC2. The loads refer to bending moments evaluated in the blade roots (r=0 m). Figure 3 shows Equation (15) compared to numerical results.

5. DISCUSSION

5.1. Flapwise fatigue loads

If there is no turbulence and only shear, the numerical and analytical results agree well. This was expected because the analytical equations were based on very few assumptions: Mainly that Equation (6) is valid and that the loads change slowly enough to be considered quasi-static so (7) is also valid. I.e. a change in axial velocity causes a quasi-steady deflection of the blade. When turbulence is included, it was expected that changes would happen so fast that the quasi-steady assumption would no longer be valid. However, all results indicate that only large-scale changes in the axial velocity are important for the root-bending moment, and these are varying so slowly that a quasi-steady deflection of the blade is reached.

The dynamic lift slope was expected to be diminished and this can be described using the concept of the reduced frequency. It can be seen that Equation (14) agrees fairly well with DLC 1.1 for dC_l/d_α=6.0 rad^{-1}. At very high wind speeds HAWTs are often stalled on large parts of the blades. In this case, (6) is no longer valid and there is no simple link between a change in axial velocity and a change in lift. The effect of this may be seen in Figure 2 where the analytical equations predict increasing fatigue loads with wind speed but the numerical simulations indicate a maximum around 20 m/s. In general, it is therefore important to be critical when selecting the lift curve slope. Apart from the issues mentioned (stall, reduced frequency) the introduction of trailing edge flaps can be modeled as a reduction of dC_l/d_α.

Based on the relatively good results obtained it can be concluded that Equation (12) can be used as an engineering tool for predicting the RFC of axial velocities. However, it is important to remember that it described the RFC at the blade tip, but was used along the whole blade. Depending on the usage, it may have to be re-evaluated based on numerical simulations or experiments. This is also the case if shear is more dominant. Note that the analysis was based on numerical calculations using the Mann turbulence model and therefore represents an accepted approximation to real turbulence.

Torsion stiffness is important, and R_{eq} is in general higher when the blade is soft in torsion. An explanation for this is the change in the angle of attack introduced when the blades twist, but the actual behaviour may depend heavily on the specific design (sweep etc.). When the blade bending-stiffness is soft, then R_{eq} is somewhat reduced because the time delay caused by the bending acts as a low pass filter removing the effects of fast changes. However, these mechanisms are very complicated and it is not possible to draw any general conclusion. We note that, in many cases, the fatigue loading will also depend on stability issues and the turbine control algorithm.

5.2. Design guidelines - flapwise fatigue loads

Equation (14) shows the following relationship to the flapwise fatigue damage

$$D \propto k^m R_{eq}^m \,, \quad R_{eq}^m \propto \Omega^{m+1} \,, \quad R_{eq}^m \propto \sigma_1^m = I^m V_0^m \,, \quad R_{eq}^m \propto \left(\int_r^R (r' - r) r' \frac{dC_l}{d\alpha} c \, dr' \right)^m \tag{16}$$

DOI: 10.1002/we
Prepared using weauth.cls

Table II. Key parameters and simulation cases

Case	α (shear)	Turbulence	EI (Bending stiffness)	GJ Torsion stiffness
DLC 1.1	0.2	NTM	Soft	Soft
3	0.2	0	∞	Soft
3b	0.2	0	∞	∞
4	0.0	NTM	∞	Soft
4b	0.0	NTM	∞	∞

where I is the turbulence intensity. Thus, increasing I and Ω increases the fatigue damage dramatically. It can also be seen that the chord distribution is very important, especially on outer parts of the blade where a shorter chord will reduce the fatigue damage. Finally, the effect of the unsteady 2D aerodynamics is included through $dC_l/d\alpha$. Note that these formulas can be used for optimization by minimizing the shown quantities.

5.3. Edgewise fatigue loads

In the special case of no turbulence the edgewise fatigue loads are predicted with good accuracy using (15), which is based on quasi-steady gravity loads. When turbulence is included, the equivalent fatigue load is increased by approximately 50%. This shows the important effects of turbulence on edgewise fatigue loads. The aerodynamic influence on edgewise fatigue loads has not been described analytically in this work.

5.4. General notes

The equivalent loads were all evaluated in the blade root (r=0 m). For $r > 0$ we expect the validity of the analytical analysis to be better because it is a better assumption that $n'=n'_{tip}$ and because there is less filtering of the fast structural dynamics.

The dimensionless RFC can be expected to vary with rotor radius, so the results presented cannot be scaled directly to turbines which are very different in size. In that case, the dimensionless functional relationship must be determined again if an absolute value for the fatigue load is needed. It is not necessary to reevaluate if a relative design study is carried out, because the atmospheric properties are decoupled from the turbine design properties.

6. CONCLUSION

The fatigue caused by the flapwise bending moment can be predicted by the theory presented. The accuracy is best in the case of rotation in shear, which shows that the assumptions used in the analytical approach are valid and that the important fatigue generating effects have been identified. However, the fatigue damage is much higher when turbulence is present and the fatigue loads are described by Equation (14). Important parameters include the dynamic lift-curve slope, the turbulence standard deviation, the chord distribution, and the rotational speed (the latter increases both cycles and load).

The edgewise fatigue loads have been threated analytically based on the assumption that gravity loads are predominant. The results are in good agreement with numerical calculations when shear and turbulence are excluded. When included, the results deviate substantially and the actual loads are up to 50% greater. The aerodynamic forces are therefore important for the edgewise fatigue loads.

We have presented a methodology for optimization of wind turbine blades for low flapwise fatigue loads. The method is fast because it is based on integral quantities, making it possible to omit aeroelastic time simulations in the initial design process.

REFERENCES

1. Jonkman J, Butterfield S, Musial W, Scott G. Definition of a 5-MW Reference Wind Turbine for Offshore System Development. *Technical Report NREL/TP-500-38060*, NREL National Renewable Energy Laboratory 2009.
2. Larsen TJ. How to HAWC2, the user's manual. *Risø-R-1597(ver. 3-9)(en)*, Risø DTU, Technical University of Denmark 2009.
3. IEC 61400-1. International Standard, Wind Turbines - Part 1: Design requirements (Third edition). *IEC 61400-1:2005(E)* 2005.
4. Larsen TJ, Madsen HA, Larsen GC. Comparison of Design Methods for Turbines in Wake. *Research in Aeroelasticity EFP-2007* 2008; .

5. Fuglsang P. Aerodynamic Design Guidelines for Wind Turbine Rotors. *A Collection of the 1998 ASME Wind Energy Symposium Technical Papers at the 36th AIAA Aerospace Sciences Meeting and Exhibit* 2002; .
6. Fuglsang P, Madsen HA. Optimization method for wind turbine rotors. *J. Wind Engineering and Industrial Aerodynamics. Vol 80.* 1999; .
7. Fuglsang P. Vingedesign. *Forskning i Aeroelasticitet EFP-2002. Bak C. (ed)* 2002; :49–64.
8. Burton T, Sharpe D, Jenkins N, Bossanyi E. *Wind Energy Handbook*. John Wiley & Sons, 2001.
9. Kristensen L, Fransen ST. Model for power spectra of the blade of a wind turbine measured from the moving frame of reference 1982; .
10. Connel JR. Turbulence spectrum observed by a fast rotating wind turbine blade, Rep. PNL-3426, Battelle Pacific Northwest Laboratory, Richland, WA 99352 1980; .

Risø DTU is the National Laboratory for Sustainable Energy. Our research focuses on development of energy technologies and systems with minimal effect on climate, and contributes to innovation, education and policy. Risø DTU has large experimental facilities and interdisciplinary research environments, and includes the national centre for nuclear technologies.

Risø DTU
National Laboratory for Sustainable Energy
Technical University of Denmark

Frederiksborgvej 399
PO Box 49
DK-4000 Roskilde
Denmark
Phone +45 4677 4677
Fax +45 4677 5688

www.risoe.dtu.dk